Optical and electrophysiological technologies for monitoring cortex-wide brain activity

A DISSERTATION

SUBMITTED TO THE FACULTY OF

THE UNIVERSITY OF MINNESOTA

BY

Jia Hu

Department of Mechanical Engineering

University of Minnesota, Twin Cities

Advisor:

Prof. Suhasa Kodandaramaiah, Department of Mechanical Engineering

Submission Date:

June, 2023

Copyright Page

Acknowledgments

First, I would like to express my sincere gratitude to my advisor, Dr. Suhasa Kodandaramaiah, founder of the Biosensing and Biorobotics Laboratory (BSBRL) at the University of Minnesota, Twin Cities (UMN). Dr. Kodandaramaiah recruited me as an undergraduate researcher during my junior year of college study in biomedical engineering and has been my advisor throughout my bachelor's, master's, and Ph.D. studies in BSBRL. As the second student to join the lab, I was lucky to receive hands-on training from Dr. Kodandaramaiah in essential engineering and research skills such as programming, device prototyping, craniotomy, and experiment design. I appreciate his patience and kindness in guiding me as I started as a fresh kid in the research. I will never forget Dr. Kodandaramaiah has always encouraged me to make independent decisions in my research while providing valuable advice.

I especially thank my colleague, Dr. Leila Ghanbari, the first Ph.D. student who graduated from BSBRL with marvelous achievements, my dear friend and student mentor tutoring me in her projects: See-Shell and Craniobot, for preparing me for my research. I sincerely appreciate that, during my Ph.D. study, Leila and her husband treated me like a younger baby brother.

I want to thank Dr. Julianna Abel and her student Mr. Henry Koon, who collaborated to create a woven tetrode neural activity sensing technology in my master’s study, my first leading research project, where I worked closely with my colleague, Miss Gabrielle Shull (Gaby). This project was published, presented, and earned the student competition finalist award at the American Society of Mechanical Engineering’s premier conference on smart materials, adaptive structures, and intelligent systems. I will never forget Gaby as a brilliant and ambitious warrior with a soft and kind heart caring for the need and the weak.

I want to thank our collaborators Dr. Michael McAlpine and his labmates, Dr. Zhijie Zhu, Mr. Vincent Belsito, and Dr. Jiyong Lee. We worked closely to create a 3D-printed transparent electrocorticography (ECoG) electrode brain sensor making a significant Chapter of this thesis. In Dr. McAlpine's lab, Dr. Ruitao Su, Dr. Xia Ouyang, and Mr. Danial Ng are all my friends, and we have many fun times together. Ruitao and Ouyang are kind, soft-hearted, competitive scientists who taught me many helpful research skills. Daniel, as a Malaysia Chinese, presents the most traditional hospitality and humbleness of Chinese that always drives me to be a better me.

I would like to thank Dr. Preston Donaldson and his Advisor, Dr. Sarah Swisher providing valuable support for my research from their expertise in electrical engineering. We attended the 2022 MRS conference in Hawaii and presented our research work there. During the conference, I appreciated Preston and his parents caring for me when I was sick on the trip.

All my colleagues in BSBRL are my friends and trustable comrades in research. The credit has to be first given to Dr. Kodandaramaiah, who makes our lab environment and culture, in my opinion, one of the most comfortable, diverse, productive, and resourceful teams in UMN:

Miss. Alana Tillery, a hardworking and talented researcher, conceptualized an idea of a fully-desktop fabricated brain sensor with Dr. Kodandaramaiah and me. This sensor became a significant part of this thesis. Alana is also my dear nerd comrade sharing the same tastes in anime, music, and Japanese jokes. Mr. Yash Mangalick, a brilliant high-school young gentleman, now a Columbia University undergraduate, also assisted me in my research. Yash is one of the few jünger using his desire and passion for research to drive me to accelerate work progress when I was his Ph.D. student mentor.

Mr. Mathew Rynes, who also joined BSBRL in the first year, worked closely with Leila and me on an automatic surgical robot project. As a hardcore socialist, Matt values his social responsibility to the US and all humankind to correct the systematic error in our society and pursue a brighter future for our civilization. I will never forget, on a freezing 0°F night, Matt stapling posters around campus for the gathering of supporting the working class.

Dr. Ridwan Hossain used his critical engineering expertise to solve numerous complex problems in our research, drawing on his deep knowledge of material science. Ridwan's unwavering confidence and optimistic encouragement motivated me, and he played an instrumental role in refining our experiments and design, laying a solid foundation for our research.

In the microcamera array project, Mr. Skylar Fausner, Mr. Vijay Rajendran, and Ridwan contributed to tackling challenging biological and engineering obstacles in the early stage. Skylar, in particular, demonstrated exceptional lab management skills, overseeing the care of all animals in my studies and providing me with valuable insights into efficient and effective work procedures. Despite frequent design modifications, Vijay delivered his work on time and to a high standard. I would like to thank my former lab managers, Miss. Samantha Linn, a talented, friendly, and progressive friend, and Mr. Orestes Hadjistamoulou, the fastest mouse brain surgeon I have even met.

Mr. Arun Cherkkil, Mr. Ibrahim Oladepo and Miss. Zoey Viavattine are in charge of further developing the micro-camera array project. We have helped each other, made rapid work progress, and given an impressive presentation at the 2023 Society for Neuroscience conference. Arun has impressive productivity and fast learning ability. Besides research, Zoey and I have many exciting conversations regarding meditation and health, making my research life more colorful.

Miss Zahra Navabi helped me in nearly all my Ph.D. research projects. Zahra and I have had countless meaningful conversations regarding the world, religions, video games, and neuroscience, making her a very interesting and valuable comrade in the lab.

Mr. Pinhao Chan is a kind and warm-hearted young man who always worries about my career development and tries to bring me more connections and resources even on our road trip driving Highway No.1 from the SfN conference in San Diego to San Diego Fransico.

Mr. Daniel Surinach often willingly provides me with new components, tools, and invitations to his house's drinking parties. Before Pinhao joined the lab, Daniel, as a Native American, was surprisingly the only lab member who could speak Chinese with me. Mr. Andrew Alegria and Dr. Amey Joshi are two very interested and fun researchers and drinking fellows that have always brought countless joy to my Ph.D. study. Mr. Jacob O'Brien is a hard-working researcher who achieved his master's degree with a Ph.D. level quality of work. Together with Andrew, Amey, Zahra, and Jacob, we developed a COVID-19 responding device and published a conference proceeding at the ASME 2021 Medical Device Conference.

Dr. James Hopes, a talented and hardworking leading scientist, and engineer in our lab, gave me valuable guidance on research and writing. He helped review this thesis and gave me writing lectures on presenting research work and ideas better. As an experienced neuroscientist, Dr. Kapil Saxena taught me many vital pieces of knowledge related to my research. He gave me many Indian culture, music, and food appreciation opportunities that I have greatly enjoyed.

I also need to thank my dear friends Louis Ting and Kevin Justinus Hartoyo since we met in the first year of our biomedical engineering undergraduate program at UMN. Louis and I have worked on many medical device development projects, and Louis’s engineering and

management skills have profoundly shaped my working procedures for solving engineering/research problems. Most importantly, as a Malaysia Chinese and my Christian brother, Louis always guides and encourages me to live with a traditionally noble goal of using our engineering skills to serve humankind rather than self-interest. Besides school study, Kevin, Louis, and I worked together and won an award from Minnovation Medical Device Competition. Kevin's teaching in our study hour before final exams significantly helped me to pass challenging classes with high grades, and he loves to invite us to his place and prepare excellent meals for us.

As for my family, they are the most important support of my Ph.D. study. As the little emperor, the only child, in a mainlander Chinese family, I genuinely believe that I am privileged that my mother, a mechanical engineer, and my father, a civil engineer, have trained me with strict disciplines but at the same time with countless and selfless love, understanding, and sufficient economic supports. I still remember when I was two years old, my mother started reading world and China history to me, from which she tried to let me understand the importance of learning the mistakes from our past and making our world a better place through continuous improvements of our civilization. I always feel grateful to the Almighty for letting me be born and grow up in this big and loving family, all my grandparents, uncles, aunties, and cousins, from both sides, rich and poor, educated or not, with various religious backgrounds and political perspectives allows me to see the world in a very colorful form.

I also have to thank many people like Church brothers and sisters, friends, and classmates who, directly and indirectly, helped me with my Ph.D. study and life. I feel sorry I cannot put all of them in this thesis acknowledgment or need another hundred pages. I sincerely appreciate their

kindness and will always appreciate being served and learning how to better serve others with kindness and generosity rooted in our conscience gifted by the LORD.

ABSTRACT

Recording cortex-wide brain activity and decoding the brain's neural computations are required to mediate behaviors. Such an understanding will help formulate better treatments for neurological disorders and improve the quality of life. Technologies for sensing neural activities have been continuously developed over the past century. These technologies have gradually improved to recording from larger brain regions at high temporal and spatial resolution. Miniaturized devices have been developed for performing such imaging in freely-behaving animals. Along these lines, this thesis first aimed to develop a high-accessibility neural activity sensing technology and developed a fully desktop-fabricated flexible Graphene electrocorticography (ECoG) arrays that can be completely built using commonly used laboratory tools without the need for specialized cleanroom facilities. The ECoG arrays could be implanted chronically for up to 180 days allowing high-quality measurement surface field potentials. Building on this work, I developed a 3D-printed transparent ECoG array that simultaneously performs ECoG recordings and mesoscale Calcium (Ca^{2+}) imaging from multiple sites. This device allowed the combination of high temporal resolution electrophysiological measurements with high spatial resolution optical readout of neural activities. In in vivo recording, the 3D-printed ECoG recorded stimuli-evoked and anesthesia drug-induced brain activity in mice and showed strong correlations between the optical and electrical signals with a cross-correlation factor > 75%. In the third aim, I developed a miniaturized micro-camera array microscope (mini-MCAM) for cortex-wide Calcium imaging at single-cell resolution in head-fixed or freely behaving mice. Mini-MCAM is an array of 4 microcameras generating a large computationally stitched FOV of 30-40 mm2 with a central resolution of 9.9 μm. The mini-MCAM recorded spontaneous brain activities at head-fixed and freely behaving states where

distinctive neurons' activities were recorded and identified. In this thesis, all three neural activity sensing technologies share a common goal to improve the existing neural activity sensing technologies and accelerate fundamental neuroscience research, which will bring new insights into the brain.

Table of Contents

Acknowledgments……i

Abstract……..……...……vii

List of Figures……xi

Project summary

Chapter 1: Introduction: background and motivation

1.1 Importance of studying the brain……...….1

1.2 Existing neural activity sensing technologies……..……...3

1.3 Accessibility of ECoG electrode arrays decided by fabrication procedures……5

1.4 Combining ECoG recording with Calcium imaging……..…....6

1.5 Approach for ideal neural activity sensing technology……...8

1.6 Thesis Outline…….....9

Chapter 2: Fully desktop-fabricated flexible graphene electrocorticography (ECoG) arrays

2.1 Introduction……..13

2.2 Approach……..15

2.3 Results……..20

2.4 Discussion……30

2.5 Methods……33

2.6 Summary……..43

Chapter 3: 3D printed flexible transparent PEDOT:PSS ECoG array

3.1 Introduction……...……...45

3.2 Approach……..46

3.3 Results……..47

3.4 Methods……....57

3.5 Summary……..58

Chapter 4: Micro-camera array for monitoring cortex-wide brain activity at cellular resolution

4.1. Introduction……61

4.2 Approach……..65

4.3. Results……69

4.4 Methods……76

4.5 Summary……..79

Chapter 5: Conclusion and future perspective……....80

References……..……86

List of Figures

Figure 1.1.1 | Brain's neural network and its functional regions……..…..…2

Figure 1.2.1 | Neural activity sensing technologies……..….3

Figure 1.3.1 | Fabrications of existing ECoG devices……..….5

Figure 1.4.1 | Non-transparent ECoG electrode array vs. transparent ECoG electrode array…..…..6

Figure 1.5.1 | Ideal neural activity sensing technology……..…..…..8

Figure 2.2.1 | Stencil-printed flexible graphene ECoG array……..15

Figure 2.2.2 | Laser-cut stencil characterization…….16

Figure 2.2.3 | bonding between PCB and ECoG electrode array…….17

Figure 2.2.4 | whole ECoG device assembly……...18

Figure 2.3.1 | Material characterization of graphene films using three graphene inks…….20

Figure 2.3.2 | Electrochemical characterization of the ECoG electrode……..22

Figure 2.3.3 | *In vivo* performance of the graphene ECoG devices……..25

Figure 2.3.4 | Ketamine induced brain response……27

Figure 2.3.5 | Sensory stimulus-evoked responses recorded by the graphene ECoG devices……..28

Figure 2.5.1 | Sample preparation for electrical characterization……34

Figure 2.5.2 | Custom-built spin coater……...36

Figure 2.5.3 | Bending test……..39

Figure 3.2.1 | 3D-printed transparent PEDOT:PSS/SU-8 ECoG array and implant device…….46

Figure 3.3.1 | Thin-film optical transmission……..48

Figure 3.3.2 | Chronic implantation of 3D printed devices……..50

Figure 3.3.3 | Functional use of ECoG arrays to measure stimulus-evoked responses……52

Figure 3.3.4 | Correlations between ECoG and Calcium Signals……53

Figure 3.3.5 | Simultaneous electrophysiology and Ca^{2+} imagined in Thy1-GCaMP6f mice…….55

Figure 4.1.1 | Existing Calcium imaging device of cellular or near-cell resolutions……...62

Figure 4.2.1 | Two approaches to increase FOV…….65

Figure 4.2.2 | See-Shell vs. 4-plane transparent skull implant…….66

Figure 4.2.3 | Assembly and photos of mini-MCAM……..67

Figure 4.3.1 | Benchtop testing……...69

Figure 4.3.2 | Head-fixed recording of spontaneous brain activity……..72

Figure 4.3.3 | Calcium imaging of spontaneous brain activity in freely behaving mouse……75

Chapter 1:
Introduction: background and motivation

1.1 Importance of studying the brain

The human brain contains approximately 86 billion neurons and is considered the most complex organ in the human body [1]. Each neuron may have thousands of connections to other neurons, creating trillions of interconnections across the brain and forming a computational network to process sensory information and mediate sensory-motor behaviors [2], [3] (**Fig 1.1.1a**). At the micro-scale, neuron-neuron interconnections result in stereotyped neuronal circuits [4]. At the macro-scale, these neural circuits are located in distinct functional regions, including the motor cortex, which is responsible for voluntary movements [5], [6]; the somatosensory cortex, which processes input information like touch, temperature, and pain from various skin sensors [7]; and, the visual cortex which processes visual information collected by the retinas [8] (**Fig 1.1.1b**). These functional regions also interact with each other to perform complex brain-wide computations that mediate behaviors such as movement control [9], emotion regulation, and memory formation [10] through their functional connectivity [11], [12]. Any disruption or malfunction occurring in these interactions can result in disorders such as Alzheimer's disease, schizophrenia, and depression [13], [14]. Understanding the brain by mapping the interactions between regions can provide insights into these disorders and potential treatments.

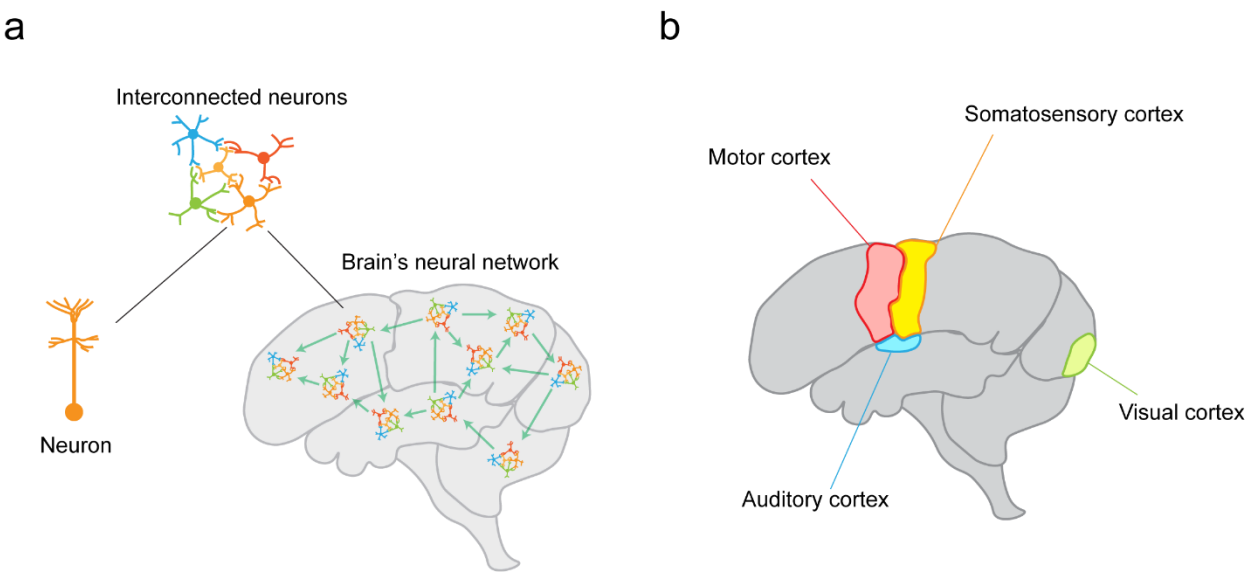

Figure 1.1.1 | Brain's neural network and its functional regions: (a) Brain's neural network contains approximately 86 billion neurons. These neurons communicate through their electrochemical signals. **(b)** The brain has many distinct function regions like the motor cortex for motion control, the somatosensory cortex for input signals like touch and pressure from skill sensors, the auditory cortex for sound, and the visual cortex for vision.

Aside from neurological disease studies, mapping the neural activity during neuromodulation provides an opportunity to understand the direct stimulation applied to the brain influences behaviors [15]. For example, transcranial direct current stimulation has been shown to enhance the individual's performance in discovery-learning visual search tasks by improving attention [16], learning [17], and memory capability [18], while a second neuromodulation technology, transcranial direct current stimulation, has been shown to improve perceptual discrimination, motor learning speed, and visual searching ability [19]. To understand the neural bases of these changes in behaviors and to improve the effectiveness and efficiency of these neuromodulation technologies, neural activity sensing techniques such as functional magnetic resonance imaging

(fMRI) [15] and electroencephalogram (EEG) [20] have been used to record the simultaneous brain activity under these types of transcranial stimulations.

1.2 Existing neural activity sensing technologies

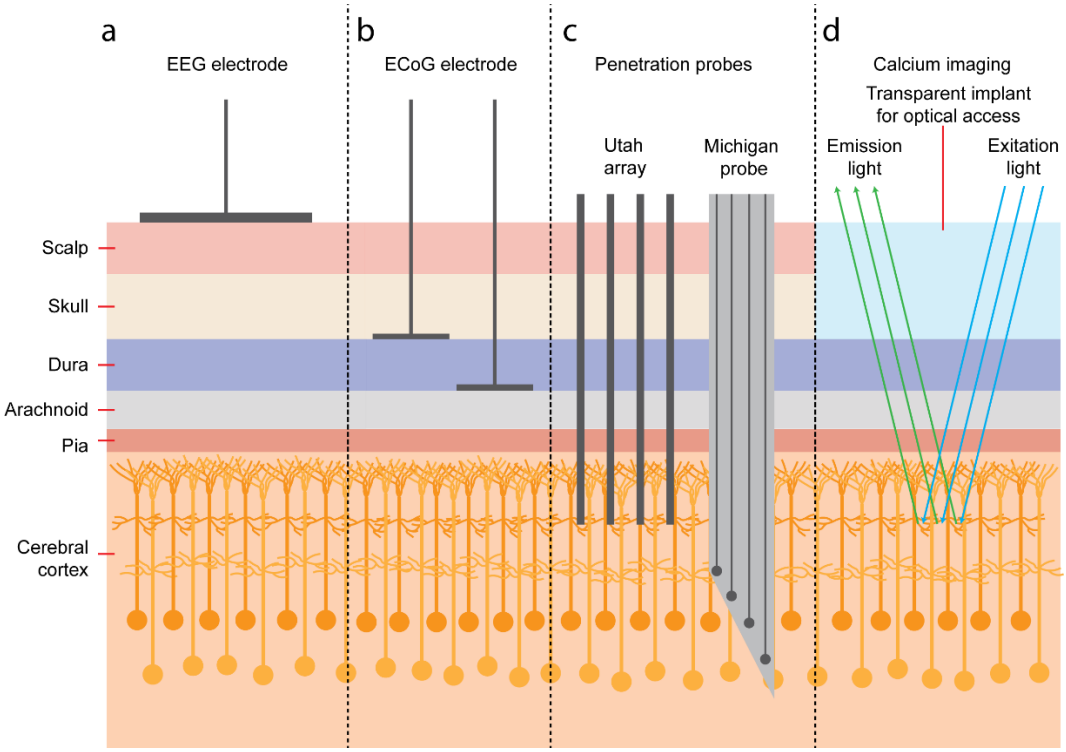

Figure 1.2.1 | Neural activity sensing technologies: (a) Electroencephalography (EEG) electrodes are placed on the scalp to measure the brain's electrical activity. **(b)** Electrocorticography (ECoG) electrodes are placed on the brain surface without penetrating the brain tissue. **(c)** Penetrating probes such as Utah array, a needle probe array, and the Michigan probe, a multi-electrode shank, penetrate the brain tissue to record the neural activity. **(d)** Calcium imaging measures the brain's Calcium activity under a transparent skull implant using optical microscopy.

To get new insights into the brain, neural activity sensing technologies have been continuously developed and improved. Mainly, these sensing technologies measure brain activity directly through its electrical signals [21] or indirectly through optical signals from indicators [22]. For

collecting electrical signals, electroencephalography (EEG) has been used to measure the brain's electrical activity by placing sub-centimeter size electrodes on the scalp [23]. Because EEG does not require surgical implantation, it has become one of the most user-friendly technologies for research and clinical applications like epilepsy diagnosis [24]. However, as shown in **Figure 1.2.1a**, the presence of scalp, skull, dura, arachnoid, and pia between the EEG electrodes and the neurons results in a coarse spatial resolution of several centimeters. This resolution makes it possible to map large-scale interactions between the brain's functional regions but impossible to map the interactions within small groups of neurons among these regions. To observe the neural activity of this small group of neurons, the spatial resolution of the neural activity sensing tools can be improved by using smaller electrode size, increasing the electrode density, and shortening the distance between the electrodes and the neurons [25] (**Fig. 1.2.1 c**), Michigan probes [26] (**Fig. 1.2.1 c**), and tetrodes [27] have been developed. However, all of these devices penetrate the brain tissue, causing tissue damage that can trigger an immune response leading to tissue encapsulation around the neural probes and degradation of signal quality in the long-term [28]. Intracortical EEG, also known as electrocorticography (ECoG), has been developed to reduce the problems associated with penetrating probes while still providing relatively high spatial resolutions in the micrometer scale [29]–[39]. ECoG achieves this balance by measuring the brain's surface field potential through a grid array of small electrodes placed on the brain's surface [40].

1.3 Accessibility of ECoG electrode arrays decided by fabrication procedures

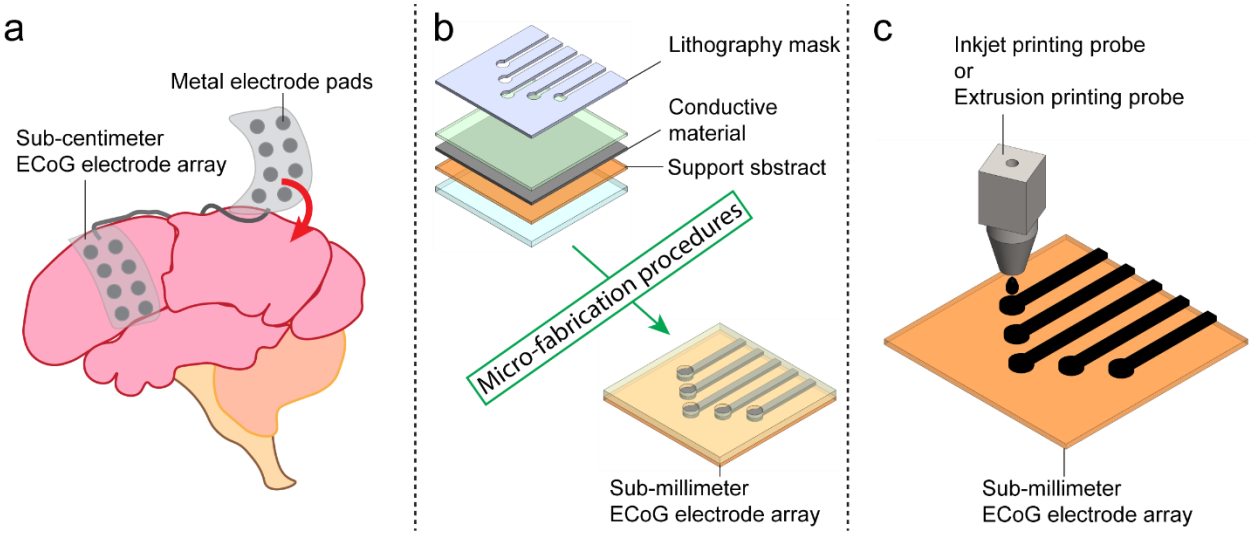

Figure 1.3.1 | Fabrications of existing ECoG devices: (a) ECoG electrode arrays of sub-centimeter resolution used in medical applications are made from biocompatible metals such as gold and titanium alloy. **(b)** Sub-millimeter ECoG electrode arrays are commonly built using microfabrication techniques such as lithography, physical vapor deposition, and chemical etching. **(c)** Inkjet-printing or extrusion-printing simplifies the fabrication procedures of sub-millimeter ECoG electrodes by direct electrode patterning, which still cannot completely evade microfabrication or specialized fabrication techniques like lithography and etching for patterning insulation materials on the electrodes.

For the human brain, with a size of tens of centimeters, a high-density ECoG electrode array with subcentimeter-sized electrodes is sufficient for mapping brain activity in subcentimeter resolution [41] (**Fig 1.3.1a**). In rodent brains, however, with a size of several millimeters, submillimeter ECoG arrays are required to resolve the brain in meaningful detail. Submillimeter ECoG arrays are generally fabricated using specialized techniques such as lithography [42], vapor chemical deposition [35], and plasma etching [33] to pattern conductive materials into electrode arrays (**Fig 1.3.1b**). These techniques require expensive equipment, professional skills,

and highly specialized training, which limits the adoption of sub-millimeter ECoG arrays by neuroscientists in their research. In recent years, improvements in the precision of printing techniques have made it possible for them to fabricate submillimeter ECoG arrays (**Fig 1.3.1c**) with higher fabrication efficiency thanks to the printing's additive manufacturing processes [29], [43]. However, printing techniques often require expensive specialized printers and professional skills to maintain and operate [43]–[45], so simpler fabrication of sub-millimeter ECoG arrays is still needed.

Chapter 2 of this thesis presents a fully desktop-fabricated ECoG electrode array that can be easily reconfigured and built using common bio-laboratory tools with minimal training.

1.4 Combining ECoG recording with Calcium imaging

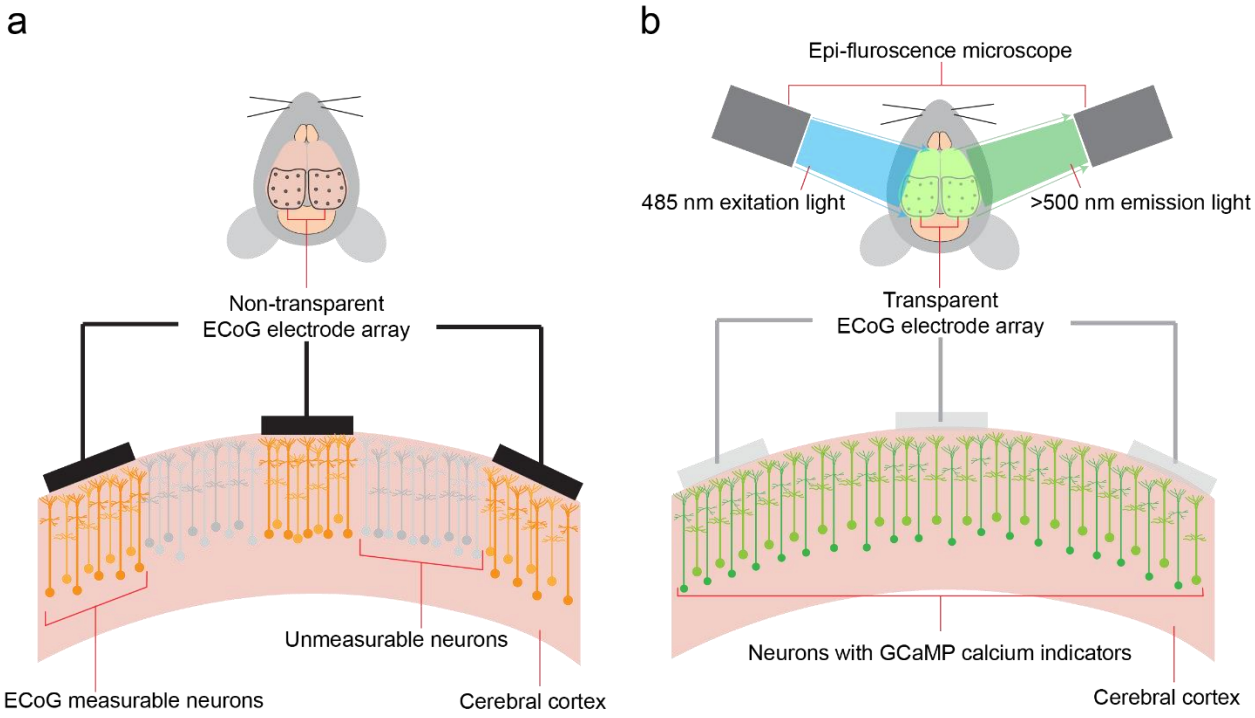

Figure 1.4.1 | Non-transparent ECoG electrode array vs. transparent ECoG electrode array: (a) non-transparent ECoG electrode array can only measure the local field potential from the brain regions under the electrode, where the spatial resolution depends on the size of and distance between neighboring electrodes. Meanwhile, the ECoG array cannot directly record the neural activity of the regions without an electrode above. **(b)** Transparent ECoG electrode array creates optical access to the brain allowing simultaneous Calcium imaging and ECoG recording. Calcium imaging can record the neuronal activity from any brain region with or without an electrode leading to much finer spatial resolution.

Calcium imaging uses optical microscopy to measure neural activity through fluorescence of Calcium-sensitive proteins (**Fig 1.2.1 d**) [43]–[45]. The main advantage of this technique is its ability to record neural activity across large areas of tissue at high spatial resolution, whereas its main disadvantage is poor temporal resolution compared to electrophysiology techniques such as ECoG and EEG. Combining ECoG and Calcium imaging techniques would leverage the high spatial resolution of Calcium imaging with the high temporal resolution of ECoG to produce high temporospatial recordings of neural activity. This combined technique requires transparent ECoG electrode arrays to provide optical access to the brain. Some existing transparent electrode array devices have been built by patterning transparent conductive materials such as Graphene [30], [31], [46] and PEDOT:PSS [39], [43], [47], which all require specialized fabrication techniques.

Chapter 3 of this thesis presents a transparent PEDOT:PSS ECoG electrode array fabricated by patterning conductive materials and insulating materials using a 3D-printer.

1.5 Approach for ideal neural activity sensing technology

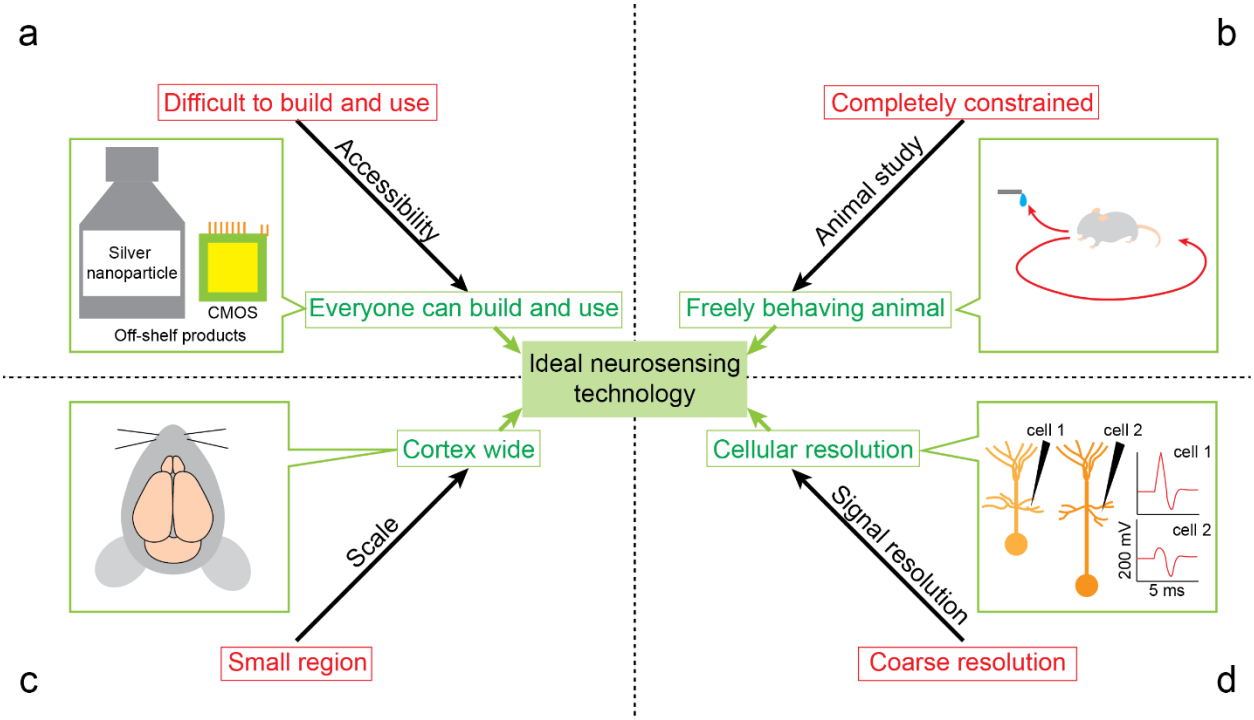

Figure 1.5.1 | Ideal neural activity sensing technology: The ideal neural activity sensing device can record cortex-wide brain activity at single-cell resolution in a freely behaving animal and be technologically accessible to researchers. **(a)** Accessibility is a measure of how easy to use and cost-effective to build the device is. The ideal device will use low-cost, off-the-shelf materials and be assembled by persons with minimal training and non-engineering background. **(b)** Animal subjects should be freely behaving and capable of performing various tasks such as reward study, social interaction, and space exploration. **(c)** The device should be capable of recording cortex-wide brain activity. **(d)** Recordings should have a high spatiotemporal resolution.

The ideal neural activity sensing device should allow neuroscientists to map cortex-wide recording in freely behaving mice at single-cell resolution [48]. To maximize adoption of the device by other labs, it should also be easy to use and cost-effective to build. (**Fig. 1.5.1a**). Mice, the most common animal model used in neuroscience studies [49], are often headfixed in

experiments to allow for high-performance neural recording hardware. However, headfixation severely impedes the behaviors that neuroscientists can study. Freely behaving mice, on the other hand, exhibit an array of complex behaviors, including social interaction [50], reward training [51], and space exploration [51] (**Fig. 1.5.1b**). To study these complex behaviors in mice, the neural activity sensing device must be miniaturized so that mice can display their natural behaviors with minimal restriction [45], [52], [53]. Achieving neural sensing of cortex-wide brain activity in freely behaving mice would allow neuroscientists to decode the neural substrates of natural behaviors such as sensorimotor processing, learning, and memory [54]. Decoding neural substrates at the neuron level is important because the neuron is the fundamental functional unit of the brain. Therefore, the ideal neural activity sensing technology should resolve neural activity at the single neuron level across large areas of the cortex. Two existing technologies come close to achieving these specifications. The first technology, the Miniscope, can achieve single-cell resolution but has a limited FOV that cannot reach a cortex-wide level [50], [55]–[57]. The second technology, the Mesoscope [50], can achieve cortex-wide brain imaging [53] but has a limited spatial resolution that cannot resolve single-cell activity.

Chapter 4 of this thesis presents an integrated miniaturized microcamera array that is both highly accessible and can perform cortex-wide brain imaging in freely behaving mice at single-cell resolution.

1.6 Thesis Outline

This thesis introduces three different neural activity sensing devices developed to improve performance and accessibility over existing devices.

Chapter 2 presents a fully-desktop fabricated Graphene ECoG electrode array that improves the accessibility over existing sub-millimeter ECoG arrays. To do so, a new Graphene ink was synthesized that allowed for patterning the ECoG electrodes using a stencil. The ink was tested to be stable, bio-safe, and highly conductive in benchtop characterization tests. Next, a desktop fabrication process was developed with care taken to ensure that users with a non-engineering background could design and build their own submillimeter ECoG array by following a set of instructions for this process. The ECoG device was also chronically tested in mice to establish biocompatibility and stability of the signal quality across several months.

Chapter 3 presents a 3D-printed transparent ECoG electrode array for performing simultaneous ECoG and Calcium imaging across most of the mouse dorsal cortex. To do so, a 3D-printing fabrication procedure was established to pattern transparent PEDOT:PSS electrodes and transparent SU-8 insulation layers to form a transparent 8-channel ECoG array. In benchtop tests, the transparent ECoG electrode array was shown to have high light transmission across the blue and green wavelengths necessary for Calcium imaging. Testing of the transparent ECoG array demonstrated successful simultaneous ECoG recording and Calcium imaging 15 days after implantation.

Chapter 4 presents a miniaturized microcamera array (mini-MCAM) for cortex-wide Calcium imaging at single-cell resolution. To achieve this, a 4-plane transparent polymer skull implant was developed that can conform the curved surface of the dorsal cortex into four individual flat surfaces, which matches the brain surface to the focal planes of the microcamera array. Testing of the Mini-MCAM demonstrated a spatial resolution of 11 um and cellular-resolution Calcium imaging of cortex-wide brain activity in mice.

Chapter 5 discusses the limitations, device improvements, and future applications of these all three neural activity sensing technologies.

Chapter 2:

Fully Desktop Fabricated Flexible Graphene Electrocorticography (ECoG) Arrays[1]

[1] The work reported in this chapter is based on the following original publications:

J. Hu*, R.F. Hossain*, Z. S. Navabi, A. Tillery, M. Laroque, P. D. Donaldson, S. L. Swisher, S. B. Kodandaramaiah, Fully desktop fabricated flexible graphene electrocorticography (ECoG) arrays, bioRxiv 2022.07.25.501414; doi: https://doi.org/10.1101/2022.07.25.501414 (Preprint Paper)

R. F. Hossain*, **J. Hu***, Z. S. Navabi, A. Tillery and S. B. Kodandaramaiah, "High-performance, Conformable, Stencil Fabricated Graphene μ-ECoG Array," 2021 IEEE Biomedical Circuits and Systems Conference (BioCAS), 2021, pp. 01-04, doi: 10.1109/BioCAS49922.2021.9644954.

Abstract

Flexible Electrocorticography (ECoG) electrode arrays that conform to the cortical surface and record surface field potentials from multiple brain regions provide unique insights into how computations occurring in distributed brain regions mediate behavior. Flexible ECoG devices requiring highly specialized microfabrication methods provide high-density electrode arrays. However, these fabrication methods challenge scientists with only bio-backgrounds to fabricate customizable, low-cost, flexible ECoG devices with relatively lower resolution than commercially available devices. Here we present a fully desktop-fabricated flexible graphene ECoG array. First, we synthesized a stable, conductive ink via liquid exfoliation of Graphene in Cyrene. Next, we have established a stencil-printing process for patterning the graphene ink via laser-cut stencils on flexible polyimide substrates. Benchtop tests indicate that the graphene

electrodes have good conductivity of ~ 1.1×10^3 S·cm-1, flexibility to maintain their electrical connection under static bending, and electrochemical stability in a 15-day accelerated corrosion test. Chronically implanted graphene ECoG devices remain fully functional for up to 180 days, with average in vivo impedances of 24.72 ± 95.23 kΩ at 1 kHz. The ECoG device can measure spontaneous surface field potentials from mice under awake and anesthetized states and sensory stimulus-evoked responses. The stencil-printing fabrication process can be used to create Graphene ECoG devices with customized electrode layouts within 24 hours using commonly available laboratory equipment.

2.1 Introduction

Simultaneous neural computations occur in many brain regions, and interactions between these regions mediate behavior [2], [3], [58]. Disruptions to these interactions indicate neurological disorders such as Parkinson's disease [13] and traumatic brain injury [59]. Minimally invasive electrocorticography (ECoG) electrode arrays have been used to measure surface field potential for recording neural activities from several distributed populations of neurons at the brain surface [60]. Functionally, ECoG electrode arrays covering large brain regions need to be flexible to make adequate contact with the complex, convex surface of the brain [60], [61]. To this end, flexible, silicon substrate-based [62] and polymer substrate-based ECoG devices [7]–[19] have been developed. However, these devices were made using highly specialized micro- or nanofabrication techniques which require training and specialized fabrication equipment. Further, most neuroscience laboratories require rapid and flexible design alterations to adapt to various experimental contexts, which is hard to achieve in traditional microfabrication procedures. To

simplify the fabrication procedure, inkjet printing conductive materials such as silver nanoparticle inks [44] and conductive polymers like PEDOT:PSS [43] have been used to create flexible and reconfigurable ECoG electrode arrays. Tse approaches require expensive printers and still rely on specialized microfabrication techniques to insulate the electrode [45].

This work introduces a fully-desktop fabricated stencil-printed, flexible graphene ECoG electrode array fabricated using commonly available tools in neuroscience laboratories. Graphene has become an attractive material for realizing neural interfaces [30], [31], [46], [63], [64] due to its high conductivity [65], flexibility [66], transparency [67], stability [68], and biocompatibility [66]. We first formulated a stable conductive ink based on exfoliating Graphene in Cyrene. The ink was stencil-printed on a flexible polyimide substrate via laser-cut stencils. A similar procedure was applied to pattern a sacrificial Pluronic layer, a tri-block copolymer for defining the exposed electrodes. Subsequently, a silicone elastomer insulation layer was coated on the electrodes using a custom-built, microprocessor-controlled spin-coater to create functional ECoG electrode arrays. Most importantly, no aspect of the device fabrication needed access to specialized cleanroom facilities. The ECoG arrays exhibited excellent benchtop performance characteristics and *in vivo* recording capabilities. Using this methodology, the proposed devices can be fabricated within 24 hours and require a level of complexity and skill comparable to the assembly of tetrode devices [69]. The flexible Graphene ECoG devices were chronically implanted in mice and demonstrated the ability to record surface field potentials for up to 180 days.

2.2 Approach

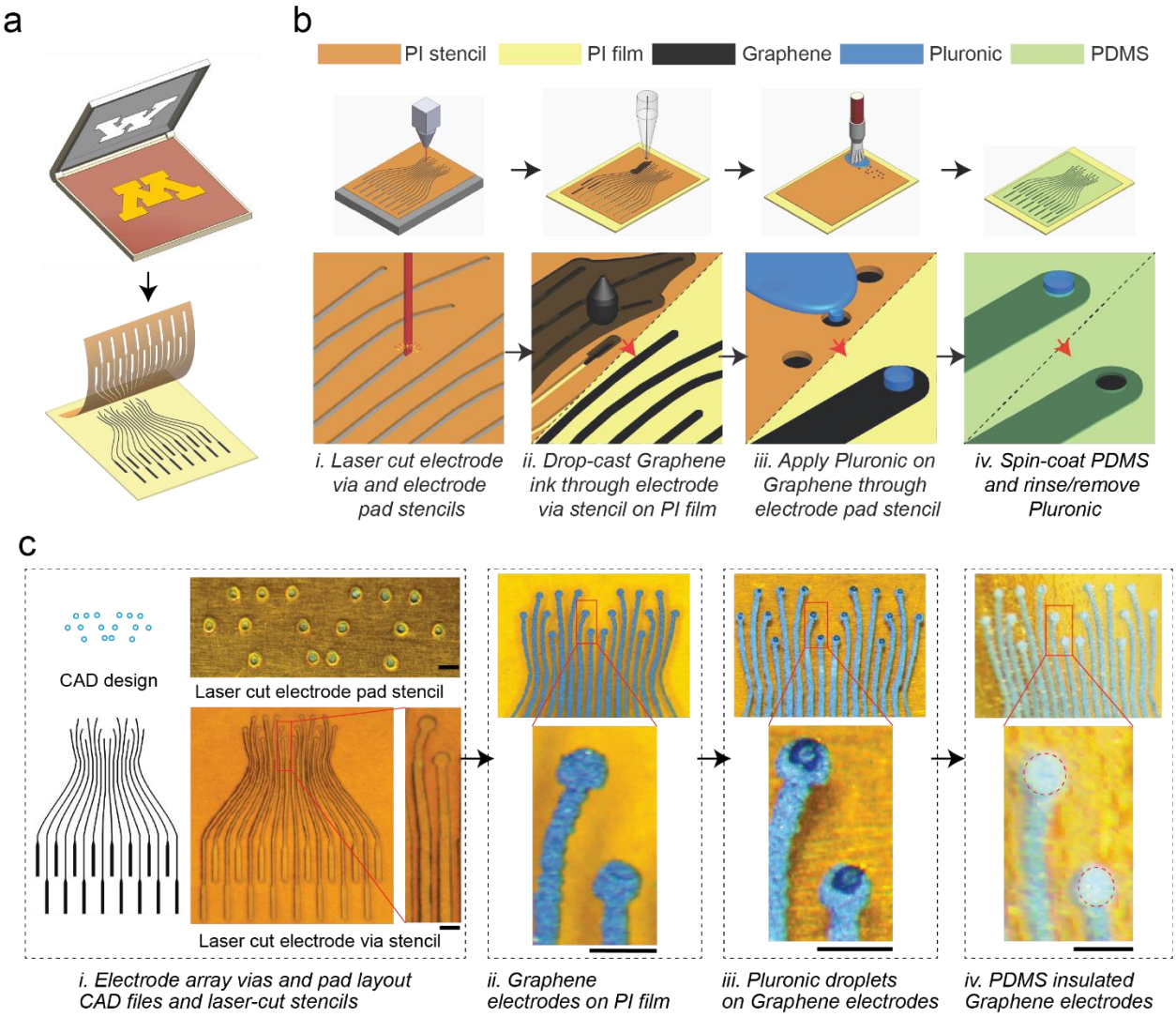

Figure 2.2.1 | Stencil-printed flexible graphene ECoG array: (a) stencil-printing adapted from screen-printing to realize flexible neural interfaces. **(b)** Schematic of the graphene ECoG electrode array fabrication procedure. (i) Stencils are cut from insulating polyimide tape (PI) using a desktop laser; (ii) after tape-transferring the stencil onto a PI film, graphene ink was drop-cast via stencil on the PI film to pattern the electrode traces, followed by annealing; (iii) After removing the electrode stencil from the PI film, Pluronic is deposited through the electrode pad stencil on the graphene electrodes; (iv) Once Pluronic solidifies, the electrode pad stencil is removed from the graphene electrode array carefully. Diluted PDMS is spin-coated to form the insulating layer. After PDMS cures, Pluronic is rinsed away to expose the electrode pads. **(c)** (i) Computer-aided design (CAD) drawing and laser-cut stencils of electrode array

vias and electrode pads. (ii) The patterned graphene electrode on PI film. (iii) Pluronic droplets on graphene electrodes. (iv) PDMS-insulated graphene electrodes. Scale bars indicate 500 µm.

We sought to engineer a flexible graphene ECoG device that could be entirely fabricated using available tools and equipment in most neuroscience laboratories. Previous work has been done on stencil-printed graphene electronics [70]–[73], but fully desktop fabricated µ-ECoG arrays implanted in mice have not been developed. The fabrication procedure required first a graphene ink which can be used to build electrodes and retain electrical performance after chronic implantation. Second, we sought to establish a simple process for achieving reconfigurable electrode arrays for use in small animals. In this study, we used graphene exfoliated in Cyrene solvent to create a high-performance conductive ink that could be patterned on a polyimide film using a stencil-printing technique (**Fig. 2.2.1a**).

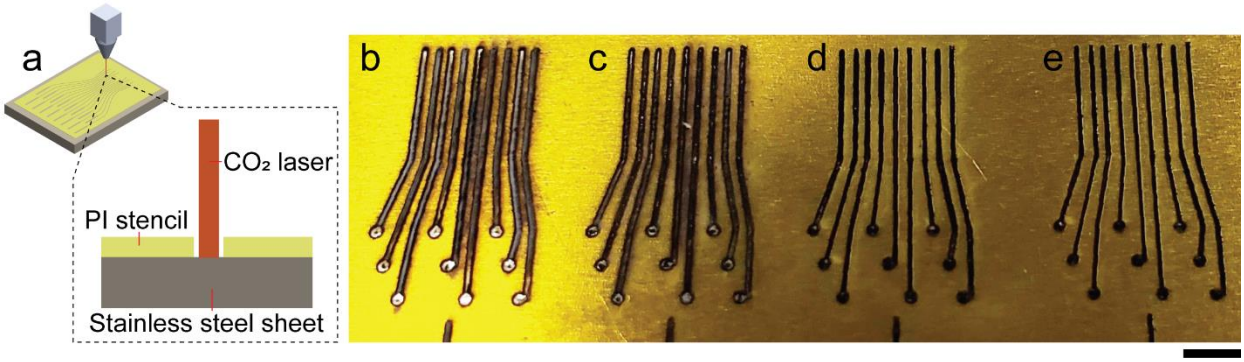

Figure 2.2.2 | Laser-cut stencil characterization. (a) The 2D schematic of laser cutting the stencil of electrode vias. The stencil was cut using a commercial CO2 laser cutter (PLS6.140D, Universal System) through the PI tape supported by a stainless-steel sheet. (b)-(e) Images of laser cut stencils at different power and speeds (b) A laser power setting of 10% and speed setting of 50% failed to create a distinct boundary between 2 neighboring electrodes. (c) A laser power setting of 10% and a speed setting of 100% created fully etched vias with distinct boundaries between electrode

tracks. (d) At a laser power setting of 5% maximum and speed setting of 100% maximum, the laser could fully cut through the PI tape but had carbonized residue filling in the stencil, which was hard to remove. (e) At a laser power setting of 2.5% maximum and speed setting of 100% maximum, the laser could not fully cut through the PI tape. The scale bar indicates 2 mm. We chose the settings in (c) for further experiments.

The overall fabrication procedure is shown in **Fig. 2.2.1a**. In the first step, stencils for patterning the graphene electrodes and a sacrificial layer of Pluronic defining the exposed electrode pads were created using a desktop laser cutter (**Fig. 2.2.1a. i, Fig. 2.2.2a**). The desktop laser cutter achieved a minimum inter-electrode (center to center) distance of ~ 400 µm. To reliably create isolated electrodes without any spurious interconnects, we used the inter-electrode distance of 500 µm in the stable design in which the electrode trace width is approximately 200 µm (**Fig. 2.2.1b, c**). This inter-electrode distance (500 µm) depended on the laser power and cutting speed of the laser cutter, which was experimentally optimized (**Fig. 2.2.2b**).

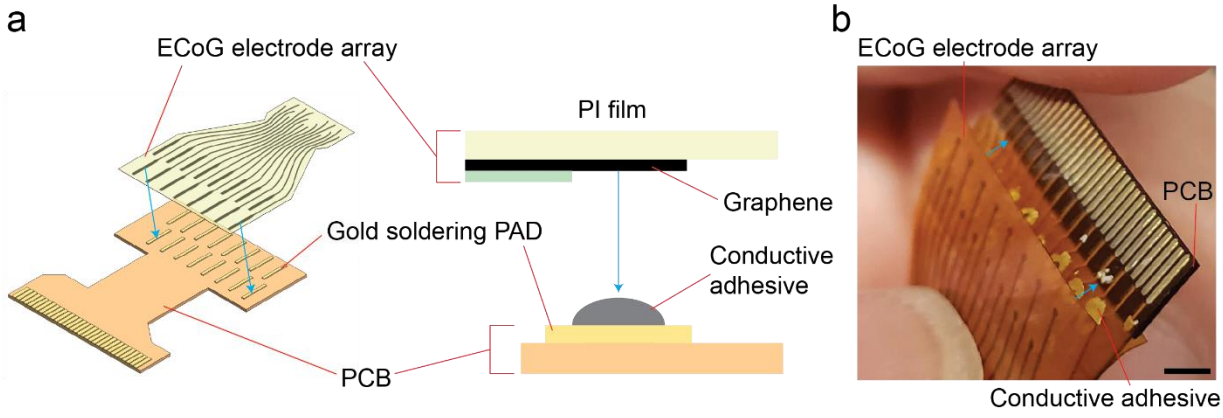

Figure 2.2.3 | bonding between PCB and ECoG electrode array: (a) 2D and 3D schematic of the bonding between the graphene ECoG array and interface PCB using conductive adhesive. **(b)** Photograph illustrating graphene ECoG array and interface PCB at the bonding sites. The scale bar indicates 2 mm.

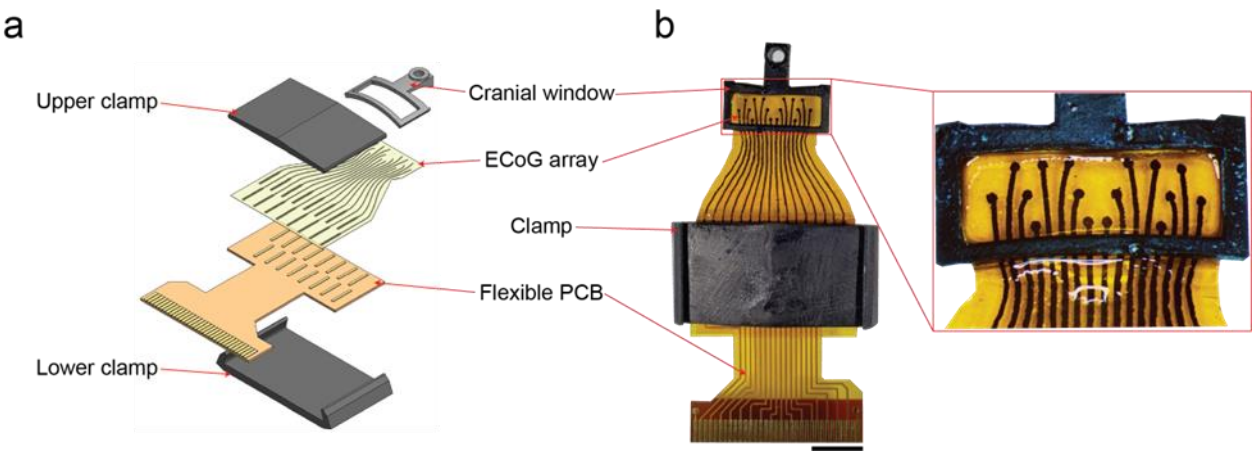

Figure 2.2.4 | **whole ECoG device assembly: (a)** CAD rendering of the whole implant assembly. The PDMS-insulated graphene ECoG electrode array is first bonded to a flexible PCB using silver epoxy adhesive to connect the electrodes with the PCB's gold pads. A 3D-printed clamp mechanically reinforces the bonded PCB and ECoG array. **(b)** Photograph of a fully assembled 16-channel graphene ECoG device. Scale bar indicates 5 mm.

The laser-cut stencil was overlaid on a flexible polyimide (PI) film, followed by drop-casting graphene ink to pattern the electrode arrays (**Fig. 2.2.1a. ii**). After drop-casting, the PI film with the stencil was annealed at a low temperature of ~ 100 °C to evaporate the excess Cyrene solvent. Then, the stencil was stripped, and the electrode array was annealed at a high temperature of ~ 300 °C (**Fig. 2.2.1c**). At room temperature, the second stencil for patterning the sacrificial Pluronic layer was overlaid on the substrate (**Fig. 2.2.1a. iii**). A fine paintbrush was applied to Pluronic on the electrode pad areas (**Fig. 2.2.1a. iii**). After removing the stencil, the Pluronic was allowed to solidify overnight (**Fig. 2.2.1c. iii**), then the array was spin-coated with diluted silicone elastomer to create the insulating layer. Once the elastomer was cured, the electrode array was gently rinsed in warm water to remove the sacrificial Pluronic covering the electrode pads, resulting in an insulated electrode array with exposed electrode sites for interfacing with a printed circuit board (PCB) (**S. Fig. 2.2.3a**) and exposed electrode pads with an average diameter of ~ 300 µm for

interfacing the brain. Once the electrode arrays were fabricated, they were integrated into a 3D printed frame adapted from our previous work [44], [52], [53]. The PCB interface was bonded to the ECoG array using conductive epoxy (**Figure 2.2.3**) and mechanically reinforced using a custom 3D printed clamp (**Fig. 2.2.4a, b**). The fabrication procedure relied entirely on common equipment such as a laser cutter and stereolithographic 3D printers, ubiquitous in nearly every university maker space. The electrode annealing was performed using a laboratory hotplate. Spin-coating was performed using a homebuilt microprocessor-controlled spinner, but off-the-shelf low-cost speed-controllable spin coaters under $1000 can also serve the purpose.

2.3 Results

Formulation of graphene inks and material characterization

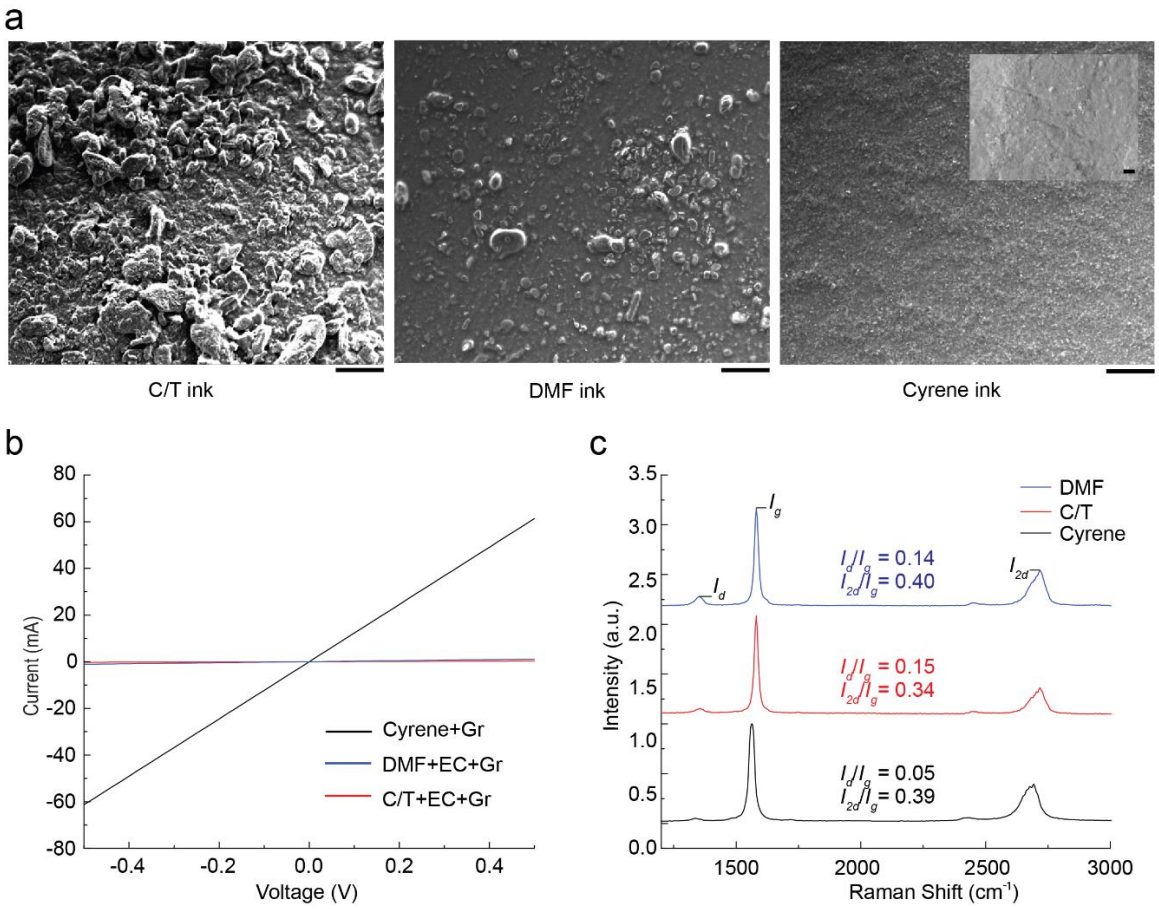

Figure 2.3.1 | Material characterization of graphene films using three graphene inks: (a) SEM images of the surface morphology of graphene films drop-cast onto a SiO2/Si substrate. The inset in the top right image shows the higher magnification image. Scale bars indicate 200 μm, while the scale bar in the inset indicates 2 μm. **(b)** Current-voltage characteristics of three exfoliated Gr inks. **(c)** Raman spectrum of the three graphene films at room temperature, showing distinct Raman D, G, and 2D-band peaks, where the Id/Ig ratio was lower for the film originated formed from Cyrene Cyrene-exfoliated graphene ink.

We formulated three graphene inks for stencil fabrication by exfoliating graphene in Cyrene, Dimethylformamide (DMF) [74]–[77], and Cyclohexanone/Terpineol (C/T) [66], [78], [79]

solvents, using a top-down liquid-phase exfoliation (LPE) technique through ultra-sonication (see **Methods** for details). Graphene inks in DMF and C/T have already been used in optoelectronic, photovoltaic, and biomedical applications [66], [75]–[80]. More recently, Cyrene demonstrated near-ideal physical properties for graphite exfoliation and the production of graphene dispersions [81]. Graphene exfoliated in Cyrene for the same sonication time of 2 hours resulted in drop-cast films with sub-micrometer surface flakes, while graphene in DMF and C/T ink produced rougher films with much larger surface clusters (**Fig. 2.3.1a**).

As shown in **Figure 2.3.1c**, the Raman spectroscopy was performed on spin-cast films from the three ink samples. The I_d/I_g ratio for highly disordered graphitic films like those generated from annealed graphene flakes increases with crystallite (i.e., flake) size [82]. The I_d/I_g ratio for the Cyrene-exfoliated graphene sample is the lowest, indicating it has the least average distance between defects (< 1 nm), implying that this sample is composed of the smallest flakes of the three inks, which have been annealed into a mainly sp^2 amorphous carbon structure [83]. Flake size is a determinant of the overall packing density, with a smaller flake size enhancing inter-platelet connectivity, resulting in higher conductivity [66]. Further, if needed, smaller flake sizes are desirable for uniform patterning through stencils or inkjet printing[66], [70]. The thickness of the drop-cast graphene inks were measured with a surface profiler, where the Cyrene+Gr, C/T+EC+Gr, DMF+EC+Gr films' thickness were measured to be 5.84 μm, 12.93 μm, and 8.08 μm, respectively.

We next assessed the current-voltage characteristics of the three graphene films at room temperature (**Fig. 2.3.1b**). At 0.5 V, the current was measured to be ~ 1.1 mA for DMF+EC+Gr

sample, ~ 0.2 mA for C/T+EC+Gr, and ~ 61 mA for Cyrene+Gr. Following the calculation in the method session, this finding corresponds to the highest conductivity of the Cyrene ink sample (~ 1.1 × 10^3 S·cm−1). These results indicated that Cyrene was an adequate solvent for formulating the exfoliated graphene ink. The characteristics of small flake size and high conductivity of the exfoliated graphene in Cyrene indicate its potential for inkjet printing [84]. This work explored stencil printing to simplify the fabrication process for patterning the ECoG electrodes. Further experiments in this work involved devices made using graphene exfoliated in Cyrene.

Benchtop characterization of stencil fabricated graphene ECoG electrode arrays

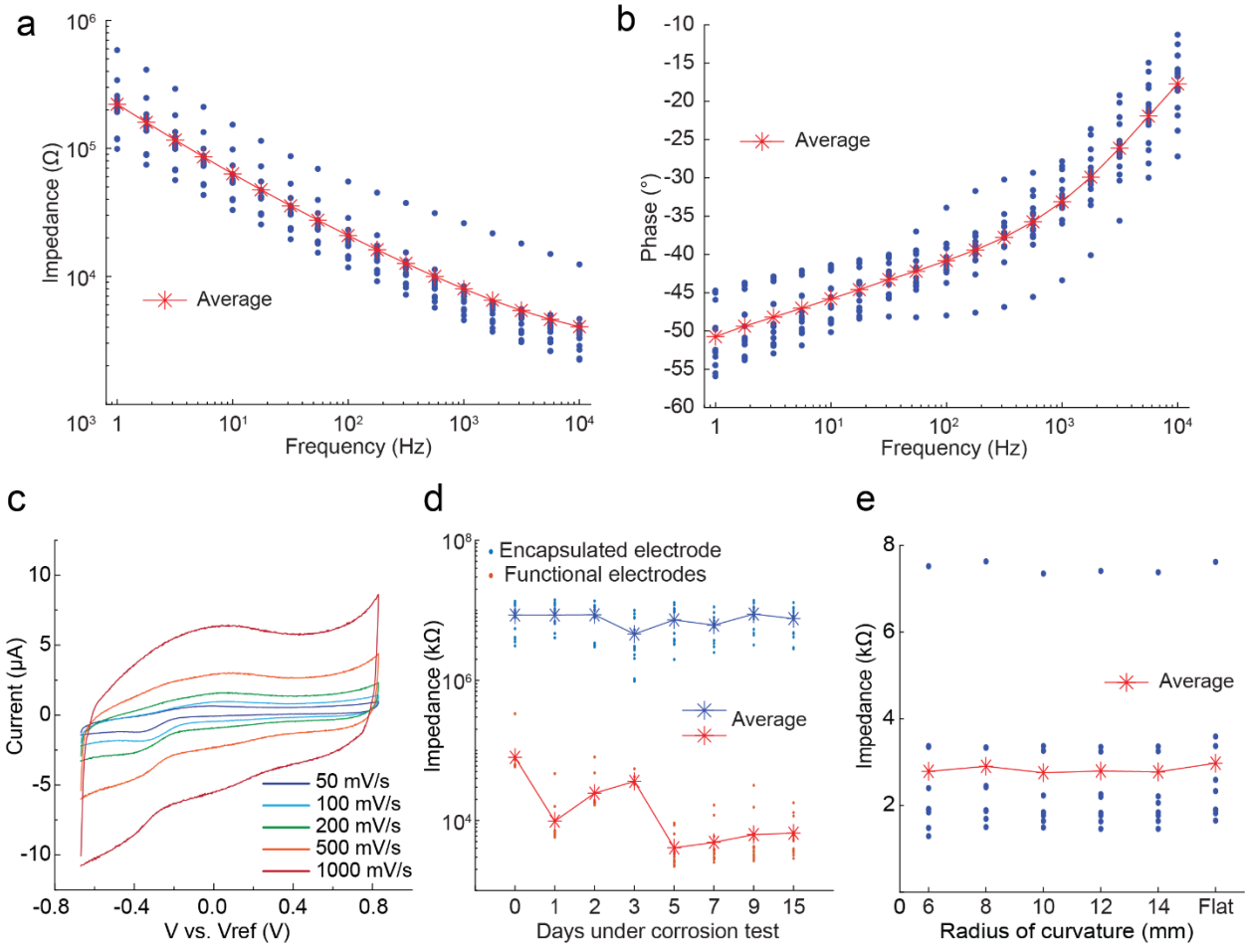

Figure 2.3.2 | Electrochemical characterization of the ECoG electrode: **(a)** Impedance magnitude at different frequencies ranging from 1 Hz to 10 kHz of electrodes made by stencil printing with Cyrene + graphene ink. **(b)** Phase angle at different frequencies ranging from 1 Hz to 10 kHz made by stencil printing with Cyrene + graphene ink. **(c)** Cyclic voltammetry of the graphene ECoG electrode in PBS at different scan rates in 50 to 500 $mV \cdot s^{-1}$. **(d)** Change in impedance magnitude as a function of time during an accelerated corrosion test. Each device has 16 electrodes with exposed electrode pads (red) and 16 electrodes with PDMS capsulated pads (blue). **(e)** The change of impedance magnitudes at 1 kHz as a function of radii of bending curvatures for nine identical straight graphene 10 mm long ECoG electrodes.

Cyclic voltammetry (CV) was used to evaluate the electrochemical stability of graphene electrodes [85]. The CV of the graphene electrode (n = 1) was measured at potentials with various scan rates ranging from 50 mV/s to 1000 mV/s. According to the shape of the plotted curves, both double-layer capacitance and pseudo-capacitance exist in the electrode (**Fig. 2.3.2c**) [86]. The capacitance value was extracted from the current (at 400 mV) vs. scan rate from the CV curve, where the linear fit slope approximated the capacitance and was calculated to be ~ 10 nF at 400 mV.

Electrochemical impedance spectroscopy (EIS) measured over a frequency range of 1 Hz to 10 kHz (**Fig. 2.3.2a**) was performed on a graphene ECoG device with 15 functional electrodes (We used a sample of 15 electrodes from one device to ensure the fabrication condition remains the same). The phase angle shows the typical capacitive behavior (near 80°) at 20 Hz but gradually becomes more resistive at higher frequencies (**Fig. 2.3.2b**). At high frequencies ranging from 1 kHz to 10 kHz, the relatively low impedance magnitudes are attributed to the stray capacitance and the Ohmic resistance of the electrolyte solution and interconnect [87]. The EIS of the stencil-

printed graphene electrode presents similar impedance characteristics as a previously reported ECoG array of monocrystalline graphene layers [31].

To evaluate the durability of the PDMS insulator and stability of graphene electrodes, we used ECoG arrays with 16 exposed electrode pads as the controls and the ECoG arrays with 16 electrode pads fully encapsulated with PDMS as the test devices in the accelerated corrosion test (**Fig. 2.3.2d**). Accelerated corrosion tests are typically used to evaluate the durability of devices by maintaining the devices in 1X PBS solution for long durations at high temperatures (60°C). Such tests simulate a fivefold acceleration in device degradation as compared to devices kept at physiological temperatures [36]. Based on these metrics, we performed accelerated corrosion tests lasting 15 days to evaluate the impedances for a project 75-day period. At the end of the 15-day accelerated corrosion tests, the electrodes had an average impedance of 6.49 ± 4.16 kΩ ($n = 16$), while devices fully encapsulated with PDMS all had impedances > 1 MΩ. These results indicate that the potential lifetime of the electrodes is at least 75 days at body temperature of 37°C.

The planar ECoG electrode array is typically bent to conform to the mouse's convex dorsal cortex with an approximate radius of curvature of 12 mm [53]. Therefore, it is important to investigate the relationship between the electrode impedance and the bending radii of curvature. The impedances of 9 identical 10 mm long straight graphene electrodes were measured at 1000 Hz when the electrodes were placed on a flat surface and then bent at various radii of curvature using a custom measurement rig (**S. Fig. 3)**. No significant difference in the electrode impedance magnitudes on a flat surface or at different radii of curvature (14 mm to 6 mm) could be found (**Fig. 2.3.2)**. Thus, the graphene electrodes patterned on the flexible PI substrates can be bent and

conform to the dorsal cortical surface of the mouse brain with minimal effect on the electrode impedance.

In vivo experiments

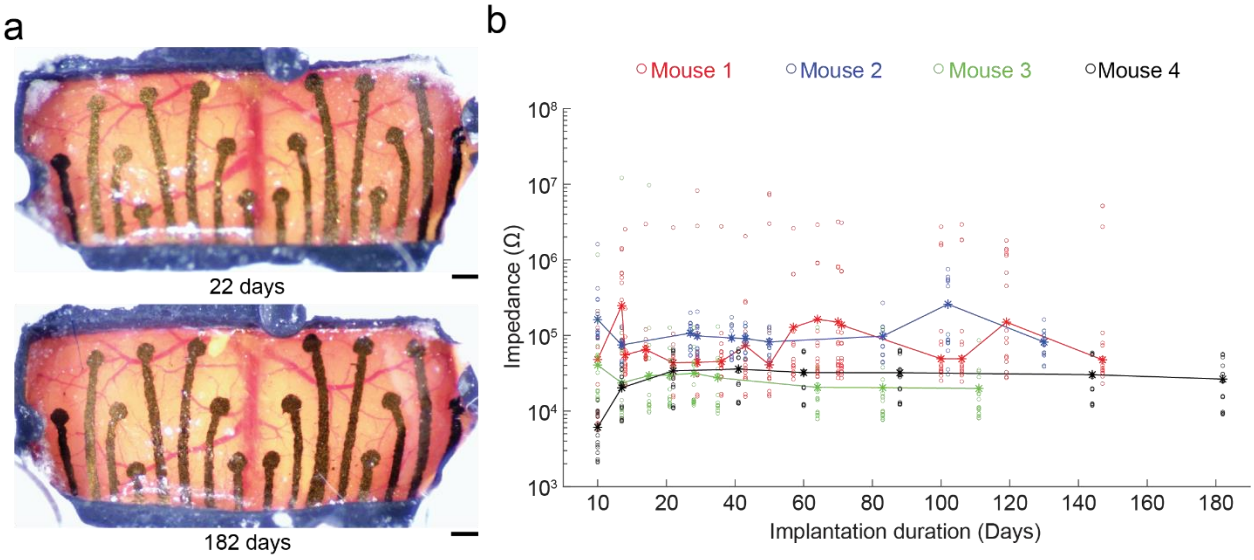

Figure 2.3.3 | *In vivo* performance of the graphene ECoG devices: (a) Optical microscope images taken at 2 timepoints after chronic implantation of ECoG device on a C57BL/6 mouse (#4 shown in **(b)**. Scale bars indicate 500 µm. (**b)** Impedance magnitude at 1 kHz of 64 electrodes in 4 implanted mice. Dots indicate individual electrode impedance values. Stars indicate the average impedance of the 16 electrodes in each device.

The graphene ECoG devices were implanted in multiple mice to evaluate the *in vivo* recording capabilities. The overall array dimension was ~ 9 mm x 4 mm, covering most sensory cortex areas bilaterally (**Fig. 2.3.5b**). Representative microscope images of one such implanted mouse taken on days 22 and 182 after implantation are shown in **Fig. 2.3.3a**. No visible neuroimmune response could be found, such as Dural thickening and tissue encapsulation in these devices. Most of the inner surface of the implant was covered by a PDMS insulation layer (**Fig. 2.2.1c**

iv). PDMS itself is a biocompatible material for long-term cranial implants [32]. The longest duration of implantation assessed was 21 weeks. The impedances of the electrodes were periodically measured throughout the implantation (**Fig. 2.3.3b**). Across 4 mice, 61 electrodes (out of 64) remained functional, with an average impedance magnitude of 24.72 ± 95.23 kΩ (n = 61) at 1 kHz. Three electrodes lost their connections on mouse 1 at the measurement of day 10. Based on previous work describing a graphene ECoG device with similar electrode sizes, the impedance of functional ECoG electrodes was expected to be lower than 600 kΩ at 1 kHz [30]. The average electrode impedances of all four devices evaluated in this study remained less than 600kΩ throughout implantation (n = 61/64 electrodes). Therefore, our graphene electrode arrays can be used for chronic *in vivo* studies.

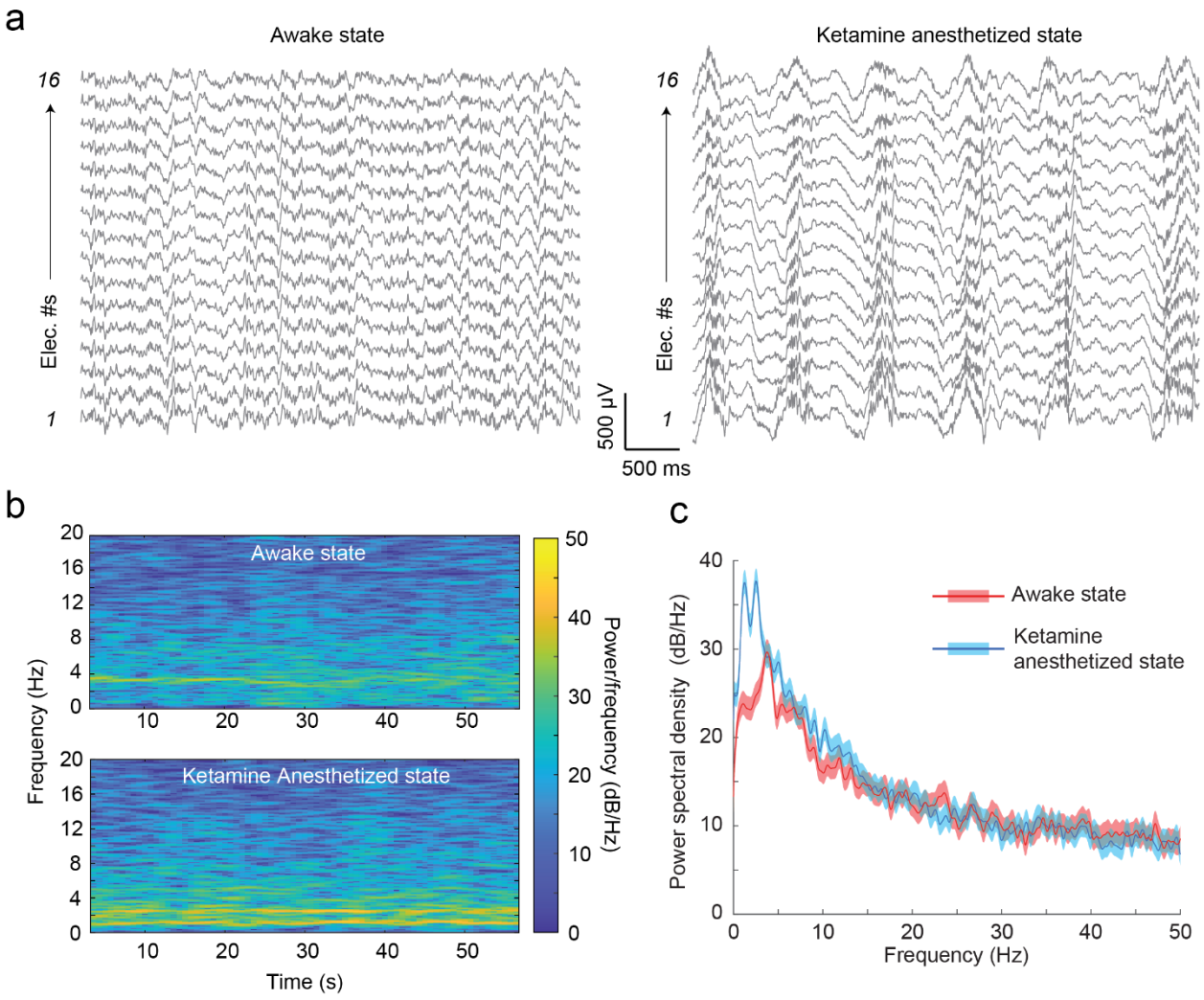

Figure 2.3.4 | Ketamine-induced brain response: (a) Raw surface field potential recordings from the electrodes in awake and Ketamine anesthetized states. **(b)** Frequency spectrogram of electrode 5 is shown in (a) in awake and anesthetized states. **(c)** Average power spectral density (PSD) of recordings of all electrodes shown in (a) in awake and anesthetized states.

ECoG recordings were performed in head-fixed mice while fully awake and under Ketamine-anesthesia to demonstrate the functional use of the graphene ECoG devices. The raw recordings obtained from all 16 electrodes in both states are shown in **Figure. 2.3.4c**. Consistent with previous observations [88]–[90], induction of the anesthetized state via Ketamine resulted in low-frequency

oscillations at the delta frequency (0.5 – 4 Hz) throughout the cortex (**Fig. 2.3.4a**). These delta oscillations had signal peak-to-peak amplitudes of approximately 500 µV, much higher than the awake state's amplitude of ~ 200 µV (**Fig. 2.3.4a**). The spectrogram in **Figure. 2.3.4b** also presents a higher signal power density at 0.5 – 4 Hz at the anesthetized state, matching the power spectral density (PSD, **Fig. 2.3.4c**). The result indicates that all 16 device channels were functional for measuring brain activity.

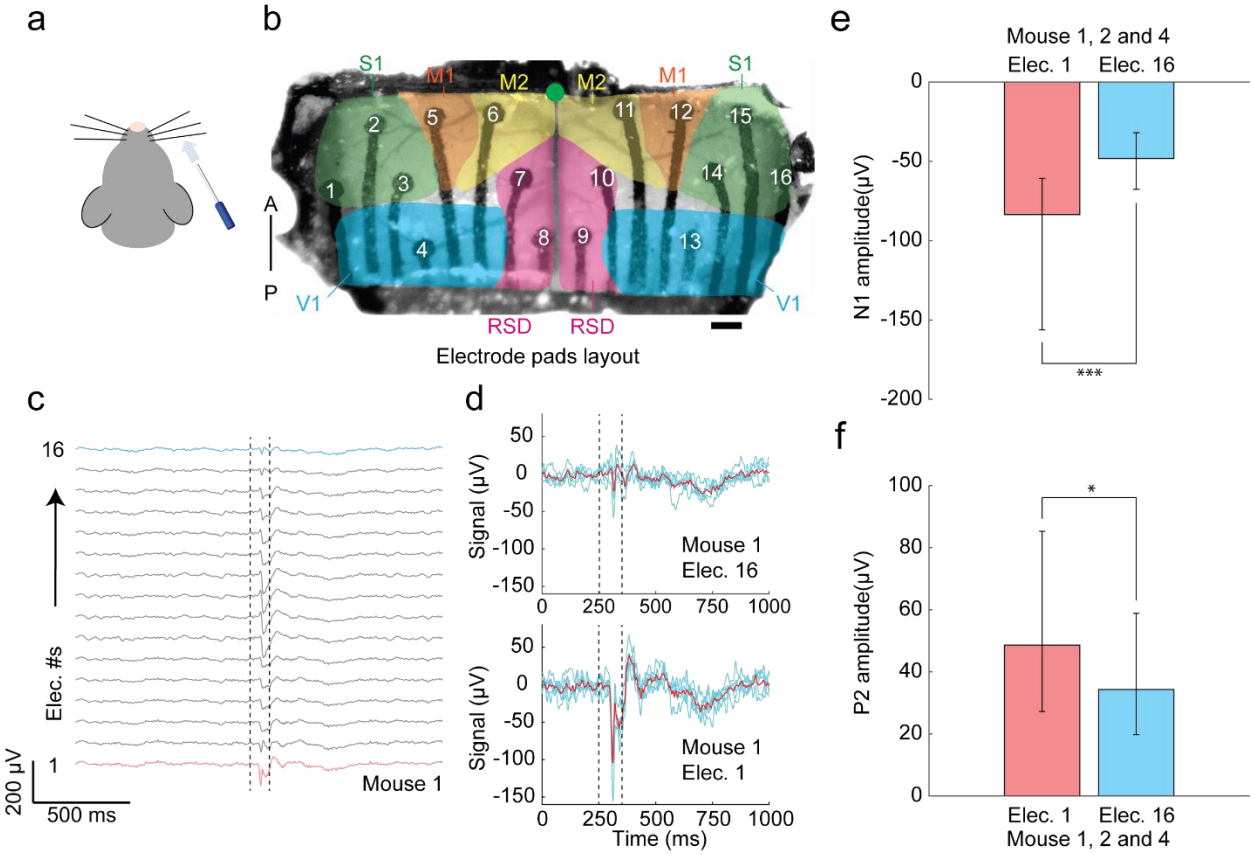

Figure 2.3.5 | Sensory stimulus-evoked responses recorded by the graphene ECoG devices. (a) Air puff stimulus was applied to the right whiskers. **(b)** Locations of electrode pads: electrodes 1 - 3 and 14 - 16 were located in the primary sensory cortex (S1); electrodes 4 and 13 were located in the visual cortex (V1); electrodes 5, 6, 11, and 12 were located in the primary motor cortex (M1/M2). Electrodes 7, 8, 9, and 10 were located in the Retrosplenial cortex (RSD). Green dot indicates Bregma. Scale bar indicates 500 µm. **(c)** Average ECoG signals responses to air-puff

stimuli (n = 138) in 20-min recording were collected from 16 electrodes of Mouse #1. Dotted lines indicate the on- and off-state of the air puff stimulus. Red line marks the signal of contralateral electrode 1, and blue line marks the signal of ipsilateral electrode 16 **(d)** Average ECoG signals captured by the contralateral electrode 1 (top) and ipsilateral electrode 16 (bottom) in response to repeated whisker stimulus (n = 5) in mouse 1. Blue lines indicate individual trials. Red line denotes the average signal response. **(e)** Comparison of surface field potential of depolarization's peak amplitudes recorded by the contralateral electrode 1 vs. ipsilateral electrode 16 on mice 1, 2, and 4 ($P < 0.001$, *t-test*). **(f)** Comparison of local field potential repolarization's peak amplitudes recorded by the contralateral electrode 1 vs. ipsilateral electrode 16 of the graphene ECoG on mice 1, 2, and 4 ($P < 0.01$, *t-test*).

Furthermore, the graphene ECoG devices demonstrated the ECoG recordings of stimuli-evoked brain activity in response to sensory stimuli. The stimuli were the brief puffs of air (100 ms) given to the right whiskers of mice in a randomized fashion during the awake state under head-fixation (**Fig. 2.3.5a**). The stimuli resulted in whisking and the motor response observed in the experiments. Broad activation of most of the cortex in response to the stimuli was observed and possibly caused by the startle response (**Fig. 2.3.5c**). Channels 1 and 16 were individually located at the contralateral and ipsilateral sensory cortices (S1) (**Fig. 2.3.5b**). Channel 1 has higher signal amplitudes of negative peak N1 and positive peak P2 than channel 16 (**Fig. 2.3.5d**). Three animals (mouse #1, mouse #2, and mouse #4) were tested to study and analyze the signal difference between Channel 1 and 16. As shown in **Figure. 2.3.5e** and **f,** the average peak values N1 in electrodes 1 vs. 16 were - 83.60 ± 23.16 µV vs. - 48.20 ± 12.29 µV ($p < 0.001$, *t-test*) on all three mice; the average peak values P2 in electrode 1 vs. 16 were 48.64 ± 19.96 µV vs. 34.34 ± 11.28 µV ($p < 0.05$, *t-test*) on all three mice. Both N1 and P2 peaks of stimuli evoked response measured by electrode 1 placed on the left somatosensory cortex (contralateral to the right whisker experienced air-puff stimulation) have significantly higher signal amplitude than electrode 16 located on the right somatosensory cortex. Thus, the graphene ECoG electrode arrays successfully

captured the evoked response to the lateral right whisker air-puff stimulation. These results are consistent with previous work done in our group [52], [91].

2.4 Discussion

Here, we demonstrate for the first time a fully desktop fabricated, stencil-printed, liquid exfoliated, graphene-based, 16-channel ECoG electrode array on a flexible polyimide substrate, implanted on the rodent dorsal cortex for high-resolution neurophysiological recording. The highly stable graphene ink formulated by exfoliating graphene in a biocompatible solvent Cyrene [92], demonstrated a high conductivity ~ 1.1×10^3 $S \cdot cm^{-1}$. Alongside the electrochemical analysis, mechanical bending tests showed no significant change in electrode impedance at a flat surface and various radii of curvature ranging from 14 mm to 6 mm. Fully functional devices and the encapsulation of PDMS insulation were highly stable even under the accelerated aging environment, maintaining an average impedance of ~ 6.49 ± 4.16 kΩ on day 15. Furthermore, the electrodes remained functional with an average impedance magnitude of 24.72 ± 95.23 kΩ (1000 Hz) throughout the implantation. Thus, our graphene ECoG arrays are robust neural interfaces that can be applied for chronic electrophysiology studies in mice.

To our knowledge, all the existing micrometer-scale ECoG devices are fully or partially fabricated using microfabrication or specialized techniques [32]–[37], [39], [93]–[95], resulting in high cost and low accessibility to neuroscience laboratories. In our method, the stencils determining the layout of the electrodes can be rapidly reconfigured using CAD tools and fabricated using desktop laser-cutters available in most university fabrication shops. The graphene ink can be formulated using standard lab equipment, and the patterned electrodes can be sintered on a laboratory hotplate.

The insulation layer can be deposited by a homebuilt, microcontroller-based spinner or a low-cost off-the-shelf spin coater. We have created the first fully desktop fabricated, flexible micrometer-scale ECoG array that can be chronically implanted in mice. These results point a way forward for creating robust, open-source, flexible neural interfaces that can be widely used in basic and translational neuroscience research.

Some limitations and concerns of the electrode characterization tests and results should be clarified and discussed. First, the conductivity of the Cyrene graphene electrode was measured to be ~1.1 X 10^5 S/m, which is enough for building neural probes compared with some PEDOT:PSS composite materials with a conductivity of $3.23 \pm 0.75 \times 10^2$ S/m from the previous study [47]. However, the conductivity of the stencil-printed multilayer graphene electrode (~1.1 X 10^5 S/m) is not comparable with monolayer graphene ($1.46 \pm 0.75 \times 10^6$ S/m) synthesized by chemical vapor deposition [96]. To improve the conductivity of the ECoG electrode made by this desktop fabrication method, new conductive inks like inkjet printable gold nanoparticle ink (8.0×10^6 S/m) can be considered [97]. Secondly, in the accelerated corrosion test, for maintaining the samples in the exact same fluid environment, the 50ml centrifuge tube we used could only fit 2 devices of total 32 electrodes (one functional device of partially PDMS-encapsulated to evaluate the stability of graphene electrode and one device of fully PDMS encapsulated to evaluate the durability of the PDMS insulation layer). Though the test results of durable PDMS (> 1 MΩ after day 15) and stable graphene electrodes (6.49 ± 4.16 kΩ after day 15) indicate the potential for long-term implantation, the sample size is too small to give a conclusion. Also, the decreasing impedance values of graphene electrodes from day 0 to day 5 (**Fig. 2.3.2d**) might indicate vapor penetration through PDMS, which is water-repellent but permeable to water vapor

[98]. To resolve this possible vapor penetration, new flexible insulation material SU-8 [93] can be introduced in the future version of the device. Thirdly, the impedance values (24.72 ± 95.23 kΩ at 1000 Hz, n = 61) of the implanted ECoG devices have high variability. In the stencil printing fabrication method, drop-casting conductive ink of exfoliated graphene flakes through the laser-cut stencil made the graphene electrode's thickness hard to control, possibly leading to the high impedance variability. To mitigate this, spin-coated or drop-casted PEDOT:PSS with smaller particle sizes can be explored to reduce the variability impedance, as demonstrated previously [91].

We also identified some limitations to the proposed approach. First, the minimum feature size is limited by the resolution of the desktop laser cutter to create the stencils. The ECoG devices with an inter-electrode (center to center) distance of ~ 500 µm can be patterned using the laser cutter for a stable fabrication quality, limiting the overall number and density of electrodes incorporated within a device. Second, the graphene ink needs to be annealed at high temperatures (> 300°C), limiting the substrates used for supporting the graphene electrodes. As an alternative, photonic sintering can be used instead of thermal annealing, allowing the use of other materials as substrates. For instance, the electrodes could be patterned on transparent polymers such as polyethylene terephthalate (PET) to create devices for simultaneous imaging and ECoG recording [45]. Though transparent graphene ECoG has been developed, it still requires cleanroom equipment [49]. Our desktop-fabricated stencil printing method does not apply to building transparent graphene ECoG, but off-shelf transparent conductive PEDOT:PSS ink can be a potential alternative [8] for making fully transparent ECoG.

Several directions can be pursued in the future, building upon the graphene ECoG devices presented in this work. The size of the implant can be extended to much larger regions of the brain [52], [53] so that the whole visual cortex and motor cortex can be included for performing ECoG recording over most of the cortical surface of the mouse brain [45]. The low and stable impedance of the electrodes can be leveraged for precise cortical micro-stimulation [31]. Miniaturization of electronic interface circuits can also allow deployment in freely behaving animals, potentially combined with imaging instrumentation for simultaneously tracking large-scale calcium dynamics [52]. Further, graphene has shown utility in passive sensing of electrical potentials and functionalizing to highly sensitive biochemical sensing [99]. Overall, our method can be scaled to mass manufacturing of flexible graphene-based biosensors at a low cost with a myriad of applications in biological sensings, such as electrocardiography [100], electromyography [101], and peripheral nerve interfacing [102].

2.5 Methods

Graphene inks formulation: The graphene inks were formulated by bath ultra-sonication of graphene powder, which was ground using a mortar pestle from a graphite rod (496561, Sigma Aldrich), in a mixture of Cyclohexanone:Terpineol (C/T) (398241 and 814759, Sigma Aldrich) at a ratio of 7:3, DMF(319937, Sigma Aldrich), and Cyrene (807796, Sigma Aldrich). An initial concentration of Ethyl Cellulose (EC) (EC 200646, Sigma Aldrich) at 2.5 wt% and 10 mg/mL graphene powder were then added in 10 mL C/T and DMF, treated for 2 hours in the Branson Bath Sonicator (CPX2800, Fisher Scientific) at 30 °C. No EC was added to the Cyrene ink as it produces excess bubbles resulting in bad drop casting. All three dispersions were kept idle for 24 hours to

precipitate the larger particles, which left pale gray precipitation at the bottom of the vials. The supernatant (~ 8 mL) inks were extracted and stored in clean vials.

Graphene sample preparation for Electrical Measurement:

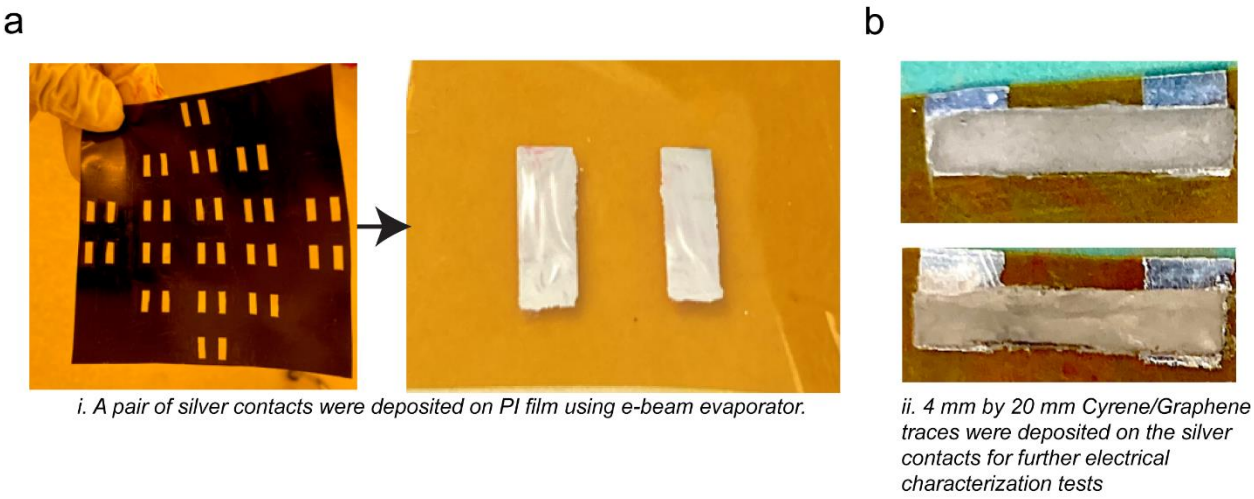

Figure 2.5.1 | Sample preparation for electrical characterization: (a) A pair of silver contacts were deposited on PI film using e-beam evaporator through a lithography mask. **(b)** 4 mm x 20 mm graphene trace was patterned on the silver contact for electrical characterization tests.

To carry out the initial electrical characterization of the graphene inks, high integrity metal contacts composed of silver (*Ag*) were first patterned with photolithography and deposited with an e-beam evaporator on the PI film, followed by drop-casting of 0.5 mL graphene ink in a rectangular area of 10.5 mm x 2 mm using a stencil (**Figure 2.5.1**). The sample was annealed at 350 ^{o}C for 90 minutes. A probe station with a parameter analyzer (B1500A, Agilent Technologies) was used to conduct 2-point-probe voltage-controlled measurements and data extraction to evaluate the current-voltage characteristics of three graphene films (**Fig. 2.3.1b**). The current density (A/cm^2)

was calculated from the measured current values (A) (**Fig. 2.3.1b**) divided by the cross-session area of the sample of 1.17×10^{-4} cm^2 (sample width of 2 mm × sample thickness of 5.84 μm of Cyrene graphene). The electric field (V/cm) was defined as applied voltage (V) (**Fig. 2.3.1b**) divided by the sample length of 1.05 cm. The conductivity (S/cm) of the graphene sample was calculated by dividing the current density (A/cm^2) by the electric field (V/cm).

Electrode array design and assembly:

Electrode array design: The layout of the graphene electrode array was rendered in computer-aided design software (SolidWorks 2021, Dassault) (**Fig. 2.2.1c**). The center-to-center distances between 2 neighboring electrode pads ranged from ~ 600 μm to 1 mm. The overall layout of the electrode array was designed to cover an area of ~ 9 mm long, extending bilaterally, with a width of ~ 4 mm posterior to Bregma (**Fig. 2.3.4b**). Electrodes 1-3 and 14-16 were in the primary sensory cortex (S1); electrodes 4 and 13 were located in the visual cortex (V1); electrodes 5-6 and 11-12 were located in the primary motor cortex (M1/M2), and 7-10 were located in Retrosplenial cortex (RSC).

Laser-cut stencils: To fabricate the stencils, a piece of 50 μm-thick insulating polyimide (PI) tape (High Temperature Tape, Bertech) with a size of 25.4 mm by 160 mm was adhered to a stainless-steel sheet and subsequently patterned by a CO_2 laser cutter (PLS6.140D, Universal System) (**Fig. 2.2.1a**). We tested the laser cutter's cutting precision on the PI tape and found that the inter-electrode pitch (center to center distance) of ~ 500 μm with power settings of 10% and speed settings of 100% can achieve the stable stencil (**Fig. 2.2.2b**). The electrode via stencil was

transferred to a polyimide film substrate using a scotch tape transfer method modified from previous work [103].

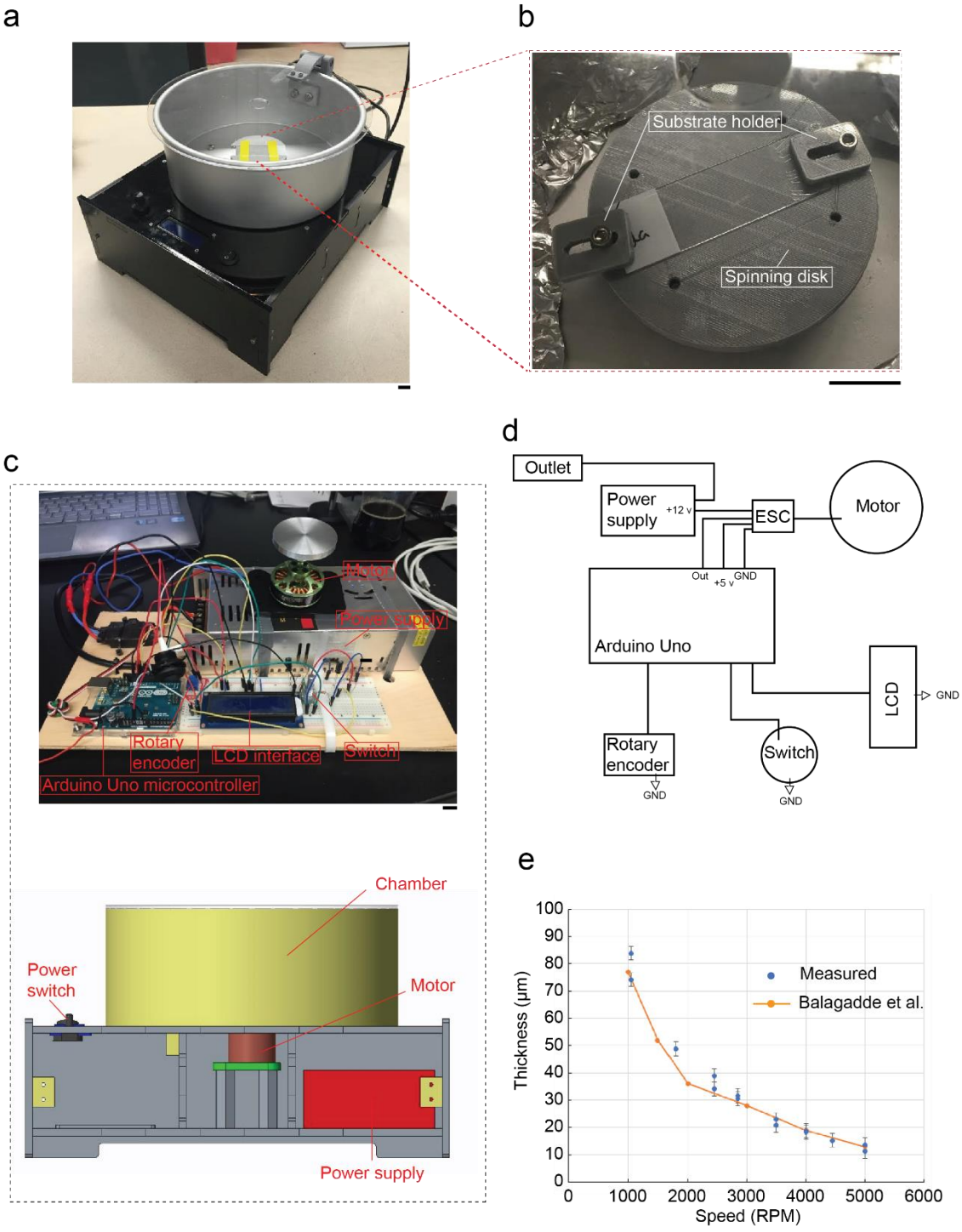

Figure 2.5.2 | Custom-built spin coater: (a) Photograph of a custom-built microprocessor-controlled spin coater. **(b)** The spin coater has one spinning disk with 2 substrate holder clamps that hold the substrate for spin coating. **(c)** The major components of the spin coater include a microcontroller, rotary encoder, liquid crystal display (LCD) interface, power switch, power supply, motor, and chamber. **(d)** Circuit layout. ESC in the schematic abbreviates electronic speed controller. **(e)** The relationship between spinning speed and PDMS thickness was obtained using the custom-built spin-coater compared to results obtained using a commercial spinner [1].

Graphene ink deposition: The graphene ink was manually drop-cast on the laser-cut mask and annealed at a high temperature (~ 350 °C) for 90 minutes. To evaporate the solvent completely, the hotplate temperature was ramped at ~ 10 °C/minute from 100 °C to 330 °C to evaporate the solvent completely. After annealing, the mask was carefully removed, leaving the patterned graphene channels on the polyimide film. A similar procedure was used to apply a sacrificial layer of Pluronic (F-127, Sigma Aldrich) after manually aligning the electrode pad stencil to the graphene electrodes. The sample was kept overnight at room temperature to solidify the Pluronic. Diluted Polydimethylsiloxane (PDMS) was spin-coated at 1500 rpm for 15s using a home-built desktop spin-coater (**Fig. 2.5.2**), then cured at 30 °C temperature for 15 minutes. For making the diluted PDMS, the tert-Butanol (471712, Sigma) was warmed at 45 °C and mixed with PDMS and SYLGARD 184 curing agent (761036, Sigma) at the weight ratio of 50:10:1. The Pluronic was released with a gentle flow of hot water at 45 - 60 ^{o}C to expose the electrode pads. Then the sample was annealed again at 100 °C for 30 minutes.

Implant assembly: The graphene ECoG device is an assembly of four major components: the stencil fabricated ECoG array, a 3D printed cranial window frame, a flexible printed circuit board (PCB) connector, and a 3D printed reinforcement clamp. The cranial window frame and the

reinforcement clamps were 3D-printed using a stereolithography 3D printer (Form 2, Formlabs). The PCB connector was custom-designed in Eagle (Autodesk Inc.) and fabricated by an online PBC manufacturer (PCBWay.com). To assemble the device, the ECoG electrode array was first bonded to the gold soldering pads on the flexible PCB connector using a conductive adhesive (8331 Silver Epoxy Adhesive, MG Chemical) (**Fig. 2.2.3**) by applying it manually with a sharp object. The interface was further mechanically reinforced using the 3D-printed clamp and followed by encapsulation with clear epoxy adhesive (Scotch-Weld Epoxy Adhesive DP100 Plus, 3M). The recording area of the stencil fabricated graphene electrode arrays was bonded to a 3D printed cranial window frame using epoxy adhesive (DP1000 Plus Clear, 3M) adapted from our previous work [52], [53] to realize the device illustrated in **Fig. 2.2.4b**. The cranial window defined a total recording area of ~ 4 mm x 9 mm, with a radius of curvature of 10 mm, to allow conformal implantation over the dorsal cortex immediately posterior to Bregma (**Fig. 2.3.4b**). A fully assembled device has a mass of ~ 1.3 g.

Benchtop testing of fully assembled devices:

CV (**Fig. 2.3.2c**), EIS (**Fig. 2.3.2a, b**), and accelerated corrosion tests (**Fig. 2.3.2d**) were performed on fully assembled graphene ECoG devices. EIS and CV measurements were conducted using a potentiostat (1010E, Gamry Instruments), with an Ag/AgCl reference electrode (Gamry Instruments) and a platinum wire as a counter electrode (1.0 mm diameter, Premion, 99.997%, Alfa Aesar) in room temperature 1X Phosphate Buffered Saline solution (D1408 PBS 10X, Sigma-Aldrich). EIS was performed with a 50 mV excitation voltage from 10 kHz to 1 Hz. Ten measurements were taken per decade. The CV was performed at varying scan rates from 50 – 1000 mV/s, with voltage limits set at ± 0.75 V vs. the open circuit potential.

The accelerated corrosion test was performed [104] by immersing 2 ECoG devices (one device has 16 exposed electrode pads, and one device has 16 fully PDMS-capsulated electrode pads) into 1X Phosphate-buffered saline (D1408 PBS 10X, Sigma-Aldrich) at an elevated temperature of 60 °C which is equivalent to a five-fold accelerated corrosion process at body temperature of 37 °C [36]. Impedances of the device were measured using the interface board (RHD2000, Intan Technologies) at 1000 Hz daily for 2 weeks.

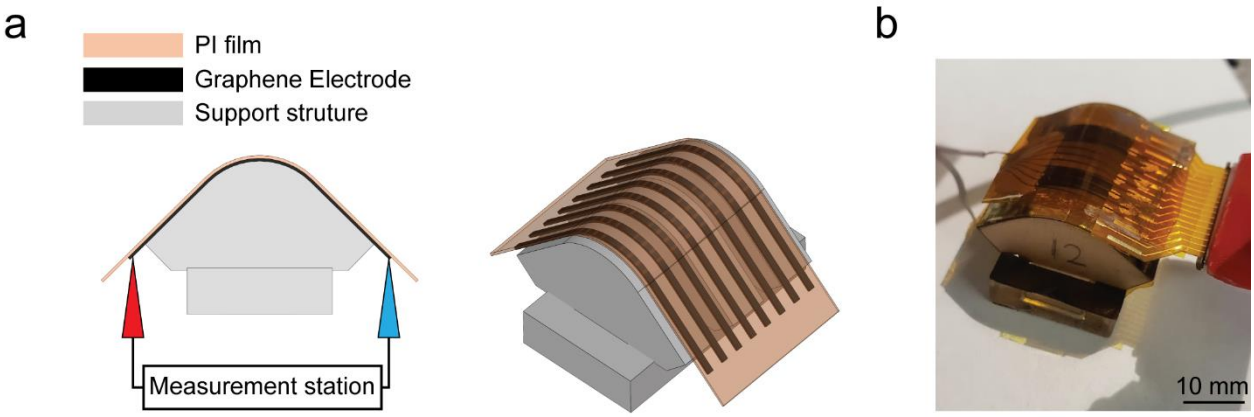

Figure 2.5.3 | Bending test. (a) The 3D and 2D schematic of the bending test setup. 3 identical electrodes built by the same fabrication procedure of the graphene ECoG electrode array were conformed to the custom supporting structure with a curvature. The electrode length is 15.7 mm. The electrode width is 100 µm. **(b)** Photograph of the measurement setup.

Bending testing was conducted by creating 9 straight, parallel graphene electrodes using the same ECoG stencil printing technique. To mimic various degrees of bending after implantation, the electrodes were placed on a flat surface and custom-built acrylic structures (**Fig. 2.5.3**) with radii

of curvature of 6 mm, 8 mm, 10 mm, 12 mm, and 14 mm, when their impedance was measured using the interface board (RHD2000, Intan Technologies Inc.) at 1000 Hz.

Surgical implantation: All animal experiments were approved by the University of Minnesota Intuitional Animal Care and Use Committee (IACUC). 9 C57BL/6 mice (5 males and 4 females) at the age of 12-30 weeks were used in this study. Initially, 5 mice were implanted with the graphene ECoG devices while optimizing the electrode layout and overall device design. Mice were housed in a 14hr light/10hr dark cycle in rooms maintained at 20-23 °C and 30-70% relative humidity. Mice had ad libitum access to food and water. Mice were given preemptive doses of 2mg/kg of sustained-release buprenorphine (Buprenorphine SR-LAB, ZooPharm) and 2 mg/kg of meloxicam for analgesia and preventing brain inflammation respectively. Mice were anesthetized 30-60 minutes after the initial analgesia dosage using 1-5% isoflurane anesthesia in Oxygen. Eye ointment (Puralube, Dechra Veterinary Products) was applied to the eyes. The scalp was shaved and cleaned. Once the mice were fixed in a stereotax (900LS, Kopf), the scalp was sterilized by repeatedly scrubbing Betadine and 70% Ethanol solution (3 times). Next, the scalp was removed using surgical scissors. The tissue and fat under the scalp were subsequently cleared using a micro curette (# 10080-05; Fine Science Tools). Partial temporalis muscle wrapping around the skull was carefully removed using a scalpel to expose the squamosal area. After drilling a ~ 300 μm-diameter hole on the squamosal suture, a stainless-steel bone screw (#FF000CE094, JI MORRIS Company) tied to a 26-gauge stainless-steel reference wire was tightened in the hole firmly. A large craniotomy was immediately performed using a high-speed dental drill following a rectangular path approximately 4 mm x 9 mm posterior to Bregma. After the drilling, the skull piece was removed from the dorsal cortex using two micro curettes holding its lateral edges. A gauze pad soaked in sterile saline was gently placed on the exposed brain to keep it moist.

The graphene ECoG device was sterilized by immersion in 70% Ethanol for 2 min and subsequently rinsed thoroughly with sterile saline. The periphery of the craniotomy was cleaned using a pointed cotton tip after removing the gauze pad. The window frame was gently placed on the exposed brain. Surgical adhesive (Vetbond, 3M) was applied around the edges of the window frame to bond the window frame to the skull. After the adhesive was cured, a customized waterjet-cut Titanium headplate was fastened on the implant with a #0-80 screw. The implant was cemented to the skull using opaque dental cement (Metabond, Parkell Inc.). Mice were transferred from the stereotax to a heated pad (catalog no. 72-0492; Harvard Apparatus) for recovery from the anesthesia and were transferred to a clean cage partially located on a warming pad once they were fully ambulatory. 2 mg/kg meloxicam was administrated twice per 24 hr for 72 hr post-surgery. Mice recovered for 7 days before any *in vivo* experiment.

In vivo electrophysiology: *In vivo* electrode performance test: The impedances of electrodes in the implanted devices were measured periodically (up to 182 days). Animals were transferred from their home cage and affixed under anesthesia in a custom head-fixation device adapted from previous studies [53], [105]. Subsequently, the FPC connector on the amplifier was connected to the PCB connector of the ECoG device. Impedance measurements were acquired at 1000 Hz.

Awake and anesthetized spontaneous recordings: Mice were head-fixed on the treadmill, and 4 minutes of spontaneous recordings were acquired when the animals were fully awake. All the signals were recorded through the RHD 2000 interface board at a sampling rate of 20 kHz. Mice were administrated a cocktail of Ketamine (100 mg/kg) and xylazine (10 mg/kg) while head-fixed.

A heated pad was placed under the animal to maintain body temperature, and mice were supplemented with Oxygen. Once the animal was fully unresponsive to toe pinch stimulus, multiple 4-minute-long spontaneous recordings were acquired. Once fully recovered from anesthesia, mice were removed from the head fixation apparatus and transferred back to their home cage.

ECoG recordings in response to sensory stimuli: Stimulation applied to mice whiskers is a common way to study the evoked response in the somatosensory system [106]. Here, we used a lateral air-puff stimulation to test whether the implanted ECoG array can successfully measure the contralateral evoked response [29], [52]. To do so, brief air-puff stimuli of compressed air flow were applied to the right whiskers of head-fix mice through a blunt 24-gauge stainless steel needle. The needle-guided the air puff to stimulate the whiskers in the posterior-anterior direction (**Fig. 4a**). 24-30 air-puff stimuli were given to each mouse in each experimental session, with each stimulus lasting 100 ms. The inter-stimulus interval was randomized (8 to 10s) and controlled using a microcontroller (Arduino Uno, Adafruit) actuated solenoid valve.

Data analysis:

All the data, including electrode impedances and ECoG signals, were collected and converted using the interface board's software (RHD2000 interface, Intan Technologies Inc.). The raw ECoG signals were first down-sampled to a moving average of 2 kHz and low-pass filtered using an elliptic filter with a passing band of 100 Hz. Custom scripts in MATLAB (MATLAB 2020b, Mathworks) were used to analyze and plot the data.

2.6 Summary

In this chapter, we introduce a fully desktop-fabricated flexible graphene ECoG array, allowing scientists of bio-background to design and build their own ECoG array using common bio-laboratory tools. For this ECoG, we synthesized a new highly conductive graphene ink exfoliated in a biocompatible organic solvent Cyrene. Current-voltage characteristic shows that the Cyrene graphene ink has better conductivity than graphene inks exfoliated in common organic solvents: DMF and C/T. Electrochemical characterization tests like CV, EIS, and accelerated corrosion tests showed that the graphene ECoG electrodes are functional and usable for chronic *in vivo* studies. Furthermore, the *in vivo* experiments of spontaneous recordings under different conditions and stimuli-evoked response recordings successfully demonstrated the usability of this graphene ECoG. Therefore, our graphene ECoG array is ready for broader applications in brain study.

Chapter 3:

3D printed transparent ECoG electrode arrays for simultaneous ECoG and Ca^{2+} imaging[1]

[1] The work reported in this chapter earned and has received support from the NIH NINDS Award (Number R42NS110165).

[2] The publication of this work is in preparation.

Abstract:

The ECoG devices in Chapter 2, provide high temporal resolution electrophysiology recording from small, distributed sites in the brain surface. To complement these capability, efforts have been made to combine ECoG with calcium imaging, which provides high spatial resolution information. To do so, several efforts have been made to develop transparent ECoG arrays that can be patterned on transparent substrate to realize functionalized, cranial window implants [29], [43]. In Chapter 3, to create the optical access to brain Ca2+ imaging, we developed a 3D printed transparent ECoG electrode array greatly simplifying the existing microfabrication procedure of transparent ECoG arrays. Our 3D-printed ECoG demonstrated its capability of chronic implantation for long-term electrophysiology and imaging. The ECoG electrodes were tested to have impedance lower than 300 kΩ with high optical transmission 83.89 ± 1.67 %. We conducted *in vivo* recording of stimuli-evoked brain activity and anesthesia drug induced brain activity in which strong correlations with a cross correlation factor > 75% between the electrical signals and optical signals were found. Thus, our ECoG can be deployed in brain studies involving Calcium activities and local field potential measurement.

3.1 Introduction

The graphene ECoG device presented in **Chapter 2** can provide high temporal resolution in brain signaling up to 100 Hz. However, it still lacks fine spatial resolution due to the limited number of electrodes (16) placed on the cortical surface. Furthermore, our previous work reported that Ca^{2+} imaging can provide high spatial resolution in neural recording [52], [53] by creating a large area of optical access to the brain. Thus, in **Chapter 3**, we engineered a 3D-printed transparent ECoG device that can be used for cortex-wide simultaneous ECoG and Ca^{2+} imaging. This technology allows us to study the correlations between the brain's Ca^{2+} signals and surface field potential and brings a higher spatial resolution than the graphene ECoG developed in **Chapter 3**.

3.2 Approach

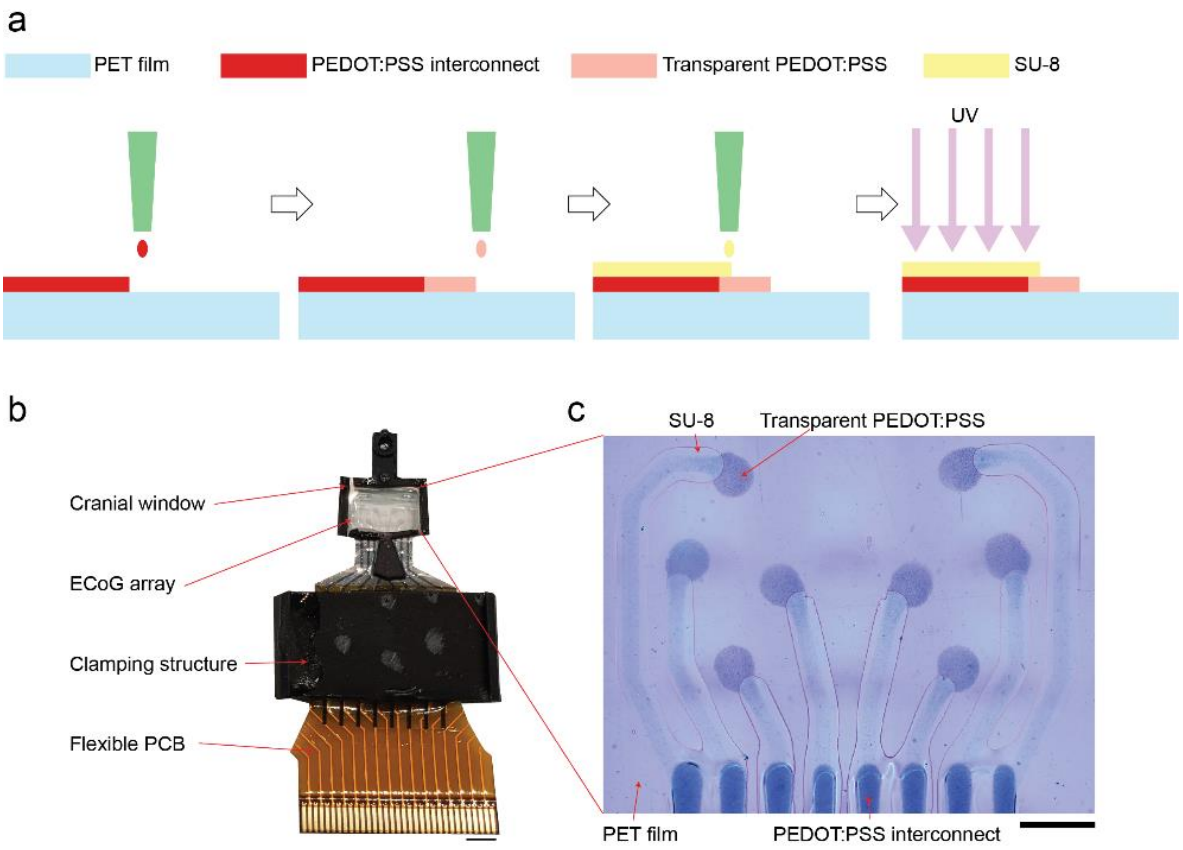

Figure 3.2.1 | 3D-printed transparent PEDOT:PSS/SU-8 ECoG array and implant device: (a) Fabrication flow chart of 3D printing the ECoG electrode: a high-concentration non-transparent PEDOT:PSS interconnect was first printed on the PET film; secondly, low-concentration transparent PEDOT:PSS ECoG electrode traces were printed on the PET film and connected with the interconnects; thirdly, a transparent insulation layer of SU-8 was printed on top of the interconnects and the partial ECoG electrode to expose electrode pads contacting brain surface. **(b)** Image of the whole ECoG device, which has a cranial window, a 3D-printed ECoG electrode array, a clamping structure, and a flexible PCB interface. **(c)** The microscope image of the transparent ECoG array (Scale bar is 500 μm)

To fabricate the 3D-printed transparent ECoG electrode array, generally, we used a ultra-high precision extrusion 3D printer [107]. Briefly, as shown in **Figure. 3.2.1a**, one layer of non-

transparent PEDOT:PSS interconnect was 3D printed on the transparent PET film; transparent PEDOT:PSS electrode array was 3D printed on the PET film and connected to the interconnect; upon the PEDOT:PSS electrodes and interconnects, a layer of SU-8 transparent negative photoresist was 3D printed and UV-cured on the electrode array to insulate the electrodes and interconnects. The overall architecture of the 3D printed ECoG device is similar to the Graphene ECoG device described in **Chapter 2**, which has 3D printed clamping structure to mechanically reinforced the 3D printed PEDOT:PSS electrode array bonded with a flexible PCB (**Fig. 3.2.1b**). As shown in **Figure 3.2.1c**, the electrode array has 8 transparent electrode pads contacting with brain surface, and the rest of electrode traces and interconnects are precisely encapsulated by the SU-8 traces.

3.3 Results

Characterization test of optical transmission

ECoG electrode arrays measure surface voltage potentials to study brain activity [60]. Electrodes with higher conductivity will have better recording performance [108]. The impedance of functional ECoG electrodes is expected to be less than 1 MΩ [86], [87], [109]. The ECoG devices were submerged in 1X phosphate-buffered saline to mimic the physiological environment and measured their impedances using an Intan RHD2000 recording station. We built and tested five devices. For all five devices, 38 out of 40 electrodes had impedance values less than 1 MΩ. Thus, the electrode fabrication procedure was stable.

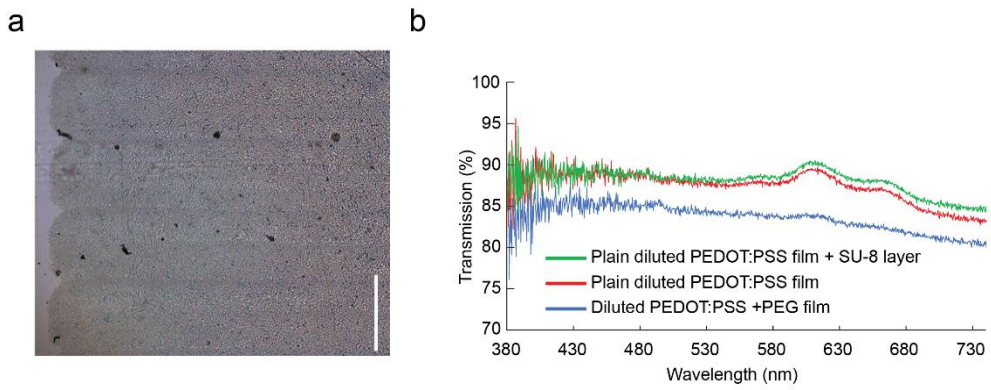

Figure 3.3.1 | Thin-film optical transmission: **(a)** 3D printed thin film of diluted PEDOT:PSS + Polyethylene Glycol (PEG) additive, line spacing 0.23 mm (Scale bar is 500 µm). **(b)** The light transmission rates in % through thin films of different materials

For Ca^{2+} imaging on mice, the ECoG electrode's light transmission rate needs at least 70%, as reported in our previous work [53]. To evaluate the electrode transparency, we measured the light transmission rate through material samples using a light source of variable wavelength ranging from 380 nm to 730 nm. An optical fiber directed the light through the samples into a spectrometer. Spectrometer readings from unobstructed light determined the percentage of light passing through the material samples. The electrode material samples tested were cut out of a solid film of diluted PEDOT:PSS with PEG additive. The films were printed with the same parameters used for the ECoG electrodes but were rectangular. (**Fig. 3.2.2 a**). The diluted PEDOT:PSS with PEG with an average transmission of 83.89% and a standard deviation of 1.67% over wavelengths between 380 and 740 nm (**Fig. 3.2.2 b**). Plain diluted PEDOT:PSS (without PEG) and plain diluted PEDOT:PSS (without PEG) covered with a layer of SU-8 were also measured for comparison; both had slightly higher levels of light transmission, but PEG was

still used in the devices due to its positive effect on reducing electrode impedance. The addition of SU-8 had no noticeable effect on transmission, indicating its transparency.

Implantation of the ECoG array

Since the PEDOT:PSS ECoG electrode array showed its low impedance and high transparency, the ECoG device was tested in *in vivo* experiments to evaluate its performance. To test whether the ECoG electrode array is safe for the animal, five devices will be separately implanted in mice in accordance with protocols approved by the University of Minnesota Intuitional Animal Care and Use Committee (IACUC); the goal is to achieve at least 75% survival rate of chronically implanted mice for at least two weeks post-surgery when optical microscope imaging will be used to monitor the brain conditions like dura thickening or immune response. The impedance of implanted ECoG devices will also be measured to test whether the electrode lasts in *in vivo* environments. To evaluate the device's ECoG recording performance, stimuli evoked brain response will be recorded with the same experiment design as **Aim 1**. Next, simultaneous ECoG recording and Ca^{2+} imaging will be acquired when the animal is fully awake vs. anesthetized to test whether a difference in brain activity can be found in electrical and Ca^{2+} signals. At the same time, the correlation between the electrical and Ca^{2+} signals will be evaluated.

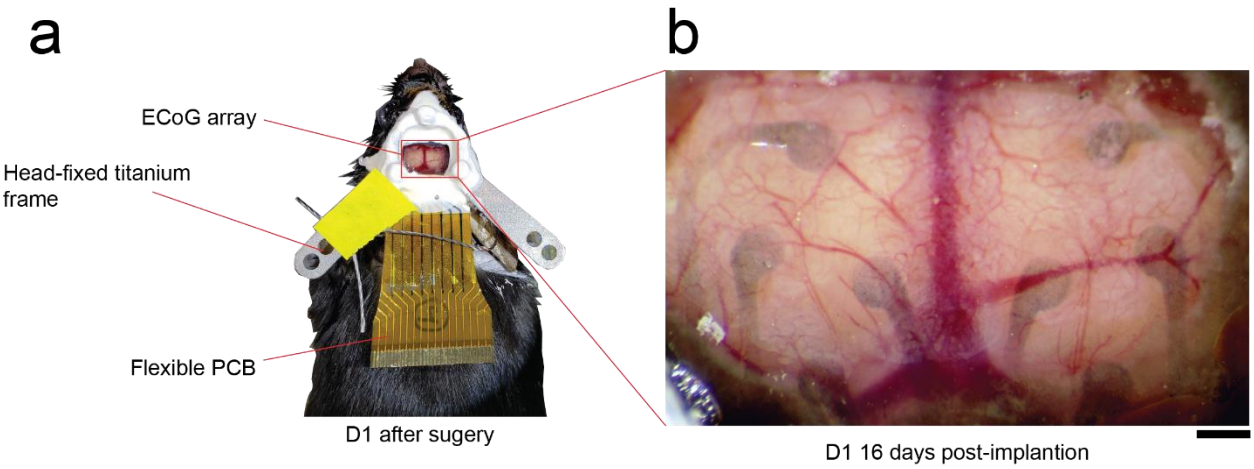

Figure 3.3.2 | Chronic implantation of 3D printed devices: (a) The image of the whole implant (D1) includes the ECoG array under a See-shell, a head-fix titanium frame, and a flexible printed circuit board (PCB) on the mouse. **(b)** D1 ECoG on the brain after 16 days of implantation.

The devices were implanted on five mice: D1 and D3 were implanted on two 5-month-old wild-type mice (D1 is male, D3 is female); D2, D4, and D5 were implanted on three 6-month-old C56/BL6 mice (D2 is male, D4 is female, D5 is male). All animal procedures were approved by the Institutional Animal Care and Use Committee (IACUC) at the University of Minnesota, Twin Cities. All mice recovered fully and exhibited no loss of body condition or change in behavior throughout implantation. Furthermore, other than bone regrowth, no visible injuries for all five devices under the microscope can be found for at least two weeks of implantation (**Fig 4.2.3 b**). Therefore, our device is safe to be used for further ECoG recording.

Table 3: Impedance measurements of implanted ECoG devices post-implantation.

Electrode	D2 (28 days)	D3 (14 days)	D4 (14 days)	D5 (14 days)
1	86.4 kΩ	86.2 kΩ	70.2 kΩ	62.7 kΩ
2	84.3 kΩ	10.2 MΩ	55.1 kΩ	26.1 kΩ
3	57.8 kΩ	62.7 kΩ	19.2 kΩ	16.2 kΩ
4	66.2 kΩ	88.6 kΩ	71.4 kΩ	17.6 kΩ
5	69.7 kΩ	25.8 kΩ	323 kΩ	18.2 kΩ
6	67.9 kΩ	50.4 kΩ	1.79 MΩ	14.7 kΩ
7	88.5 kΩ	51.1 kΩ	3.25 MΩ	17.8 kΩ
8	148 kΩ	37.7 kΩ	149 kΩ	93.4 kΩ

Implanted ECoG electrode array in the *in vivo* environment is expected to experience material loss and tissue encapsulation around the electrodes, which leads to high impedance and downgrading ECoG signal quality [36]. In all five implanted devices, except for D1, whose PCB connector was accidentally broken and failed to take any measurements, D2, D3, D4, and D5 had 37 functional electrodes out of 40, with impedance values less than 1 MΩ after two weeks of implantation (**Table 3**). All five mice survived the implantation.

Simultaneous ECoG recording and Ca^{2+} imaging of airpuff stimuli evoked brain activity in head-fixed mice

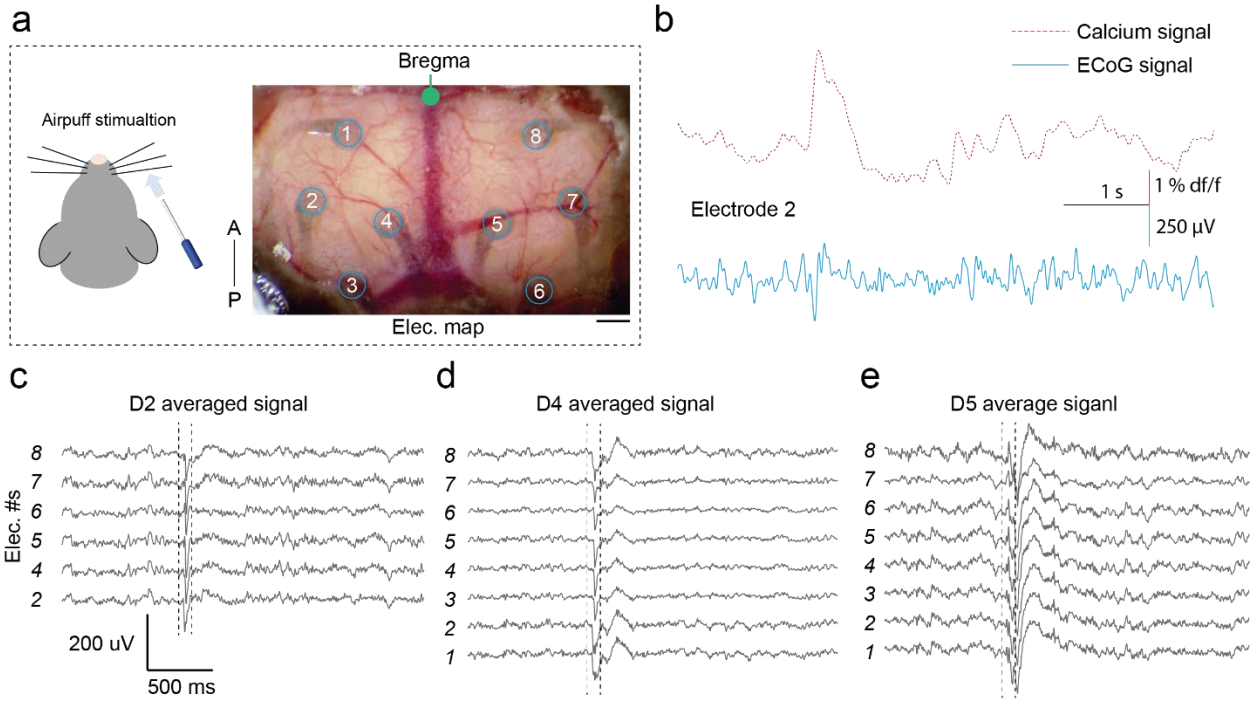

Figure 3.3.3 | Functional use of ECoG arrays to measure stimulus-evoked responses: (a) Stimulation experiment setup to deliver brief air-puff to whiskers and the map of implanted ECoG electrodes on the brain. The green dot marks the location of Bregma point. **(b)** Normalized Calcium fluorescence changes (dashed line) vs. ECoG signal (solid line) at electrodes 2 D5. **(c), (d), (e)** Averaged recorded brain signals of D2, D4, and D5 activated by the air-puff stimulation.

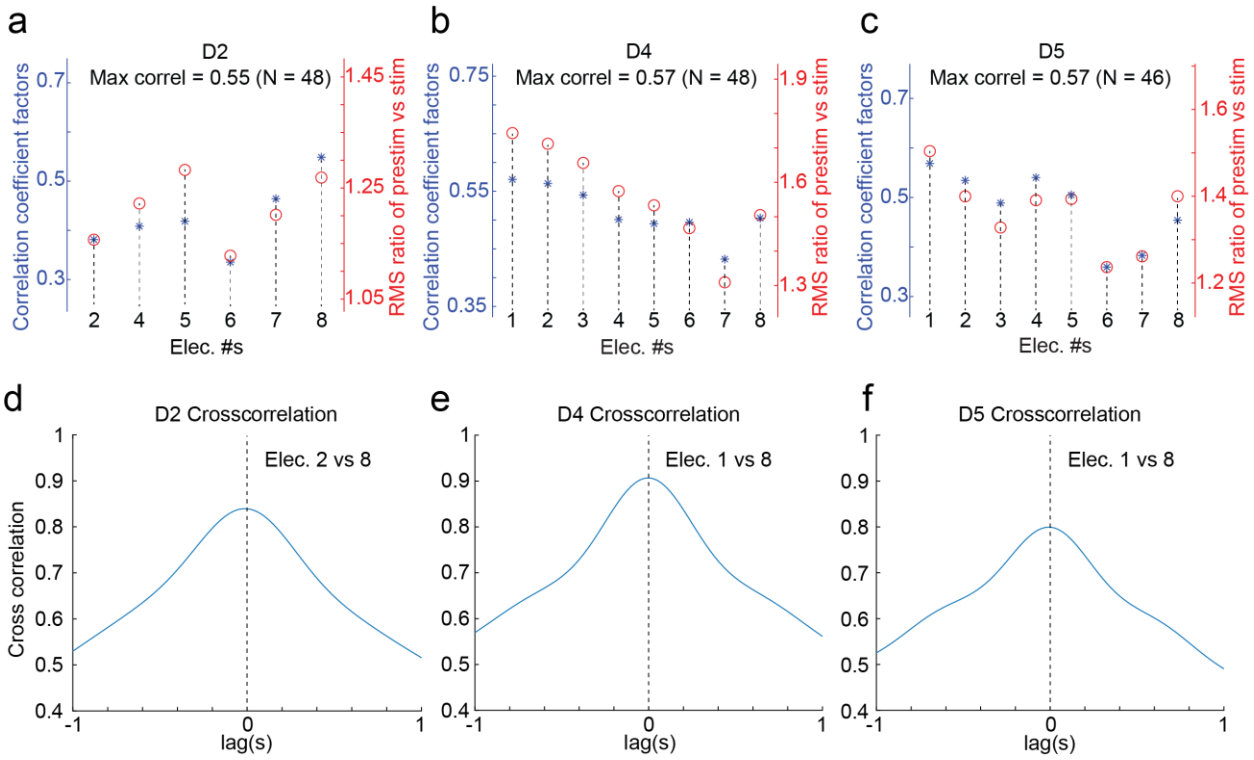

Figure 3.3.4 | Correlations between ECoG and Calcium Signals: a, b, c. Correlation factors of airpuff stimulation vs. brain's neuronal response captured by each electrode, and the ratio of the root mean square (RMS) of neuronal responses in the periods of pre-stimulation vs. post-stimulation of D2, D4, and D5. d. The cross-correlation between the brain signals recorded by electrodes 2 and 8 in D2. e, f. Cross-correlation between the brain signal recorded by electrodes 1 and 8 in D4 and D5.

For testing whether the ECoG electrode array can localize brain activity responding to lateral stimulation, the mouse's right whiskers were given 23-28 air-puff stimuli each lasting ~100 ms for 4 minutes (**Fig. 3.3.3 a**). To eliminate the noise, we averaged the signal across all 23–28 time windows (2.5 s) containing the air-puff and filtered it with a low-pass filter (0-100 Hz) to generate an averaged signal plot showing that all functional electrodes captured the evoked brain activity responding to the air-puff (**Fig. 3.3.3 c, d, and e**). In devices D4 and D5, compared with electrode 8 in the lateral somatosensory cortex, we found that electrode 1 in the contralateral somatosensory cortex had higher signal amplitude. To further quantify such difference, we first

calculate the root mean square (RMS) power of the ECoG signal evoked by the stimuli vs. at pre-stimulus state (no stimulus was given to the animal), then plot the average ratio of the RMS values individually for each electrode in each device. Since D2 lost the contralateral electrode 1 in the somatosensory cortex (**Fig. 3.3.3 c**), we compare the RMS signal ratio obtained by D4 and D5 and find that the contralateral electrode 1 did have a higher signal response than lateral electrode 8 in the sensory cortex (**Fig. 3.3.4 b and c)**.

Furthermore, we also calculate the correlation between the individual electrode's RMS ratio to the existence of stimuli (in the control group, the air-puff stimuli were turned off in some time windows). The ECoG signals and Calcium signals are generally highly correlated with each other with a cross-correlation factor higher than 0.75 (**Fig. 3.3.4 d, e, and f**). We found that the contralateral electrode 1 in both D4 and D5 have higher correlation values than the lateral electrode 8 (**Fig. 3.3.3 d and e)**. This finding indicates a similar localized brain response found in **Chapter 2**. Furthermore, the ECoG and Ca^{2+} signals were correlated in the overall recording (**Fig. 3.3.4 a, b and c**).

Simultaneous ECoG recording and Ca^{2+} imaging of brain activity in mice under Ketamine anesthesia

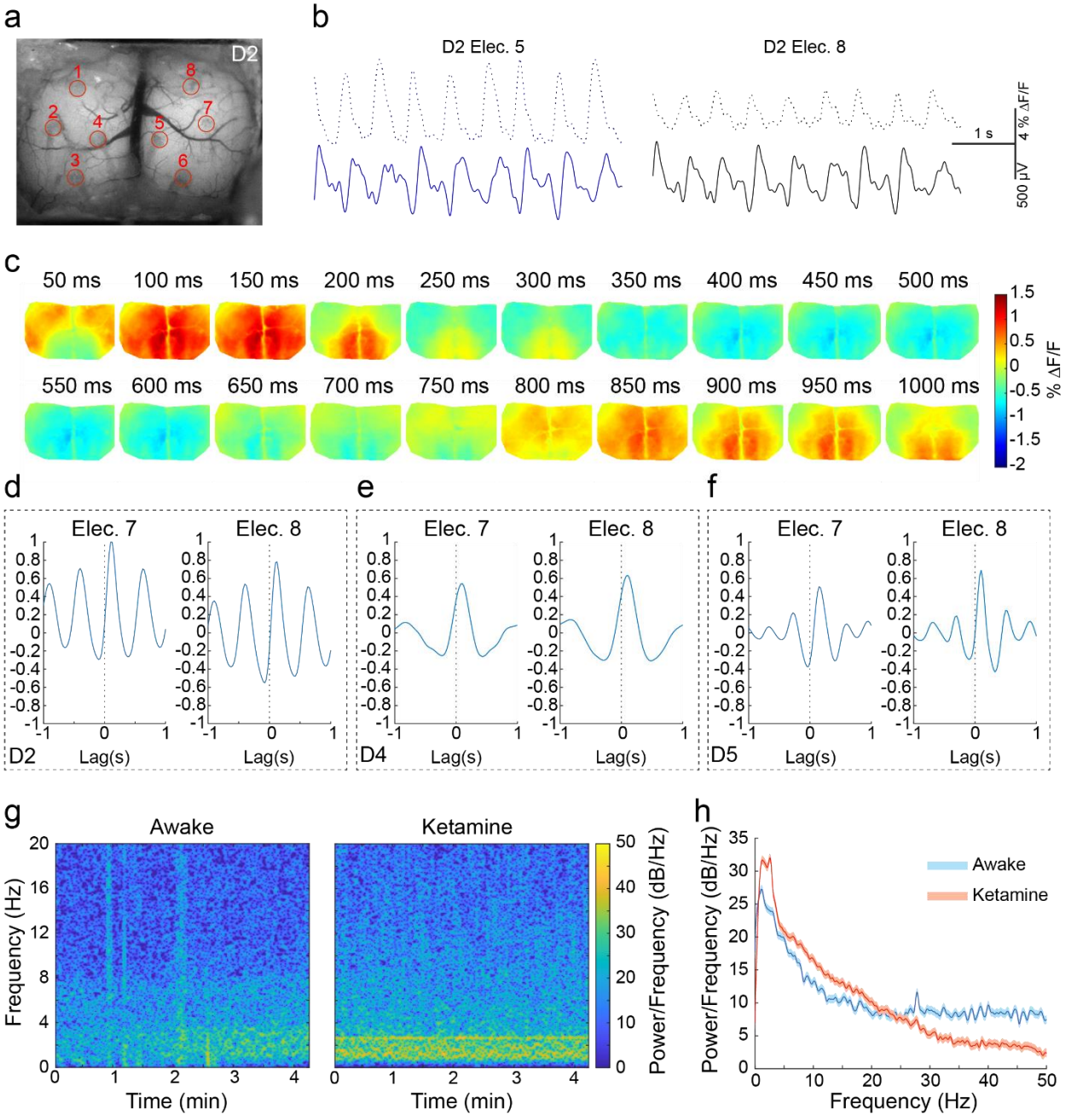

Figure 3.3.5 | Simultaneous electrophysiology and Ca^{2+} imagined in Thy1-GCaMP6f mice: **(a)** Map of implanted ECoG electrodes in transgenic animal broadly expressing GCaMP in excitatory cells in the cortex. **(b)** Normalized Calcium fluorescence changes (dashed line) vs. ECoG signal (solid line) at electrodes 5 and 8 in D2. **(c)**

Mesoscale calcium imaging under Ketamine anesthesia in D2 shows traveling waves of periodic activity from anterior to posterior regions of the cortex. **(d), (e), (f)** Cross-correlation between calcium signal and ECoG signal under Ketamine anesthesia in D2, D4, and D5. g. Spectrograms of ECoG signals in awake state vs. anesthetized state for D2. **(g)** Spectrogram of ECoG signals measured at electrode 5 in awake state vs. anesthetized state for D2. **(h)** Power spectrum of ECoG signals measured at electrode 5 in awake state vs. anesthetized state for D2.

We perform Ca^{2+} imaging through our transparent ECoG device using an epifluorescence microscope on transgenic Thy1-GCamP6f mice broadly expressing calcium indicators in excitatory neurons of the cortex (**Fig. 3.3.5. a**). Mesoscale imaging reveals traveling waves of Calcium activity going anterior regions of the cortex to the posterior regions. No loss of signal quality was observed under the electrode pads (**Fig. 3.3.5. c**) because no shadow of the electrode was found. Under Ketamine anesthesia, the ECoG signals recorded by our device and calcium activity were marked by low-frequency oscillations (0-4 Hz) (**Fig. 3.3.5. b**). These Ketamine-induced low-frequency oscillations can also be found in the spectrogram (**Fig. 3.3.5. g**) and power spectrum (**Fig. 3.3.5. h**). As shown in **Figure 3.3.5 d, e,** and **f,** Ca^{2+} signals and ECoG signals are highly correlated with an approximate 100-ms delay. Therefore, in **Chapter 3**, we successfully developed a 3D-printed transparent ECoG device that can perform Ca^{2+} imaging and ECoG recording simultaneously with an improved spatial resolution brought by Ca^{2+} signal compared to the traditional graphene ECoG device in **Chapter 2**.

3.4 Methods

Electrode printing and implant fabrication

To fabricate this 3D-printed transparent ECoG electrode array, as shown in **Figure. 3.2.1 a**, they were created via a 3-step fabrication process, with each step using the same 3D printer (ANT130 nano-positioning system). The electrode material is mainly PEDOT:PSS, a flexible and biocompatible conductive polymer [39]. Previously, 3D-printed ECoG devices with silver electrodes were opaque and cytotoxic [44]. To prepare for device fabrication, a small rectangle of polyethylene terephthalate (PET) film was set flat on the printer stage. As shown in **Figure 3.2.1 a**, a 5.0 wt% PEDOT:PSS ink was used to print non-transparent electrode interconnects on the PET film to route the ECoG electrodes and flexible PCB interface. The PET file with the printed interconnects was then placed on a 120 °C hot plate for 5 minutes to cure the PEDOT:PSS; a diluted PEDOT:PSS ink mixed with polyethylene glycol (PEG) [110]–[112] was used to print transparent electrodes each linked with one of the interconnects, and the device was again placed on a 120 °C hot plate for 5 minutes to cure the ink; finally, an insulation layer of SU-8 2.0 was printed over most of the transparent electrodes, leaving the ends exposed to be electrode pads contacting the brain. We previously used a polymethyl methacrylate (PMMA) layer for insulation, but that material became cloudy and formed cracks *in vivo*. Therefore, SU-8 was chosen as an alternative transparent and biocompatible insulator [93]. The insulation layer went through a curing process that consisted of baking on a hot plate at 65 °C for 1 minute, 95 °C for 3 minutes, 380 nm UV exposure for 100 seconds, a second baking step of 1 minute at 65 °C and 1 minute at 95 °C, and finally a hard bake at 120 °C for 15 minutes to ensure durability over time. This resulted in a durable, flexible, and transparent ECoG device with eight electrode channels (**Fig. 3.2.1 c**). The ECoG electrode array was mounted on a modified See-

Shell frame from the previous study [53] and bonded with a flexible PCB connector connected to the recording station for further measurement (**Fig. 3.2.1 b**).

Implantation:

The implantations follow the same procedure in **Chapter 2**. There are five mice are GCaMP5f C56/BL6 mice.

Simultaneous ECoG recording and Ca^{2+} imaging of airpuff stimuli evoked brain activity in head-fixed mice:

The experiment follows the same procedure in **Chapter 2**.

Simultaneous ECoG recording and Ca^{2+} imaging of brain activity in mice under Ketamine anesthesia:

The experiment follows the same procedure in **Chapter 2**.

3.5 Summary

In this Chapter, we developed a 3D-printed transparent PEDOT:PSS ECoG electrode array, which can be chronically implanted. Our transparent ECoG array successfully demonstrated simultaneous ECoG recording and Calcium imaging of stimuli-evoked and Ketamine-induced

brain activities in head-fixed mice, where strong correlations were found between the brain's Calcium and electrical signals.

Chapter 4:

Miniaturized micro-camera array microscopy (mini-MCAM) for cortex-wide Calcium imaging at single-cell resolution in head-fixed or freely behaving mouse[1]

[1] The work reported in this chapter is supported by NIH Grant (Number RF1NS113287)

[2] The publication of this work is in preparation.

Abstract:

Recording the activities of individual neurons distributed across multiple brain regions can provide new insights into the brain's functions and animal behavior. Over the last few years, miniaturized devices have been developed to image the activities of neurons in small fields of view in freely behaving animals. Scaling the devices to image large fields of view results in large imaging objectives and large cameras that are difficult to miniaturize for studying freely behaving animals. Furthermore, such imaging devices must contend with the brain's complex three-dimensional surface. Here, we introduced two innovations to enable calcium imaging from multiple sites at cellular resolution across the dorsal cortical surface. First, we engineered a multi-planar transparent skull implant with four glass windows stacking to open up 42 mm^2 of the dorsal cortical surface for imaging. This area encompasses most of the bilateral primary and secondary motor cortices, much of the somatosensory cortex areas, the Retrosplenial, association, higher visual, and part of the primary visual cortex. We next built an array of fluorescent micro-cameras to image each of the four planes defined by the square window. The

fluorescent micro-camera consists of a 1:1.4 relay objective lens, a fluorescent imaging filter, and a miniaturized CMOS sensor. Each micro-camera can image 8-12 mm^2 FOV at resolutions ranging from 9.9 to 11.4 μm. A laser-coupled fiber-based illumination system delivers 460 nm excitation light with a light intensity power of 4.2-6.7 mW to each targeted brain region. We imaged neuronal activity using the micro-camera in head-fixed and freely behaving Ai163 x Cux2-creERT2 transgenic mice that sparsely expressed GCaMP6s in layers 2-3 pyramidal neurons in the cortex.

4.1. Introduction:

Chapter 1 introduces the concept of the ideal neural activity sensing device, which should be highly accessible and record cortex-wide brain activity at single-cell resolution in freely behaving animals. To approach this ideal neural activity sensing device, 2 devices were developed to improve one or more aspects of existing neural activity sensing devices: First, the fully-desktop fabricated ECoG array, built by off-shelf materials and common bio-laboratory tools, in **Chapter 2**, provides high accessibility but lack spatial resolution. Next, the 3D-printed transparent ECoG array, combined ECoG and Calcium imaging techniques, in **Chapter 3,** provides higher temporospatial resolution but cannot measure the single neuron's activity. In **Chapter 4**, inspired by the promising *in vivo* imaging results given by the Calcium imaging technique in **Chapter 3**, the direction was chosen to develop a Calcium imaging device approaching the ideal neural activity sensing features.

Calcium imaging technologies	Resolution	Field of View	Acqusition speed	Weight/animal state
a 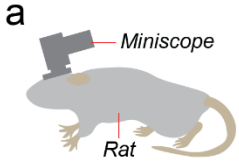 Miniscope-LFOV Guo et al., 2021	2.5 - 4.4 μm	3.1 × 2.3 mm	11 FPS	14 g Freely behaving rat
	4.4 - 6.2 μm	3.1 × 2.3 mm	23 FPS	14 g Freely behaving rat
	6.2 - 7.8 μm	3.6 × 2.7 mm	23 FPS	14 g Freely behaving rat
b 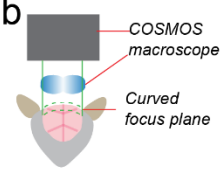 COSMOS system Kauvar et al., 2020	28 μm	10 mm × 10 mm	29.4 FPS	Head-fixed mouse
c 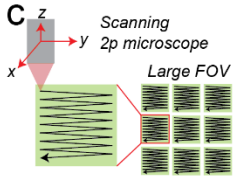 2p-RAM Sofroniew et al., 2016	Lateral 0.66 μm Axial 4.09 μm	4.4 × 4.2 mm	1.9 FPS	Head-fixed mouse
d 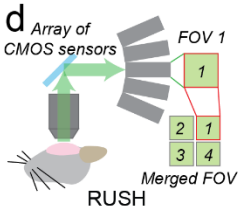 RUSH Fan et al., 2019	1.2 μm	10 × 12 mm	30 FPS	Head-fixed mouse
e 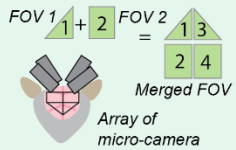 Miniaturalized MCAM	9.9 μm	4.5 × 2.5 mm × 4	30 FPS	Head-fixed or Freely behaving mouse

Figure 4.1.1 | Existing Calcium imaging device of cellular or near-cell resolutions: (a) A large FOV, single-cell resolution miniature microscope (Miniscope-LFOV) performs brain imaging in freely behaving mice. Miniscope-LFOV has a large FOV of 3.6 × 2.7 mm, a resolution of 6.2 – 7.8 μm, and a sampling rate of 23 Hz. **(b)** cortical observation by synchronous multifocal optical sampling method (COSMOS) to measure the brain activity across a large, curved brain region of 10 × 10 mm, at near cellular resolution of 28 μm, with a sampling rate of 29.4 Hz in head-fixed mouse. **(c)** Two-photon mesoscope (2p-RAM) can scan a large brain region of 4.4 × 4.2 mm at

resolutions of lateral 0.66 μm and axial 4.09 μm, with a relatively low sampling rate of 1.9 Hz in head-fixed mice. **(d)** Real-time, ultra-large-scale, high-resolution (RUSH) imaging system which can perform brain Calcium imaging in an ultra-large FOV of 10 × 12 mm, at a uniform resolution of ~1.2 μm, with a high sampling rate of 30 Hz in head-fixed mice. **(e)** Miniaturized micro-camera array microscope (mini-MCAM) developed in this study can measure brain activity, in a computational stitched FOV of 4.5 × 2.5 mm × 4, at a resolution of 9.9 μm, with a sampling rate of 30 Hz in both head-fixed and freely moving animal study.

In recent years, several Calcium imaging devices were developed to image brain activity at single-cell resolution or near-cell resolution:

In 2016, a team from Howard Hughes Medical Institute (Virginia, United States) developed a two-photon mesoscope (2p-RAM) to perform *in vivo* brain imaging at a subcellular resolution [113] (**Fig. 4.1.1c**). The 2p-RAM can scan a large brain region of 4.4 × 4.2 mm at a high resolution of lateral 0.66 μm and axial 4.09 μm but at a relatively low sampling rate of 1.9 Hz in head-fixed mice. In 2p-RAM's FOV of 4.4 × 4.2 mm, its high spatial resolution allows measuring the simultaneous activities of over 3000 neurons, but 2p-RAM's scanning working principle has a relatively low spatial resolution and only be used in headfixed mice.

In 2019, a team from Tsinghua University (Beijing, China) developed a real-time, ultra-large-scale, high-resolution (RUSH) imaging system to image the brain activity in a FOV of 10 × 12 mm at a uniform resolution of ~1.2 μm and a sampling rate of 30 Hz in head-fixed mice [114] (**Fig. 4.1.1d)**. The RUSH system uses a 34-camera array to record the neural activities from multiple brain regions and merge the cameras' FOVs into a large FOV containing the whole

cortex. The RUSH system uses the camera array to create a curved focal plane matching the curved brain surface, making the whole cortex imaginable. However, the RUSH system's camera array is costly and heavy for only use in headfixed mice.

In 2020, a team from Stanford University (California, United States) developed an imaging method of cortical observation by synchronous multifocal optical sampling (COSMOS) to measure brain activity across a large, curved brain region of 10 × 10 mm at near cellular resolution of 28 μm, and at a high sampling rate of 29.4 Hz in head-fixed mouse [115] (**Fig. 4.1.1b)**. Unlike the RUSH system's camera array using a camera array to create a curved focal plane, the COSMOS method uses a custom-built lens with multi-focal planes matching the curved brain surface to achieve a large FOV. Though this multi-focal lens has a much-minimized hardware setup than RUSH, its resolution of 28 μm may not be able to image all the cortical neurons with a soma size of 10-20 μm. As well as RUSH, COSMOS can only be used in head-fixed mice.

In 2021, a team from the University of California in Los Angeles (California, United States) developed a large FOV, single-cell resolution miniature microscope (Miniscope-LFOV) which can perform *in vivo* Calcium imaging in freely-behaving rat in a large FOV of 3.6 × 2.7 mm, at a high resolution of 6.2 – 7.8 μm, and a sampling rate of 23 Hz [116] (**Fig. 4.1.1a**). Miniscope-LFOV is a miniaturized 1p-microscope mounted on the freely-behaving rat, and it captures neurons' activities across its large FOV. However, the FOV is too small to image the neural

activity across the whole cortex. Also, its 14 g is too heavy for the freely-behaving mouse to carry [52], the most common animal model in the research.

4.2 Approach

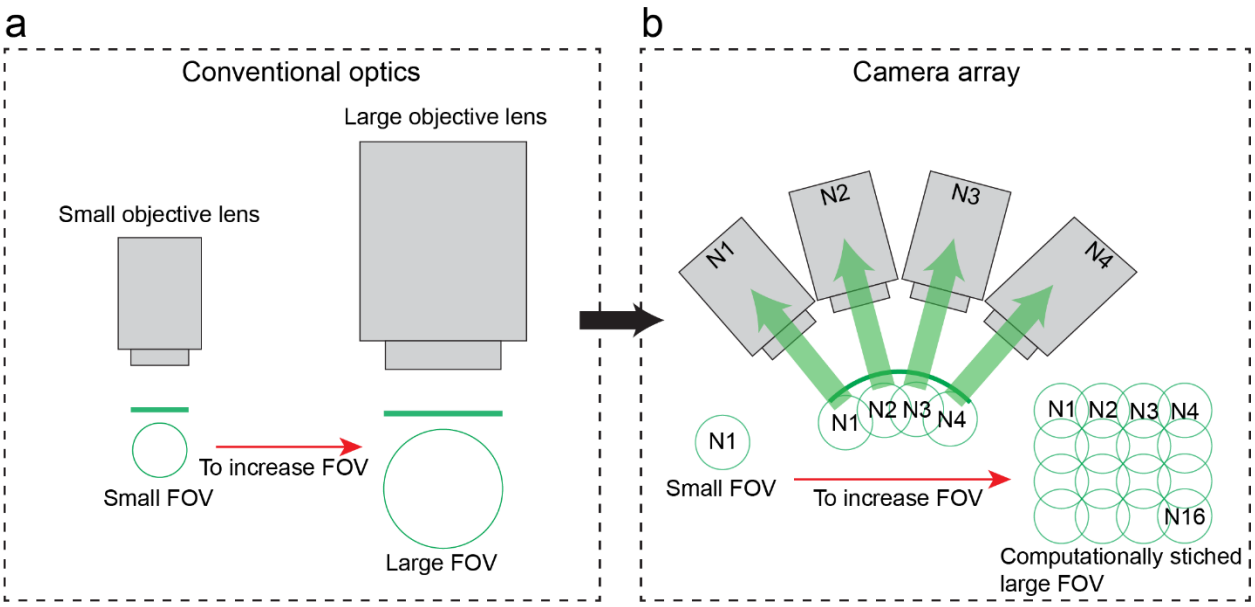

Figure 4.2.1 | Two approaches to increase FOV: (a) The approach of building conventional optics is to use a larger objective lens, which also results in a bulky, heavy device requiring head-fixing the animal during recording. **(b)** The other approach uses a miniaturized microcamera array to image and stitch multiple small FOVs to form a large FOV.

As mentioned, the ideal neural activity sensing device should record the neural activity across the dorsal cortex, requiring the imaging device to have a large FOV. One approach commonly used in conventional optics is using a large objective lens to achieve a larger FOV. This results in bulky, heavy hardware requiring head-fixing the mouse during recording (**Fig. 4.2.1a**). Here, this study proposes another approach to use a miniaturized microcamera array microscopy (mini-

MCAM), which has multiple microcameras to image different brain regions and merge all the microcameras' FOVs into a large FOV. Thus the mini-MCAM can create an approximate curved focal plane matching the curved brain surface (**Fig. 4.2.1b**).

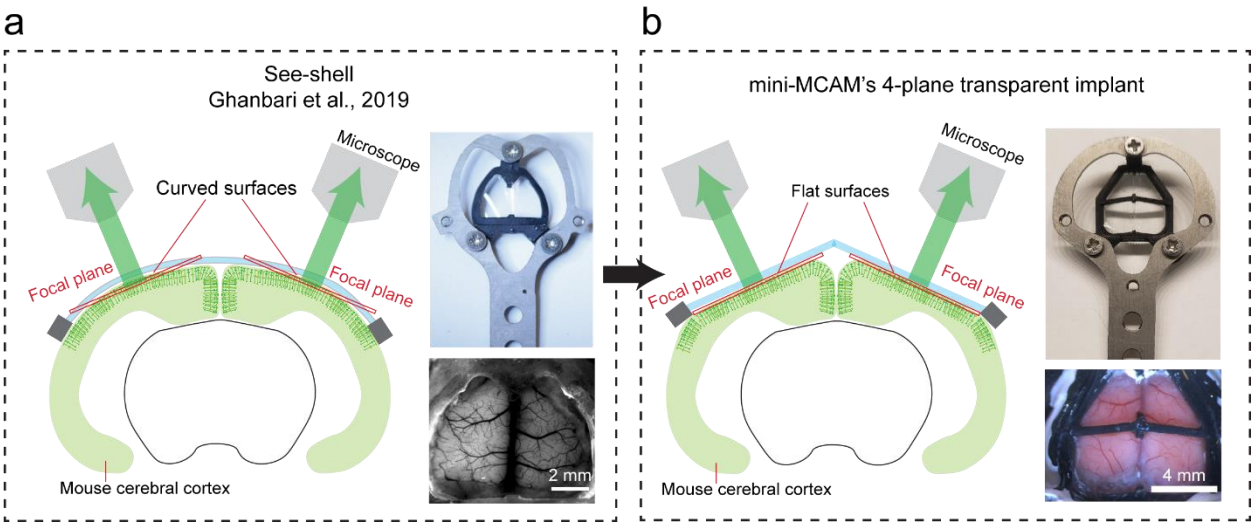

Figure 4.2.2 | See-Shell vs. 4-plane transparent skull implant: (a) See-Shell from our previous study is a transparent skull implant, which creates optical access to the brain through its curved transparent PET film placed on the brain surface. The curved surface challenges the imaging device to keep the whole FOV in focus if the focal plane is approximately flat. **(b)** Used by the mini-MCAM, a 4-plane transparent implant was developed to have four windows. Each window confronts the underneath brain surface to a flat surface allowing the microcamera to keep its whole FOV in focus easier.

The COSMOS system, 2p-RAM, and RUSH system were all trying to address one challenge: keeping the targeted curved brain surface in focus [114]–[116]. As shown in **Figure 4.2.2a**, for imaging the brain, when the optical access maintains the curved brain surface using curved transparent skull implants like See-Shell [53], if the center of the FOV is in focus, the edge of the FOV becomes out of focus, which results in failure of imaging the neural activity across the

whole FOV. Since the mini-MCAM has 4 microcamera to target 4 different brain regions, a 4-plane transparent skull implant of 4 windows was developed. Each window conforms the underneath brain tissue to a planar surface allowing one microcamera to keep its whole FOV in focus (**Figure 4.2.2b**).

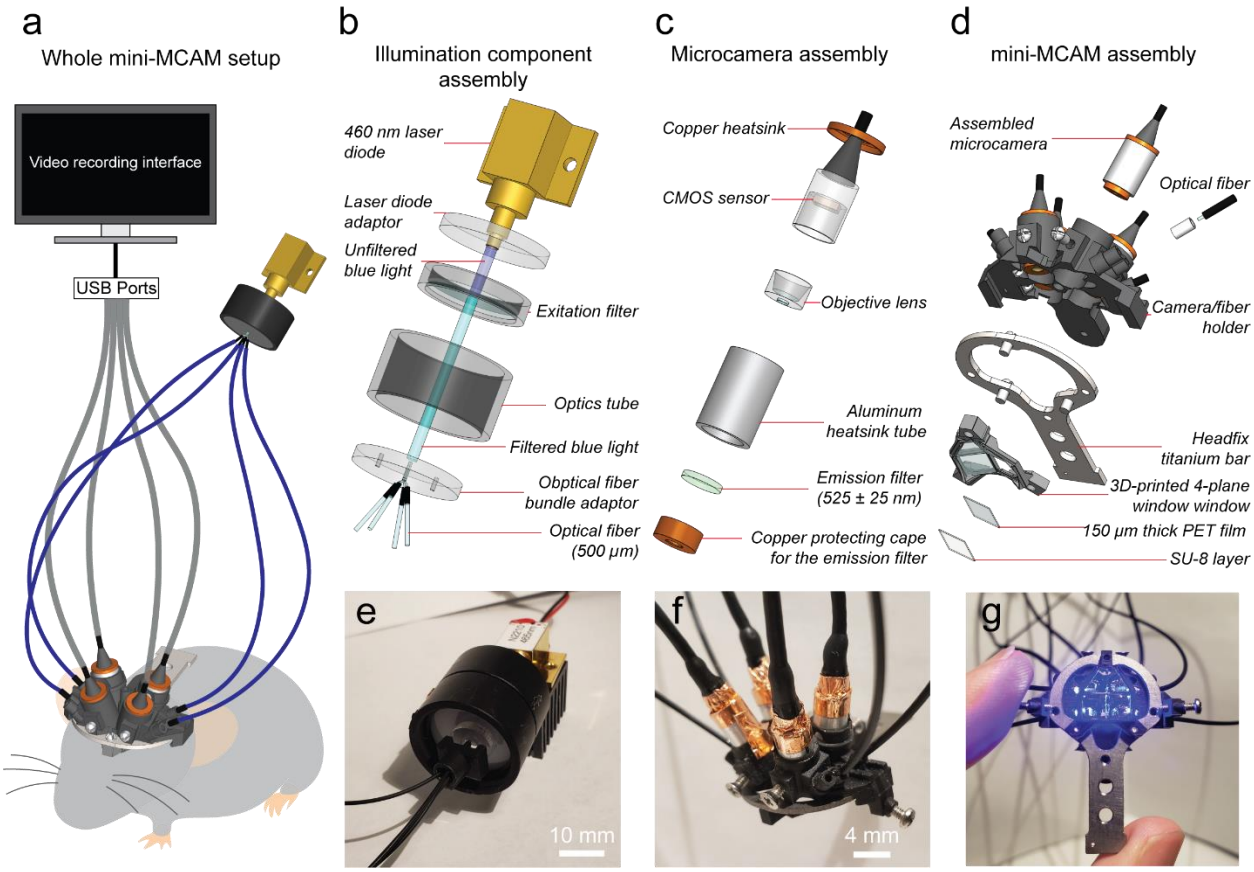

Figure 4.2.3 | Assembly and photos of mini-MCAM: (a) Demonstration of mini-MCAM mounted on a mouse for brain imaging. Mini-MCAM consists of an illumination component, laser-coupled fibers providing excitation light, an imaging component, a microcamera array performing cortex-wide brain imaging, and a recording interface visualizing and storing the imaging data. **(b)** Assembly of the illumination component: the excitation light is provided by a 460 nm laser diode. The blue light is first filtered by an excitation filter and then delivered to the brain surface through four optical fibers. **(c)** The microcamera is a modified endoscope consisting of a CMOS sensor, an objective lens, and an emission filter. The microcamera is mechanically reinforced by a heatsink Aluminum tube

and multiple copper components. **(d)** Assembly of mini-MCAM: four microcameras and four optical fibers are installed on a 3D-printed holding structure. The 4-plane transparent skull implant has four separate windows, mainly transparent PET films coated with a layer of transparent SU-8 negative photoresist for hardening the window. **(e)** Photo of the illumination component. **(f)** Photo of the microcamera array. **(g)** Photo of excitation blue light projected on the 4-plane window implant.

Based on the two introduced working concepts to increase the FOV in this study (**Fig. 4.2.1** and **Fig. 4.2.2)**, Mini-MCAM was developed to perform cortex-wide brain imaging at single-cell resolution in head-fixed or freely behaving mice. The mini-MCAM consists of three major components: an illumination component, an imaging component, and the 4-plane transparent skull implant. The illumination component provides 460 nm excitation laser light. The laser diode's light is first filtered by an excitation filter of 469 ± 17.5 nm and then delivered through a bundle of optical fibers to the brain under the transparent implant (**Fig. 4.2.3b**, **e,** and **g**). The imaging component is an array of four microcameras (**Fig. 3.2.3f**). Each microcamera is a modified endoscope with an emission filter of 525 ± 25 nm, an objective lens, and a CMOS sensor collecting the fluorescence signals from the brain's Calcium activity (**Fig. 4.2.3c**). The 4-plane transparent skull implant has four windows. Each window is a 150 μm thick PET film coated with a layer of transparent negative photoresist SU-8 (~20 μm), and the SU-8 demonstrated strong biocompatibility in **Chapter 3**. Four windows are installed on a 3D-printed PMMA window frame attached to a titanium structure for head fixation (**Fig. 4.2.3. d**). When imaging the brain, the microcamera array is installed on the titanium structure (**Fig. 4.2.3. a**).

4.3. Results

Benchtop testing of the mini-MCAM

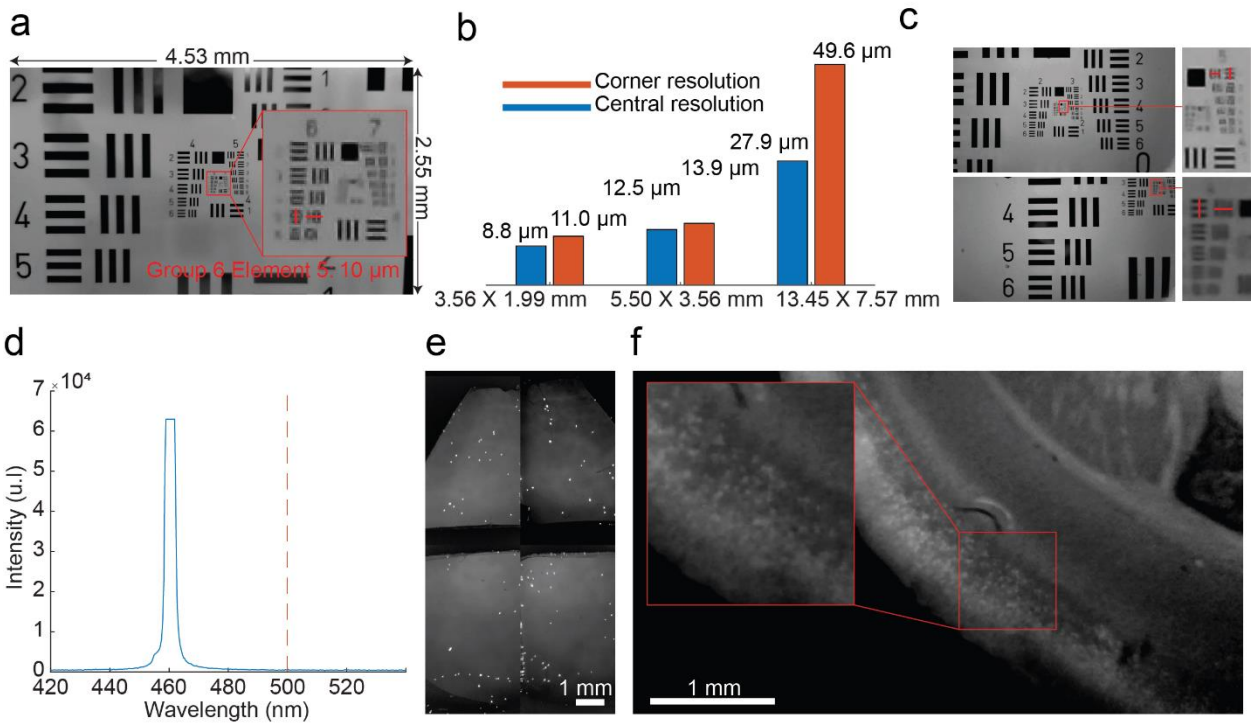

Figure 4.3.1 | Benchtop testing: (a) Size and resolution of the microcamera's FOV used in *in vivo* recordings were measured using a USAF resolution test chart. **(b)** FOVs in different sizes have different corresponding central and corner resolutions. **(c)** Images present the central and corner resolutions measured using the USAF resolution test chart. **(d)** Power spectral density of the blue excitation light provided by the 460 nm laser-coupled fiber bundle. **(e)** Image of fluorescent microbeads coated underneath the 4-plane implant captured by the mini-MCAM. f. Image of brain slide captured by the microcamera.

Benchtop testing was used to evaluate the optical performance of the mini-MCAM Before *in vivo* experiments. First, the size and central resolution of the microcamera's FOV used in *in vivo* recordings were measured using a USAF resolution test chart. Here, the resolution refers to the shortest distance between 2 distinct lines in the USAF chart which is 9.9 µm at the center and

11.4 µm at the corner for the FOV of 4.53 × 2.55 mm (**Fig. 4.3.1a)**. Since cortical neuron's soma has a diameter of 10-20 µm [114], a resolution of 9.9 – 11.4 µm should be adequate for measuring neuronal activities. As for the FOV of 4.53 × 2.55 mm used in the *in vivo* recording, ~68 % area of the implant's rectangle window, in a size of 3.82 × 3.82 mm (**Fig. 4.3.2a**), can be imaged by 1 microcamera. Also, the microcamera is just a modified off-shelf endoscope, and its FOV size is adjustable by simply changing the distance between the lens and CMOS (**Fig. 4.2.3c**). To study how the FOV affects the resolution, the central and corner resolutions are measured for different FOVs. As shown in **Figure. 4.3.1b** and **c**, the smallest achievable FOV of 3.56 × 1.99 mm has a central resolution of 8.8 µm and a corner resolution of 11 µm. Once the FOV was increased to 5.50 × 3.56 mm, its central and corner resolutions degraded to 12.5 µm and 13.9 µm. In the largest achievable FOV of 13.45 × 7.57 mm, the central and corner resolutions were measured to be 27.9 µm and 49.6 µm, which can only be used for mesoscale brain imaging demonstrated in our previous study [52]. In the in vivo recording, the FOV of 4.53 × 2.55 mm was selected.

Resolution is just 1 of 2 factors deciding whether the Calcium imaging tool can successfully capture single-cell activity in GCaMP6f mice. The other factor is the excitation light which excites the Calcium indicators to reveal the Calcium activity through the indicator's fluorescent light [117]. The excitation light's power spectral density was measured; its intensity centered at ~ 460 ± 5 nm (**Fig. 4.3.1d**), and it did not exceed 500 nm above the fluorescent Calcium signals. Further, the 460 nm excitation light was also proved effective for brain imaging GCaMP6m mice in a previous study [118]. Besides wavelength, the sufficient intensity of excitation light also matters to have good imaging results. The light intensities of the four individual optical fibers

were measured to be ~ 5.5 mW for Fiber 1, ~ 5.8 mW for Fiber 2, ~ 5.5 mW for Fiber 3, and ~ 6.7 mW for Fiber 4. To evaluate the excitation light's effectiveness, under this blue light, 10 μm fluorescence microbeads coated underneath the windows were imaged using the microcameras (**Fig. 4.3.1e**), and the image of individual neurons in a brain slide was also imaged using the same setup (**Fig. 4.3.1e**). Therefore, all these results suggest that the mini-MCAM is ready for *in vivo* experiments and used to measure neural activity at single-cell resolution.

In vivo testing of mini-MCAM

Calcium imaging of spontaneous brain activity in head-fixed mouse

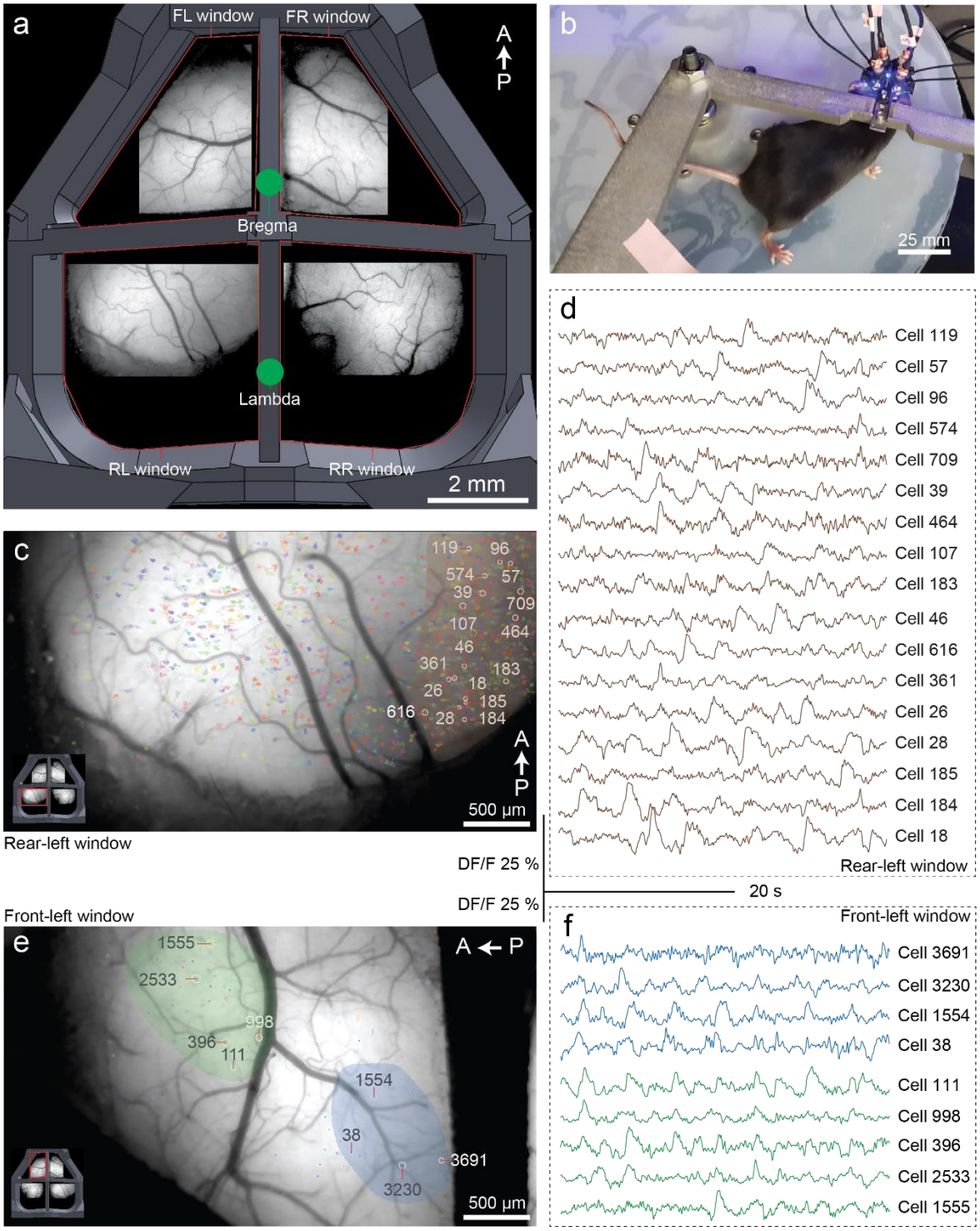

Figure 4.3.2 | Head-fixed recording of spontaneous brain activity: **(a)** FOV of mini-MCAM compared with the 4-plane transparent skull implant. Each microcamera's FOV aligns with its targeted window. The whole FOV of the mini-MCAM consists of a front-left (FL) window, a front-right (FR) window, a rear-left (RL) window, and a rear-right (RR) window. **(b)** Setup of the experiment: the mouse was headfixed on a disk treadmill which was also used in the *in vivo* experiments of **Chapters 2** and **3** when brain imaging was taken. **(c)** Calcium image of the brain region under the RL window. Green-labeled region highlights the neurons locating in the Retrosplenial cortex. **(d)** Plot of Calcium signals in DF/F extracted from the selected neurons in RL window using imaging processing software suite2p. **(e)** Calcium image of the brain region under the FL window. Blue-labeled region highlights the neurons locating in the sensory cortex. Green-labeled region highlights the neurons in the motor cortex. **(f)** Plot of Calcium signals in DF/F extracted from the selected neurons in FL window using imaging processing software suite2p.

To evaluate the *in vivo* imaging performance of mini-MCAM, the mini-MCAM was used to record the spontaneous brain activity in a head-fixed mouse walking on a disk treadmill (**Fig. 4.3.2b**). This experiment recorded mesoscale and single neurons' activities of four brain regions under the 4-plane transparent implant (**Fig. 4.3.2a**). The FOVs of the four microcameras imaged multiple brain regions across the brain, including parts of the motor cortex, sensory cortex, auditory cortex, Retrosplenial cortex, and visual cortex. The implant's rear-left (RL) window and the front-left (FL) window are selected to present single neurons' Calcium activities, where the signals of 17 representative cells (cell 119, 57, 96, 574, 709, 39, 464, 107, 183, 46, 616, 361, 26, 28, 185, 184, and 18) locating in the Retrosplenial cortex were extracted from the recorded video and plotted (**Fig. 4.3.2d**). Meanwhile, more than 1200 cells in the RL window were identified by suite2p [119]. As shown in **Figure 4.3.2f**, in the front-left (FL) window, Calcium signals of 5 representative cells (cell 111, 998, 396, 2533, and 1555) locating in the motor cortex and four cells (cell 3691, 3230, 1554, 38) locating in the sensory cortex were also extracted and plotted.

More than 3500 cells in the FL window were identified by suite2p. The plotted Calcium signals in DF/F all have magnitudes > 15%, and all the neighboring cells appear to have distinctive spike activities (**Fig. 4.3.2d** and **f**). Therefore, the mini-MCAM successfully demonstrated proof-of-concept *in vivo* recording in a headfixed mouse.

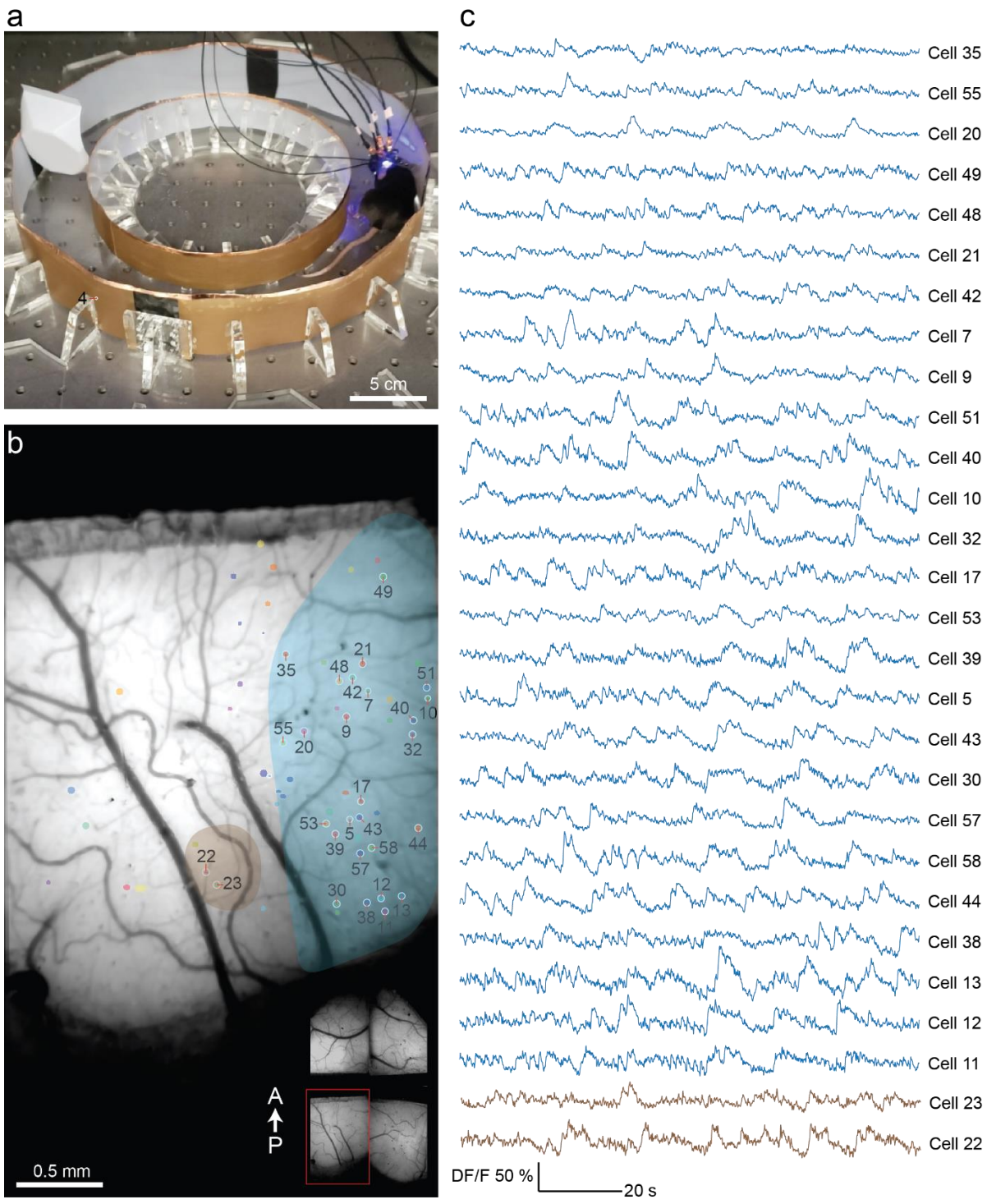

Figure 4.3.3 | Calcium imaging of spontaneous brain activity in freely behaving mouse: (a) The experiment setup: the mouse explored in an O-shape arena when mini-MCAM was recording. **(b)** Calcium image of the brain region under the rear-right window. Blue-labeled area highlights the neurons locating in the Retrosplenial cortex.

Brown-labeled area highlights neurons locating in the visual cortex. **(c)** Plot of Calcium signals in DF/F extracted from the selected neurons in RL window using imaging processing software suite2p.

Mini-MCAM was also used to record spontaneous brain activity in a freely behaving mouse. The weight of mini-MCAM was measured to be ~4.5g, which is too heavy and exceeds 10% of the subject's body weight of ~34g. According to our previous study [52], the weight of the imaging device should not exceed 10% of the animal's weight, which is 3.4g under this circumstance. However, a study of miniaturized 2p-microscopy performing brain imaging in freely behaving mice shows that 5g device carried by 32-35 g mice had minimal effect on the mice's movement [120]. In this experiment, the subject was trained for 1 week (30 minutes per day) to carry the mini-MCAM when placed in an O-shape arena to explore the arena freely. In the RL window, suite2p identified more than 200 neurons (**Fig. 4.3.3b**). Figure 4.3.3c shows the representative Calcium signals of 26 neurons in the Retrosplenial cortex, and 2 neurons in the visual cortex were extracted and plotted where distinctive spike activities within all these neighboring cells can be found. Thus, the mini-MCAM demonstrated proof-of-concept *in vivo* recording in freely behaving animals at single-cell resolution.

4.4 Methods

The 4-plane transparent skull implant assembly

As shown in **Figure 4.2.3d**, to assemble the 4-plane transparent skull implant, a 150 μm thick PET film was first laser-cut into 2 square windows of 3.8 x 3.8 mm and 2 triangle windows of 3.8 x 4 mm, then installed and bonded on a 3D printed PMMA window frame using optical

adhesive (Thorlabs, NOA61). To harden the flexible PET window, 0.025 ml negative photoresist SU-8 monomers dissolved in 1 wt% cyclopentanone were dropped cast on the window and polymerized to form a hardened glass-like transparent layer, in which the implant was pre-baked at a ramping temperature from 60 ℃ to 90 ℃ for 1 min, then placed under 365 nm UV light to polymerize the monomer following by post-baked at a ramping temperature from 60℃ to 90℃. Three holes of the 3D-printed window frame were threaded using a 0-80 tap for a titanium headfixation structure to be installed (**Fig. 4.2.3d**).

Imaging component assembly

The fully assembled device has 4 microcameras. Each microcamera is a modified endoscope (MISUMI, TD-B209M3-76-01). As shown in **Figure 4.2.3c**, to assemble one microcamera, an emission filter of 525 ± 25 nm (Chroma. Inc., ET525/50m 4mm Dia) was bonded on the endoscope's original objective lens using optical glue (Thorlabs, NOA61). A heat-conductive Copper tape was partially wrapped around the emission filter as a protector preventing accidental collision with the emission filter. The endoscope attached to the emission filter was placed in an aluminum heat sink tube with an inner diameter of 4mm and an outer diameter of 4.5 mm. Four microcameras were individually installed into the microcamera slots of a 3D printed PMMA camera/fiber holder, where four optical fibers were also installed into the fiber slots of the camera/fiber holder that each fiber individually targets at a window of the 4-plane transparent skull implant.

Illumination component assembly

The illumination component is mainly a laser-coupled optical fiber bundle. As shown in **Figure 4.2.3b**, a bundle of four acrylic optical fibers of 500 μm diameter was inserted into and bonded to a custom-built laser-cut acrylic fiber adaptor to assemble the illumination component. The end of the fiber bundle was polished first using 600-grade sandpaper and then 2000-grade sandpaper to create a perpendicular surface facing the blue laser light. The fiber adaptor, the excitation filter of 469 ± 17.5 nm (Thorlabs, Inc., MF 469-35), and a custom-built laser-cut laser diode adaptor were installed into a lens tube (Thorlabs, SM01) where the 460 nm laser diode was attached to the laser diode adaptor.

Surgical implantation and animal caring

The surgical implantation and animal caring follow the same procedure and protocol described in **Chapter 2**, the fully desktop-fabricated Graphene ECoG electrode array.

***In vivo* brain imaging**

In this study, all the *in vivo* recording data was collected from an 8-mouth old female GCaMP6 Ai163-cux2 mouse. The setup of headfixed recording followed the same procedure of studies in **Chapter 2** and **Chapter 3**. In the freely behaving experiment, the mouse mounted with mini-MCAM was placed in an O-shape arena to explore the space. 8 trials of brain recording were taken, and each trial lasted ~1 minute.

Data acquisition and analysis

An open-source multi-camera interfacing software OBS studio developed OBS Project was used to record the brain image and save the video in mp4 format. To analyze the data, the video was first converted into avi format through a MATLAB script and then analyzed by an open-source cell detection software called suite2p developed by cortex-lab. When analyzing the video, the suite2p automatically identified and located the regions of interest (ROI) behaving like a neuron and extracted the Calcium signals of the neurons and their surrounding backgrounds. The Calcium signal waveform in DF/F, relative signal to baseline, was plotted by a MATLAB script (MathWorks. MATLAB).

4.5 Summary

Chapter 4 presents a miniaturized brain imaging device, mini-MCAM, an array of four microcameras individually targeting four planar brain surfaces confronted by a 4-plane transparent skull implant. As a proof-of-concept device, mini-MCAM has a merged FOV of ~ 34 mm^2 and successfully demonstrated *in vivo* recording of cortex-wide spontaneous brain activity at single-cell resolution in moue under head-fixed and freely behaving conditions. Therefore, mini-MCAM shows a strong potential to become the ideal neural activity sensing technology defined in this thesis.

Chapter 5 Conclusion and future perspectives

Mapping and decoding the brain's neural network bring a further understanding of the brain, from which the knowledge can be used to improve the quality of human life by seeking better treatments for neurological disorders and enhancing brain functions. To gather more insights into the brain, neural activity sensing technologies have been continuously developed and improved. In this thesis, a concept of the ideal neural activity sensing technology is introduced, that this technology can perform cortex-wide brain recording at single-cell resolution in freely behaving animals with high accessibility. To approach the ideal neural activity sensing technology, the neural activity sensing tools presented in this thesis aimed to improve one more aspect of existing neural activity sensing tools with corresponding benchtop characterization tests and in vivo experiments.

Fully desktop-fabricated flexible graphene electrocorticography (ECoG) arrays

Chapter 2 presents a fully-desktop fabricated ECoG electrode array that can be built using off-shelf materials and common bio-laboratory tools. The electrode array was patterned by stencil printing graphene ink. The highly stable graphene ink formulated by exfoliating graphene in a biocompatible solvent Cyrene [92] demonstrated a high conductivity of ~ 1.1×10^3 $S \cdot cm^{-1}$. Mechanical bending tests showed no significant change in electrode impedance at a flat surface and various radii of curvature ranging from 14 mm to 6 mm. Fully functional devices and the encapsulation of PDMS insulation were highly stable even under the accelerated aging environment, maintaining an average impedance of ~ 6.49 ± 4.16 kΩ on day 15. Furthermore, the electrodes remained functional with an average impedance magnitude of 24.72 ± 95.23 kΩ (1 kHz)

throughout the implantation. Thus, our graphene ECoG arrays provide robust neural interfaces that can be applied for chronic electrophysiology studies in mice.

To our knowledge, all the existing micrometer-scale ECoG devices are fully or partially fabricated using microfabrication or specialized techniques [32]–[37], [39], [93]–[95], resulting in high cost and low accessibility to neuroscience laboratories. In our method, the stencils determining the layout of the electrodes can be rapidly reconfigured using CAD tools and fabricated using desktop laser cutters available in most university fabrication shops. The graphene ink can be formulated using standard lab equipment, and the patterned electrodes can be sintered on a laboratory hotplate. The insulation layer can be deposited by a homebuilt, microcontroller-based spinner or a low-cost off-the-shelf spin coater. We have created the first fully desktop-fabricated, flexible micrometer-scale ECoG array that can be chronically implanted in mice. These results point a way forward for creating robust, open-source, flexible neural interfaces that can be widely used in basic and translational neuroscience research.

Several directions can be pursued in the future, building upon the graphene ECoG devices presented in this work. The size of the implant can be extended to much larger regions of the brain [52], [53] so that the whole visual cortex and motor cortex can be included for performing ECoG recording over most of the cortical surface of the mouse brain [45]. The low and stable impedance of the electrodes can be leveraged for precise cortical micro-stimulation [31]. Miniaturization of electronic interface circuits can also allow deployment in freely behaving animals, potentially combined with imaging instrumentation for simultaneously tracking large-scale calcium dynamics [52]. Further, graphene has shown utility in passive sensing of electrical potentials and

functionalizing to highly sensitive biochemical sensing [99]. Overall, our method can be scaled to mass manufacturing of flexible graphene-based biosensors at a low cost with a myriad of applications in biological sensings, such as electrocardiography [100], electromyography [101], and peripheral nerve interfacing [102].

3D-printed transparent ECoG electrode arrays for simultaneous ECoG and Ca^{2+} imaging

Chapter 3 presents a 3D-printed transparent ECoG electrode array conducting simultaneous ECoG recording and Calcium imaging in the mice to achieve finer spatial resolution than traditional ECoG. On the one hand, for Calcium imaging, the transparent ECoG electrodes provide optical access to the brain with a measured transmission of 89.96 ± 1.67%. On the other hand, for the ECoG recording, the electrodes remained functional after 15 days of implantation in mice and were measured to have low impedances < 300 kΩ. When performing *in vivo* recording, the ECoG array successfully measured the stimuli-evoked brain activity and anesthesia drug-induced brain activity, in which the ECoG's electrical signal was found to be significantly correlated with the Calcium's optical signal with a cross-correlation coefficient > 75%. Thanks to this correlation, ECoG's high temporal resolution, and Calcium's fine spatial resolution can better map the brain's neural network leading to a better understanding of the brain [121].

As for the fabrication, the 3D-printed ECoG array also simplifies the fabrication procedures of existing transparent ECoG arrays, highly relying on cleanroom facilities [29], [30], [43], [44]. The 3D-printed electrodes were built using only 1 extrusion 3D printer, which can precisely pattern the transparent PEDOT:PSS ink to form the electrodes and the transparent SU-8

photoresist ink to insulate the electrodes. All these inks are off-shelf products and can be purchased from supplier Sigma-Aldrich.

Several directions can be pursued to improve and deploy this ECoG array. Currently, the ECoG array only has 8 electrodes to monitor the ECoG signals of neural activities in 8 regions under the electrodes. These 8 regions (**Fig. 3.3.2 a**) are too small for cortex-wide ECoG recording. To resolve this issue, a 3D-printed high-density 64-channel ECoG array is under development by refining the printing setting to reduce the electrode size. To deploy the ECoG array into research, the transparent ECoG array can collect the brain's electrical activity feedback in responding to optical stimulation. Thanks to the different signal types, the electrical feedback and optical stimulation signals will not interrupt each other [29]. Furthermore, due to the high scalability of 3D printing and the ECoG array's flexibility, the ECoG array can be easily modified for biological sensing applications such as skin electrodes [122], neural cuff electrodes [123], and Electrocardiography electrodes [124].

Miniaturized micro-camera array microscopy (mini-MCAM) for cortex-wide Calcium imaging at single-cell resolution in head-fixed or freely behaving mouse

Chapter 4 presents a miniaturized microcamera array microscopy (mini-MCAM) which performs cortex-wide Calcium imaging at single-cell resolution in head-fixed and freely behaving mice. Mini-MCAM weighed 4.5g and was built using off-shelf endoscopes. To create optical access to the brain for the mini-MCAM, a 4-plane transparent skull implant was developed. This optical access gave mini-MCAM a total FOV of ~35 mm^2, which includes most

of the bilateral primary and secondary motor cortices, most of the somatosensory cortex areas, the Retrosplenial, association, higher visual, and part of the primary visual cortex. Besides this large FOV, the resolution of the mini-MCAM was measured to be 9.9 – 11 μm, which is feasible for recording the single neuron's activity [116]. The blue excitation light of Mini-MCAM was measured to be 460 nm with a light intensity of 5.8 ± 0.6 mW, which was proved sufficient to capture images of fluorescence microbeads and neurons in brain slide samples. Furthermore, in the *in vivo* brain imaging, mini-MCAM successfully recorded spontaneous brain activity at single-cell resolution in head-fixed and freely behaving mice. All these results indicate that mini-MCAM, as a proof-of-concept device, presents a promising direction of device development to approach the ideal neural activity sensing technology.

Based on the current accomplished benchtop optical and *in vivo* imaging performances, several improvements can be pursued in future development. First, the excitation light was not uniformly projected on the brain surface, making the central region of the brain under the implant window brighter than the edges. This non-uniform light projection makes cell detection challenging because the brighter region saturated the image's brightness and submerged the cells' Calcium signals. In this study, to temporally resolve this issue, neurons located in the brighter regions were manually selected based on their twinkling somas' Calcium activities in the recorded video. In the future, the cell-detection setting in the current processing software can be optimized, and the optical fiber can be modified by adding an extra diffuser to provide a more uniform light projection to the brain's surface. Secondly, rather than recording spontaneous brain activity, behavior, and stimulation studies can be beneficial for mini-MCAM to map the neural network and study the interactions within neurons and different functional regions [114]–[116]. Thirdly,

mini-MCAM's weight of 4.5g is questionable for freely behaving studies based on the mesoscope standard because it exceeds 10% body weights of most mice, ~ 32g [52]. To reduce the weight, the Aluminum and Copper heat sink should be miniaturized or replaced with lighter materials.

425 7th Street South, Minneapolis, MN, 55415

From fully desktop-fabricated Graphene ECoG array to 3D-printed transparent ECoG array to mini-MCAM, this thesis demonstrates how engineering can support fundamental brain study by developing optical and electrophysiological technologies for monitoring cortex-wide brain activity. With the author's sincere desire, this work is expected to serve humankind to better understand the brain for continuously improving quality of life and performance.

References:

[1] W. Singer, “Understanding the brain. How can our intuition fail so fundamentally when it comes to studying the organ to which it owes its existence?,” *EMBO Rep*, vol. 8, no. SUPPL. 1, 2007, doi: 10.1038/sj.embor.7400994.

[2] I. TORRES, “Human Behavior and the Developing Brain,” *American Journal of Psychiatry*, vol. 152, no. 4, 1995, doi: 10.1176/ajp.152.4.637-a.

[3] A. Moustafa, *Computational Models of Brain and Behavior*. 2017. doi: 10.1002/9781119159193.

[4] D. L. Chao, L. Ma, and K. Shen, “Transient cell-cell interactions in neural circuit formation,” *Nature Reviews Neuroscience*, vol. 10, no. 4. 2009. doi: 10.1038/nrn2594.

[5] E. J. Hwang *et al.*, “Disengagement of motor cortex from movement control during long-term learning,” *Sci Adv*, vol. 5, no. 10, 2019, doi: 10.1126/sciadv.aay0001.

[6] M. Jafari *et al.*, “The human primary somatosensory cortex encodes imagined movement in the absence of sensory information,” *Commun Biol*, vol. 3, no. 1, 2020, doi: 10.1038/s42003-020-01484-1.

[7] H. J. ten Donkelaar, J. Broman, and P. van Domburg, “The somatosensory system,” in *Clinical Neuroanatomy: Brain Circuitry and Its Disorders*, 2020. doi: 10.1007/978-3-030-41878-6_4.

[8] C. Stringer, M. Michaelos, D. Tsyboulski, S. E. Lindo, and M. Pachitariu, “High-precision coding in visual cortex,” *Cell*, vol. 184, no. 10, 2021, doi: 10.1016/j.cell.2021.03.042.

[9] S. K. Karadimas *et al.*, “Sensory cortical control of movement,” *Nat Neurosci*, vol. 23, no. 1, 2020, doi: 10.1038/s41593-019-0536-7.

[10] M. W. Spratling, “Cortical region interactions and the functional role of apical dendrites.,” *Behavioral and cognitive neuroscience reviews*, vol. 1, no. 3. 2002. doi: 10.1177/1534582302001003003.

[11] I. Gaudet, A. Hüsser, P. Vannasing, and A. Gallagher, “Functional Brain Connectivity of Language Functions in Children Revealed by EEG and MEG: A Systematic Review,” *Front Hum Neurosci*, vol. 14, 2020, doi: 10.3389/fnhum.2020.00062.

[12] K. J. Friston, “Functional and Effective Connectivity: A Review,” *Brain Connect*, vol. 1, no. 1, 2011, doi: 10.1089/brain.2011.0008.

[13] J. D. Bijsterbosch *et al.*, “The relationship between spatial configuration and functional connectivity of brain regions,” *Elife*, vol. 7, 2018, doi: 10.7554/eLife.32992.

[14] F. X. Castellanos, A. di Martino, R. C. Craddock, A. D. Mehta, and M. P. Milham, “Clinical applications of the functional connectome,” *Neuroimage*, vol. 80, 2013, doi: 10.1016/j.neuroimage.2013.04.083.

[15] V. P. Clark and R. Parasuraman, “Neuroenhancement: Enhancing brain and mind in health and in disease,” *NeuroImage*, vol. 85. 2014. doi: 10.1016/j.neuroimage.2013.08.071.

[16] B. A. Coffman, M. C. Trumbo, and V. P. Clark, “Enhancement of object detection with transcranial direct current stimulation is associated with increased attention,” *BMC Neurosci*, vol. 13, no. 1, 2012, doi: 10.1186/1471-2202-13-108.

[17] V. P. Clark, B. A. Coffman, M. C. Trumbo, and C. Gasparovic, “Transcranial direct current stimulation (tDCS) produces localized and specific alterations in neurochemistry: A 1H magnetic resonance spectroscopy study,” *Neurosci Lett*, vol. 500, no. 1, 2011, doi: 10.1016/j.neulet.2011.05.244.

[18] B. Falcone, B. A. Coffman, V. P. Clark, and R. Parasuraman, “Transcranial direct current stimulation augments perceptual sensitivity and 24-hour retention in a complex threat detection task.,” *PLoS One*, vol. 7, no. 4, 2012, doi: 10.1371/journal.pone.0034993.

[19] B. Luber and S. H. Lisanby, “Enhancement of human cognitive performance using transcranial magnetic stimulation (TMS),” *NeuroImage*, vol. 85. 2014. doi: 10.1016/j.neuroimage.2013.06.007.

[20] N. Naseer, H. Ayaz, and F. Dehais, “Portable and Wearable Brain Technologies for Neuroenhancement and Neurorehabilitation,” *BioMed Research International*, vol. 2018. 2018. doi: 10.1155/2018/1806374.

[21] G. Hong and C. M. Lieber, “Novel electrode technologies for neural recordings,” *Nature Reviews Neuroscience*, vol. 20, no. 6. 2019. doi: 10.1038/s41583-019-0140-6.

[22] R. Cossart, Y. Ikegaya, and R. Yuste, “Calcium imaging of cortical networks dynamics,” *Cell Calcium*, vol. 37, no. 5 SPEC. ISS. 2005. doi: 10.1016/j.ceca.2005.01.013.

[23] M. Soufineyestani, D. Dowling, and A. Khan, “Electroencephalography (EEG) technology applications and available devices,” *Applied Sciences (Switzerland)*, vol. 10, no. 21. 2020. doi: 10.3390/app10217453.

[24] S. Noachtar and J. Rémi, “The role of EEG in epilepsy: A critical review,” *Epilepsy and Behavior*, vol. 15, no. 1. 2009. doi: 10.1016/j.yebeh.2009.02.035.

[25] R. Bhandari, S. Negi, and F. Solzbacher, “Wafer-scale fabrication of penetrating neural microelectrode arrays,” *Biomed Microdevices*, vol. 12, no. 5, 2010, doi: 10.1007/s10544-010-9434-1.

[26] D. K. Rangel Guerrero, J. G. Donnett, J. Csicsvari, and K. A. Kovács, “Tetrode recording from the hippocampus of behaving mice coupled with four-point-irradiation closed-loop optogenetics: A technique to study the contribution of hippocampal SWR events to learning,” *eNeuro*, vol. 5, no. 4, 2018, doi: 10.1523/ENEURO.0087-18.2018.

[27] P. Pochay, K. D. Wise, L. F. Allard, and L. T. Rutledge, “A Multichannel Depth Probe Fabricated Using Electron-Beam Lithography,” *IEEE Trans Biomed Eng*, vol. BME-26, no. 4, 1979, doi: 10.1109/TBME.1979.326558.

[28] C. Marin and E. Fernández, “Biocompatibility of intracortical microelectrodes: Current status and future prospects,” *Front Neuroeng*, vol. 3, no. MAY, 2010, doi: 10.3389/fneng.2010.00008.

[29] P. D. Donaldson *et al.*, “Polymer Skulls With Integrated Transparent Electrode Arrays for Cortex-Wide Opto-Electrophysiological Recordings,” *Adv Healthc Mater*, 2022, doi: 10.1002/adhm.202200626.

[30] D. W. Park *et al.*, “Graphene-based carbon-layered electrode array technology for neural imaging and optogenetic applications,” *Nat Commun*, vol. 5, 2014, doi: 10.1038/ncomms6258.

[31] D. W. Park *et al.*, “Electrical Neural Stimulation and Simultaneous in Vivo Monitoring with Transparent Graphene Electrode Arrays Implanted in GCaMP6f Mice,” *ACS Nano*, vol. 12, no. 1, 2018, doi: 10.1021/acsnano.7b04321.

[32] W. R. Lee, C. Im, C. S. Koh, J. M. Kim, H. C. Shin, and J. M. Seo, “A convex-shaped, PDMS-parylene hybrid multichannel ECoG-electrode array,” in *Proceedings of the Annual International Conference of the IEEE Engineering in Medicine and Biology Society, EMBS*, 2017. doi: 10.1109/EMBC.2017.8037018.

[33] K. Y. Kwon, B. Sirowatka, A. Weber, and W. Li, “Opto-μ ECoG array: A hybrid neural interface with transparent μ ECoG electrode array and integrated LEDs for optogenetics,” *IEEE Trans Biomed Circuits Syst*, vol. 7, no. 5, 2013, doi: 10.1109/TBCAS.2013.2282318.

[34] M. Vomero *et al.*, “Achieving Ultra-Conformability with Polyimide-Based ECoG Arrays,” in *Proceedings of the Annual International Conference of the IEEE Engineering in Medicine and Biology Society, EMBS*, 2018, vol. 2018-July. doi: 10.1109/EMBC.2018.8513171.

[35] P. Ledochowitsch, E. Olivero, T. Blanche, and M. M. Maharbiz, “A transparent ECoG array for simultaneous recording and optogenetic stimulation,” in *Proceedings of the Annual International Conference of the IEEE Engineering in Medicine and Biology Society, EMBS*, 2011. doi: 10.1109/IEMBS.2011.6090808.

[36] V. Woods *et al.*, “Long-term recording reliability of liquid crystal polymer μ ECoG arrays,” *J Neural Eng*, vol. 15, no. 6, 2018, doi: 10.1088/1741-2552/aae39d.

[37] A. F. Renz *et al.*, “Opto-E-Dura: A Soft, Stretchable ECoG Array for Multimodal, Multiscale Neuroscience,” *Adv Healthc Mater*, vol. 9, no. 17, 2020, doi: 10.1002/adhm.202000814.

[38] T. Kaiju *et al.*, “High spatiotemporal resolution ECoG recording of somatosensory evoked potentials with flexible micro-electrode arrays,” *Front Neural Circuits*, vol. 11, 2017, doi: 10.3389/fncir.2017.00020.

[39] W. Yang *et al.*, “A fully transparent, flexible PEDOT:PSS-ITO-Ag-ITO based microelectrode array for ECoG recording,” *Lab Chip*, vol. 21, no. 6, 2021, doi: 10.1039/d0lc01123a.

[40] M. Shokoueinejad *et al.*, “Progress in the field of micro-electrocorticography,” *Micromachines*, vol. 10, no. 1. 2019. doi: 10.3390/mi10010062.

[41] N. Jeremy Hill *et al.*, “Recording human electrocorticographic (ECoG) signals for neuroscientific research and real-time functional cortical mapping,” *Journal of Visualized Experiments*, no. 64, 2012, doi: 10.3791/3993.

[42] K. J. Yu *et al.*, “Bioresorbable silicon electronics for transient spatiotemporal mapping of electrical activity from the cerebral cortex,” *Nat Mater*, vol. 15, no. 7, 2016, doi: 10.1038/nmat4624.

[43] P. D. Donaldson and S. L. Swisher, “Transparent, Low-Impedance Inkjet-Printed PEDOT:PSS Microelectrodes for Multimodal Neuroscience,” *Physica Status Solidi (A) Applications and Materials Science*, 2022, doi: 10.1002/pssa.202100683.

[44] P. D. Donaldson, L. Ghanbari, M. L. Rynes, S. B. Kodandaramaiah, and S. L. Swisher, “Inkjet-Printed Silver Electrode Array for in-vivo Electrocorticography,” in *International IEEE/EMBS Conference on Neural Engineering, NER*, 2019, vol. 2019-March. doi: 10.1109/NER.2019.8717083.

[45] P. D. Donaldson *et al.*, “Polymer skulls with integrated transparent electrode arrays for cortex-wide opto-electrophysiological recordings,” *bioRxiv*, p. 2021.11.13.468490, Jan. 2021, doi: 10.1101/2021.11.13.468490.

[46] D. Kuzum *et al.*, “Transparent and flexible low noise graphene electrodes for simultaneous electrophysiology and neuroimaging,” *Nat Commun*, vol. 5, 2014, doi: 10.1038/ncomms6259.

[47] Y. Liang, A. Offenhäusser, S. Ingebrandt, and D. Mayer, “PEDOT:PSS-Based Bioelectronic Devices for Recording and Modulation of Electrophysiological and Biochemical Cell Signals,” *Advanced Healthcare Materials*, vol. 10, no. 11. 2021. doi: 10.1002/adhm.202100061.

[48] D. J. Wallace and J. N. D. Kerr, “Circuit interrogation in freely moving animals,” *Nature Methods*, vol. 16, no. 1. 2019. doi: 10.1038/s41592-018-0275-9.

[49] Z. Yao *et al.*, “A transcriptomic and epigenomic cell atlas of the mouse primary motor cortex,” *Nature*, vol. 598, no. 7879, 2021, doi: 10.1038/s41586-021-03500-8.

[50] S. Chen *et al.*, “Miniature Fluorescence Microscopy for Imaging Brain Activity in Freely-Behaving Animals,” *Neuroscience Bulletin*, vol. 36, no. 10. 2020. doi: 10.1007/s12264-020-00561-z.

[51] Y. Li *et al.*, “Serotonin neurons in the dorsal raphe nucleus encode reward signals,” *Nat Commun*, vol. 7, 2016, doi: 10.1038/ncomms10503.

[52] M. L. Rynes *et al.*, “Miniaturized head-mounted microscope for whole-cortex mesoscale imaging in freely behaving mice,” *Nat Methods*, vol. 18, no. 4, 2021, doi: 10.1038/s41592-021-01104-8.

[53] L. Ghanbari *et al.*, “Cortex-wide neural interfacing via transparent polymer skulls,” *Nat Commun*, vol. 10, no. 1, 2019, doi: 10.1038/s41467-019-09488-0.

[54] X. Liu *et al.*, “Decoding of cortex-wide brain activity from local recordings of neural potentials,” *J Neural Eng*, vol. 18, no. 6, 2021, doi: 10.1088/1741-2552/ac33e7.

[55] D. Aharoni and T. M. Hoogland, “Circuit investigations with open-source miniaturized microscopes: Past, present and future,” *Frontiers in Cellular Neuroscience*, vol. 13. 2019. doi: 10.3389/fncel.2019.00141.

[56] S. Srinivasan *et al.*, “Miniaturized microscope with flexible light source input for neuronal imaging and manipulation in freely behaving animals,” *Biochem Biophys Res Commun*, vol. 517, no. 3, 2019, doi: 10.1016/j.bbrc.2019.07.082.

[57] X. Wu *et al.*, “A Modified Miniscope System for Simultaneous Electrophysiology and Calcium Imaging in vivo,” *Front Integr Neurosci*, vol. 15, 2021, doi: 10.3389/fnint.2021.682019.

[58] S. L. West *et al.*, “Wide-Field Calcium Imaging of Dynamic Cortical Networks during Locomotion,” *Cerebral Cortex*, 2021, doi: 10.1093/cercor/bhab373.

[59] S. W. Cramer *et al.*, “Wide-field Calcium Imaging Reveals Widespread Changes in Cortical Connectivity Following Repetitive, Mild Traumatic Brain Injury in the Mouse,” *bioRxiv*, 2022.

[60] J. Kim, M. Lee, J. S. Rhim, P. Wang, N. Lu, and D. H. Kim, “Next-generation flexible neural and cardiac electrode arrays,” *Biomedical Engineering Letters*, vol. 4, no. 2. 2014. doi: 10.1007/s13534-014-0132-4.

[61] D. Khodagholy *et al.*, “NeuroGrid: Recording action potentials from the surface of the brain,” *Nat Neurosci*, vol. 18, no. 2, 2015, doi: 10.1038/nn.3905.

[62] I. Rachinskiy *et al.*, “High-Density, Actively Multiplexed µECoG Array on Reinforced Silicone Substrate,” *Frontiers in Nanotechnology*, vol. 4, 2022, doi: 10.3389/fnano.2022.837328.

[63] M. Ryu *et al.*, “Enhancement of Interface Characteristics of Neural Probe Based on Graphene, ZnO Nanowires, and Conducting Polymer PEDOT,” *ACS Appl Mater Interfaces*, vol. 9, no. 12, 2017, doi: 10.1021/acsami.7b02975.

[64] A. Bourrier *et al.*, “Monolayer Graphene Coating of Intracortical Probes for Long-Lasting Neural Activity Monitoring,” *Adv Healthc Mater*, vol. 8, no. 18, 2019, doi: 10.1002/adhm.201801331.

[65] A. K. Geim and K. S. Novoselov, “The rise of graphene,” *Nat Mater*, vol. 6, no. 3, 2007, doi: 10.1038/nmat1849.

[66] R. F. Hossain, I. G. Deaguero, T. Boland, and A. B. Kaul, “Biocompatible, large-format, inkjet printed heterostructure MoS 2-graphene photodetectors on conformable substrates,” *NPJ 2D Mater Appl*, vol. 1, no. 1, pp. 1–10, 2017.

[67] R. R. Nair *et al.*, “Fine structure constant defines visual transparency of graphene,” *Science (1979)*, vol. 320, no. 5881, 2008, doi: 10.1126/science.1156965.

[68] T. C. Cristarella, A. J. Chinderle, J. Hui, and J. Rodríguez-López, “Single-layer graphene as a stable and transparent electrode for nonaqueous radical annihilation electrogenerated chemiluminescence,” *Langmuir*, vol. 31, no. 13, 2015, doi: 10.1021/la5050317.

[69] J. Voigts, J. Siegle, D. L. Pritchett, and C. I. Moore, “The flexDrive: An ultra-light implant for optical control and highly parallel chronic recording of neuronal ensembles in freely moving mice,” *Front Syst Neurosci*, no. MARCH 2013, 2013, doi: 10.3389/fnsys.2013.00008.

[70] W. J. Hyun, E. B. Secor, M. C. Hersam, C. D. Frisbie, and L. F. Francis, “High-resolution patterning of graphene by screen printing with a silicon stencil for highly flexible printed electronics,” *Advanced Materials*, vol. 27, no. 1, 2015, doi: 10.1002/adma.201404133.

[71] Y. Xu *et al.*, “Screen-printable thin film supercapacitor device utilizing graphene/polyaniline inks,” *Adv Energy Mater*, vol. 3, no. 8, 2013, doi: 10.1002/aenm.201300184.

[72] K. Yong, A. Ashraf, P. Kang, and S. Nam, “Rapid Stencil Mask Fabrication Enabled One-Step Polymer-Free Graphene Patterning and Direct Transfer for Flexible Graphene Devices,” *Sci Rep*, vol. 6, 2016, doi: 10.1038/srep24890.

[73] E. Jabari, F. Ahmed, F. Liravi, E. B. Secor, L. Lin, and E. Toyserkani, “2D printing of graphene: A review,” *2D Materials*, vol. 6, no. 4. 2019. doi: 10.1088/2053-1583/ab29b2.

[74] Y. Z. N. Htwe, M. K. Abdullah, and M. Mariatti, “Optimization of graphene conductive ink using solvent exchange techniques for flexible electronics applications,” *Synth Met*, vol. 274, 2021, doi: 10.1016/j.synthmet.2021.116719.

[75] A. M. Alamri, S. Leung, M. Vaseem, A. Shamim, and J.-H. He, “Fully inkjet-printed photodetector using a graphene/perovskite/graphene heterostructure,” *IEEE Trans Electron Devices*, vol. 66, no. 6, pp. 2657–2661, 2019.

[76] S. Casaluci, M. Gemmi, V. Pellegrini, A. di Carlo, and F. Bonaccorso, “Graphene-based large area dye-sensitized solar cell modules,” *Nanoscale*, vol. 8, no. 9, pp. 5368–5378, 2016.

[77] M. Silva, I. S. Pinho, J. A. Covas, N. M. Alves, and M. C. Paiva, “3D printing of graphene-based polymeric nanocomposites for biomedical applications,” *Functional Composite Materials*, vol. 2, no. 1, pp. 1–21, 2021.

[78] Y. Fang, J. G. D. Hester, W. Su, J. H. Chow, S. K. Sitaraman, and M. M. Tentzeris, “A bio-enabled maximally mild layer-by-layer Kapton surface modification approach for the fabrication of all-inkjet-printed flexible electronic devices,” *Sci Rep*, vol. 6, 2016, doi: 10.1038/srep39909.

[79] E. B. Secor, P. L. Prabhumirashi, K. Puntambekar, M. L. Geier, and M. C. Hersam, “Inkjet printing of high conductivity, flexible graphene patterns,” *J Phys Chem Lett*, vol. 4, no. 8, pp. 1347–1351, 2013.

[80] M. Michel, C. Biswas, and A. B. Kaul, “High-performance ink-jet printed graphene resistors formed with environmentally-friendly surfactant-free inks for extreme thermal environments,” *Appl Mater Today*, vol. 6, pp. 16–21, 2017.

[81] K. Pan *et al.*, “Sustainable production of highly conductive multilayer graphene ink for wireless connectivity and IoT applications,” *Nat Commun*, vol. 9, no. 1, 2018, doi: 10.1038/s41467-018-07632-w.

[82] M. M. Lucchese *et al.*, “Quantifying ion-induced defects and Raman relaxation length in graphene,” *Carbon N Y*, vol. 48, no. 5, 2010, doi: 10.1016/j.carbon.2009.12.057.

[83] I. Childres, L. A. Jauregui, W. Park, H. Caoa, and Y. P. Chena, “Raman spectroscopy of graphene and related materials,” in *New Developments in Photon and Materials Research*, 2013.

[84] R. F. Hossain and A. B. Kaul, “Biocompatible, Inkjet Printed Heterostructure Photodetector for Biosensing Applications,” in *31st Annual Conference of the IEEE Photonics Society, IPC 2018*, 2018. doi: 10.1109/IPCon.2018.8527301.

[85] S. F. Cogan, “Neural stimulation and recording electrodes,” *Annual Review of Biomedical Engineering*, vol. 10. pp. 275–309, 2008. doi: 10.1146/annurev.bioeng.10.061807.160518.

[86] Y. Shao, H. Wang, Q. Zhang, and Y. Li, “Fabrication of large-area and high-crystallinity photoreduced graphene oxide films via reconstructed two-dimensional multilayer structures,” *NPG Asia Mater*, vol. 6, no. 8, 2014, doi: 10.1038/am.2014.59.

[87] A. K. Yagati, J. Min, and S. Cho, “ Electrosynthesis of ERGO-NP Nanocomposite Films for Bioelectrocatalysis of Horseradish Peroxidase towards H 2 O 2 ,” *J Electrochem Soc*, vol. 161, no. 14, 2014, doi: 10.1149/2.1001414jes.

[88] N. J. Michelson and T. D. Y. Kozai, “Isoflurane and ketamine differentially influence spontaneous and evoked laminar electrophysiology in mouse V1,” *J Neurophysiol*, vol. 120, no. 5, 2018, doi: 10.1152/jn.00299.2018.

[89] A. Fontanini, P. F. Spano, and J. M. Bower, “Ketamine-xylazine-induced slow (<1.5 Hz) oscillations in the rat piriform (olfactory) cortex are functionally correlated with

respiration," *Journal of Neuroscience*, vol. 23, no. 22, 2003, doi: 10.1523/jneurosci.23-22-07993.2003.

[90] E. Hwang, J. M. McNally, and J. H. Choi, "Reduction in cortical gamma synchrony during depolarized state of slow wave activity in mice," *Front Syst Neurosci*, vol. 7, no. DEC, 2013, doi: 10.3389/fnsys.2013.00107.

[91] D. Valtakari, J. Liu, V. Kumar, C. Xu, M. Toivakka, and J. J. Saarinen, "Conductivity of PEDOT:PSS on Spin-Coated and Drop Cast Nanofibrillar Cellulose Thin Films," *Nanoscale Res Lett*, vol. 10, no. 1, 2015, doi: 10.1186/s11671-015-1093-y.

[92] C. Grune, J. Thamm, O. Werz, and D. Fischer, "Cyrene™ as an Alternative Sustainable Solvent for the Preparation of Poly(lactic-co-glycolic acid) Nanoparticles," *J Pharm Sci*, vol. 110, no. 2, 2021, doi: 10.1016/j.xphs.2020.11.031.

[93] G. Márton, G. Orbán, M. Kiss, R. Fiáth, A. Pongrácz, and I. Ulbert, "A multimodal, SU-8 - Platinum - Polyimide microelectrode array for chronic in vivo neurophysiology," *PLoS One*, vol. 10, no. 12, 2015, doi: 10.1371/journal.pone.0145307.

[94] J. D. Yeager, D. J. Phillips, D. M. Rector, and D. F. Bahr, "Characterization of flexible ECoG electrode arrays for chronic recording in awake rats," *J Neurosci Methods*, vol. 173, no. 2, 2008, doi: 10.1016/j.jneumeth.2008.06.024.

[95] M. Vomero *et al.*, "Glassy carbon electrocorticography electrodes on Ultra-Thin and Finger-Like Polyimide Substrate: Performance evaluation based on different electrode diameters," *Materials*, vol. 11, no. 12, 2018, doi: 10.3390/ma11122486.

[96] S. Lim, H. Park, G. Yamamoto, C. Lee, and J. W. Suk, “Measurements of the electrical conductivity of monolayer graphene flakes using conductive atomic force microscopy,” *Nanomaterials*, vol. 11, no. 10, 2021, doi: 10.3390/nano11102575.

[97] W. Cui, W. Lu, Y. Zhang, G. Lin, T. Wei, and L. Jiang, “Gold nanoparticle ink suitable for electric-conductive pattern fabrication using in ink-jet printing technology,” *Colloids Surf A Physicochem Eng Asp*, vol. 358, no. 1–3, 2010, doi: 10.1016/j.colsurfa.2010.01.023.

[98] P. Bian, Y. Wang, and T. J. McCarthy, “Rediscovering Silicones: The Anomalous Water Permeability of ‘Hydrophobic’ PDMS Suggests Nanostructure and Applications in Water Purification and Anti-Icing,” *Macromol Rapid Commun*, vol. 42, no. 5, 2021, doi: 10.1002/marc.202000682.

[99] Y. Liu, X. Dong, and P. Chen, “Biological and chemical sensors based on graphene materials,” *Chem Soc Rev*, vol. 41, no. 6, 2012, doi: 10.1039/c1cs15270j.

[100] N. Celik, N. Manivannan, A. Strudwick, and W. Balachandran, “Graphene-enabled electrodes for electrocardiogram monitoring,” *Nanomaterials*, vol. 6, no. 9, 2016, doi: 10.3390/nano6090156.

[101] O. Ozturk and M. K. Yapici, “Muscular Activity Monitoring and Surface Electromyography (sEMG) with Graphene Textiles,” in *Proceedings of IEEE Sensors*, Oct. 2019, vol. 2019-October. doi: 10.1109/SENSORS43011.2019.8956801.

[102] S. Grijalvo and D. D. Díaz, “Graphene-based hybrid materials as promising scaffolds for peripheral nerve regeneration,” *Neurochem Int*, vol. 147, 2021, doi: 10.1016/j.neuint.2021.105005.

[103] H. Zhu, A. Liu, F. Shan, W. Yang, C. Barrow, and J. Liu, “Direct transfer of graphene and application in low-voltage hybrid transistors,” *RSC Adv*, vol. 7, no. 4, 2017, doi: 10.1039/c6ra26452b.

[104] B. J. Lambert and F. W. Tang, “Rationale for practical medical device accelerated aging programs in AAMI TIR 17,” in *Radiation Physics and Chemistry*, 2000, vol. 57, no. 3–6. doi: 10.1016/S0969-806X(99)00403-X.

[105] M. L. Rynes *et al.*, “Assembly and operation of an open-source, computer numerical controlled (CNC) robot for performing cranial microsurgical procedures,” *Nat Protoc*, vol. 15, no. 6, 2020, doi: 10.1038/s41596-020-0318-4.

[106] S. M. Bernhard *et al.*, “An automated homecage system for multiwhisker detection and discrimination learning in mice,” *PLoS One*, vol. 15, no. 12 December, 2020, doi: 10.1371/journal.pone.0232916.

[107] X. Ouyang, R. Su, D. W. H. Ng, G. Han, D. R. Pearson, and M. C. McAlpine, “3D Printed Skin-Interfaced UV-Visible Hybrid Photodetectors,” *Advanced Science*, vol. 9, no. 25, p. 2201275, Sep. 2022, doi: 10.1002/advs.202201275.

[108] R. Chen, A. Canales, and P. Anikeeva, “Neural recording and modulation technologies,” *Nature Reviews Materials*, vol. 2, no. 2. 2017. doi: 10.1038/natrevmats.2016.93.

[109] T. Sekine, K. Fukuda, D. Kumaki, and S. Tokito, “The effect of mechanical strain on contact resistance in flexible printed organic thin-film transistors,” *Flexible and Printed Electronics*, vol. 1, no. 3, 2016, doi: 10.1088/2058-8585/1/3/035005.

[110] T. Wang, Y. Qi, J. Xu, X. Hu, and P. Chen, “Effects of poly(ethylene glycol) on electrical conductivity of poly(3,4-ethylenedioxythiophene)-poly(styrenesulfonic acid) film,” *Appl Surf Sci*, vol. 250, no. 1–4, 2005, doi: 10.1016/j.apsusc.2004.12.051.

[111] S. Xiong, L. Zhang, and X. Lu, “Conductivities enhancement of poly(3,4-ethylenedioxythiophene)/poly(styrene sulfonate) transparent electrodes with diol additives,” *Polymer Bulletin*, vol. 70, no. 1, 2013, doi: 10.1007/s00289-012-0833-8.

[112] D. Alemu Mengistie, P. C. Wang, and C. W. Chu, “Effect of molecular weight of additives on the conductivity of PEDOT:PSS and efficiency for ITO-free organic solar cells,” *J Mater Chem A Mater*, vol. 1, no. 34, 2013, doi: 10.1039/c3ta11726j.

[113] N. J. Sofroniew, D. Flickinger, J. King, and K. Svoboda, “A large field of view two-photon mesoscope with subcellular resolution for in vivo imaging,” *Elife*, vol. 5, no. JUN2016, 2016, doi: 10.7554/eLife.14472.

[114] J. Fan *et al.*, “Video-rate imaging of biological dynamics at centimetre scale and micrometre resolution,” *Nat Photonics*, vol. 13, no. 11, 2019, doi: 10.1038/s41566-019-0474-7.

[115] I. v. Kauvar *et al.*, “Cortical Observation by Synchronous Multifocal Optical Sampling Reveals Widespread Population Encoding of Actions,” *Neuron*, vol. 107, no. 2, 2020, doi: 10.1016/j.neuron.2020.04.023.

[116] C. Guo *et al.*, “Miniscope-LFOV: A large field of view, single cell resolution, miniature microscope for wired and wire-free imaging of neural dynamics in freely behaving animals,” *bioRxiv*, 2021.

[117] J. Akerboom *et al.*, “Optimization of a GCaMP calcium indicator for neural activity imaging,” *Journal of Neuroscience*, vol. 32, no. 40, 2012, doi: 10.1523/JNEUROSCI.2601-12.2012.

[118] S. F. Owen and A. C. Kreitzer, “An open-source control system for in vivo fluorescence measurements from deep-brain structures,” *J Neurosci Methods*, vol. 311, 2019, doi: 10.1016/j.jneumeth.2018.10.022.

[119] M. Pachitariu *et al.*, “Suite2p: beyond 10,000 neurons with standard two-photon microscopy,” *bioRxiv*, 2016, doi: 10.1101/061507.

[120] W. Zong *et al.*, “Miniature two-photon microscopy for enlarged field-of-view, multi-plane and long-term brain imaging,” *Nat Methods*, vol. 18, no. 1, 2021, doi: 10.1038/s41592-020-01024-z.

[121] X. Liu *et al.*, “Decoding ECoG High Gamma Power from Cellular Calcium Response using Transparent Graphene Microelectrodes,” in *International IEEE/EMBS Conference on Neural Engineering, NER*, 2019, vol. 2019-March. doi: 10.1109/NER.2019.8717147.

[122] P. Zhao *et al.*, “Strain-Discriminable Pressure/Proximity Sensing of Transparent Stretchable Electronic Skin Based on PEDOT:PSS/SWCNT Electrodes,” *ACS Appl Mater Interfaces*, vol. 12, no. 49, 2020, doi: 10.1021/acsami.0c16546.

[123] L. M. Ferrari *et al.*, “All-Polymer Printed Low-Cost Regenerative Nerve Cuff Electrodes,” *Front Bioeng Biotechnol*, vol. 9, 2021, doi: 10.3389/fbioe.2021.615218.

[124] S. K. Sinha *et al.*, “Screen-Printed PEDOT:PSS Electrodes on Commercial Finished Textiles for Electrocardiography,” *ACS Appl Mater Interfaces*, vol. 9, no. 43, 2017, doi: 10.1021/acsami.7b09954.